Faculty of Experimental Sciences,
University Pablo de Olavide

Improving Adsorption-Based Processes Using Porous Materials

Francisco D. Lahoz Martín

Seville, July 2019

ISBN: 978-84-09-12801-3

Printed by: LLARdigital

IMPROVING ADSORPTION-BASED PROCESSES USING POROUS MATERIALS

SUPERVISORS

Sofía Calero Díaz
Catedrática de Universidad
Dpto. de Sistemas Físicos Químicos y Naturales
Universidad Pablo de Olavide

Ana Martín Calvo
Titulado Superior de Apoyo a la Investigación - Doctor
Dpto. de Sistemas Físicos Químicos y Naturales
Universidad Pablo de Olavide

Work presented to obtain the degree of Doctor

Francisco D. Lahoz Martín
Licenciado en Biotecnología

Doctoral Supervisors

Prof. Sofía Calero Díaz
Dr. Ana Martín Calvo

Examination Committee

Chair: Prof. Germán Sastre Navarro
Secretary: Prof. María del Carmen Gordillo Bargueño
Member: Prof. José Manuel Romero Enrique

The research reported in this thesis was carried out at the Department of Physical Chemical and Natural Systems, University Pablo de Olavide (Seville, Spain) with financial support from the European Research Council – ERC Consolidator Grant (ERC2011-StG-279520-RASPA).

Contents

Appendixes

List of publications

Acknowledgements/Agradecimientos

1

Introduction

Carbon based molecules are the cornerstone of a wide variety of chemical and biological applications, in fields as far apart as medicine, computer electronics, or the petrochemical industry[1-4]. Simpler organic molecules may link to one another, creating chains and sheets, which can be connected into a range of frameworks. Using these chains to connect metallic centers creates complex three-dimensional porous structures, which prove to have important adsorptive and catalytic properties[5-7]. These organic molecular sieves are diverse in their topology and chemical make-up. These structures are classified under the umbrella term of metal-organic frameworks (MOFs)[8-11]. There is a large number of molecular sieves available at the moment, with a great amount of modified structures being created each year. It is critical to have an efficient method of screening, to learn how to navigate an ocean of useful prospects. In this context emerges more than ever the need for theoretical models which can be studied using molecular simulation methods[12]. Before testing the properties of a structure empirically, one can narrow the structure pool and steer later experimental endeavors towards suitable structures[13]. It is possible to predict the adsorptive behavior of a group of structures, with growing degree of accuracy[14].

In this thesis, two main industrial processes are studied: In the first place, the separation of mixtures containing ethane and ethylene. The importance of this separation in the industrial production of ethylene is evident considering the amount of ethylene produced annually worldwide[15,16]. The uses of ethylene range from chemical synthesis (polyethylene production) to food industry, since this molecule has a direct effect in the ripening of fruits[17,18]. However, the actual separation of these two compounds is carried out through high-cost processes[15]]. On the other hand, the separation of BTEX mixtures is very important. This group of aromatic compounds formed by benzene, toluene, ethylbenzene, and the isomers of xylene (ortho-, meta-, and para-xylene) is highly toxic[19,20]. The presence of these compounds in air has been proven harmful for humans and other living beings[21-23].

Nevertheless, their use is very extended in the petrochemical industry as they are part on many production processes such as the production of resistant plastics as polystyrene (ethylbenzene), polyethylene terephthalate (xylenes) or nylon (benzene and toluene)[24-26]. The environmental effect of BTEX mixtures has promoted the need of searching for techniques to efficiently separate their components[27-29].

1. Materials

This thesis focuses on the use of organic-based molecular sieves, and the adsorptive capacity of several MOFs and ZIFs (zeolitic imidazolate frameworks) is analyzed.

1.1. Metal-Organic Frameworks

The molecular sieves employed in this thesis fall under the category of Metal-Organic Frameworks (MOFs). These are crystalline nanostructures formed by organic ligands which serve as a link between different metallic clusters, knitting a three-dimensional network of pores and channels. By varying the type or length of the linkers, and also the metal element found in the metallic center, a vast array of possible structures may be obtained, with diverse adsorptive features. Compared to other well-known materials such as zeolites, some MOFs show higher flexibility and tunability, while maintaining good chemical and thermal stability[30,31].

Key features of MOFs are the high porosity and surface area[31]. Such features made these structures appealing for adsorption and storage of hydrogen, which is widely used in fuel cell technologies[32-34]. From there, many other uses for separation and storage of chemical compounds have been proposed for different MOFs[35,36]. The search for stable and usable structures has yielded a large number of frameworks, with over 75.000 theoretical MOFs listed by the Cambridge Crystallographic Data Centre (CCDC)[37]. The tunability of these structures allows for tailored desired features on adsorption and storage applications[38-43], as well as catalysis[44-46], fuel cell technologies[32,47,48], or drug delivery in biomedicine[49-53].

One of the drawbacks from MOFs is the instability in the presence of water, as the highly polarized water molecules attack the metals on the metallic centers, causing the structures to collapse. Some MOFs can withhold a relatively large amount of water inside, although they are rare and their adsorption capacity in other processes is not guaranteed[53-55].

The internal topology of MOFs favors an organization based on interconnected channels or one-directional channels. An example for each class is featured in Figure 1.

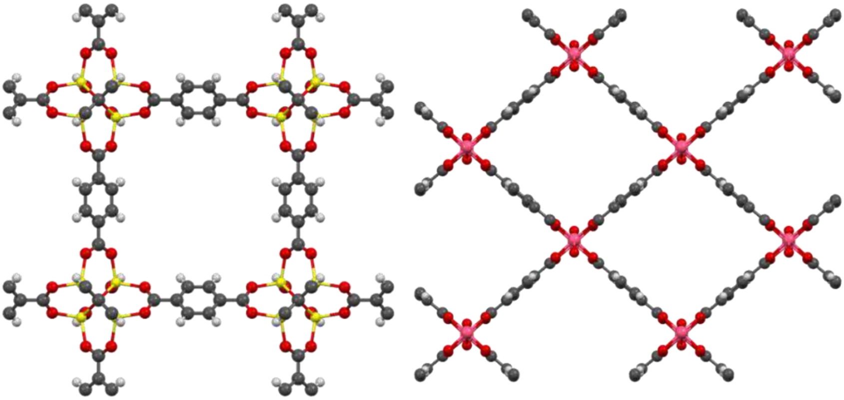

Figure 1. Representation of the crystallographic position of the atoms in IRMOF-1 (left) and MIL-47 (right). Color code: Carbon (grey), oxygen (red), hydrogen (white), zinc (yellow), and vanadium (pink).

One family of MOFs that has been used extensively in this work are the isoreticular metal-organic frameworks (IRMOFs). They were designed following the MOF-5 template (IRMOF-1) and systematically changing the organic linkers, to create a variety of pore sizes and topologies. The main goal for their synthesis by Yaghi *et al.* (2002) was methane storage, and their reported uses have widened since then to include greenhouse gases adsorption, biomedical applications and research or energy cells production[38]. A particularity of some of these IRMOFs-n, (n=1-16) is that their organic linkers are functionalized, affecting therefore to their adsorption and diffusion properties. IRMOF-1 is the simplest structure. The organic linker of IRMOF-1 is 1,4-benzenedicarboxylate and its orientation defines two cages of about 11 Å and 15 Å in diameter. IRMOFs-n (n=2-5) contain the same linker but different chemical composition of functionalized groups in the phenyl ring. IRMOF-2 and -3 have small functional groups such as bromine and amine, respectively while IRMOF-4 and -5 have larger linkers, 2,5-propanoyl-1,4-benzenedicarboxylate and 2,5-pentanoyl-1,4-benzenedicarboxylate, respectively. IRMOF-10 and -16 resemble IRMOF-1, but with increasing number of phenyl groups (2 phenyl groups in IRMOF-10, and 3 phenyl groups in IRMOF-16). IRMOF-7 and -8 have a naphthalene group, connected through a double bond, but the groups are connected to each other differently. In the case of IRMOF-7 the carbon atoms connected to the two metallic centers are located in the same benzene ring, while for IRMOF-8 each cyclic group connects to one metallic center. IRMOF-6 is another structure with two cyclic groups. The ligand of this structure is benzocyclobutene dicarboxylate. IRMOF-12 and -14 have hexahydropyrene dicarboxylate and pyrene dicarboxylate as linkers, respectively. The main difference between these structures is the delocalization of the double bonds in the linker that affects to the total number of hydrogen atoms of each structure. IRMOF-9, -11, -13, and -15 are like IRMOF-10, -12, -14, and -16, respectively, but with interpenetrating cavities.

Other two materials used in this thesis are MIL47 and MOF-1. MIL-47 belongs to the MIL series (*Material of Institut Lavoisier*) and was first synthesized by Barthelet *et al.*[56]. It contains vanadium as coordinated metallic center, and BDC (1,4-benzenedicarboxylate) as organic linker. This structure is characterized by diamond shaped straight channels in one direction[56]. MOF-1 is somehow similar to IRMOF-1, as it is characterized by the presence of zinc as coordinated metallic center and BDC as organic ligand. Along with the organic linkers, half of the metallic centers of the structure are linked via 4-diazabicyclo [2, 2, 2] octane (Dabco) groups[57,58].

1.2. Zeolitic Imidazolate Frameworks

A peculiar type of frameworks ties some characteristics of MOFs and zeolites. Zeolitic imidazolate frameworks (ZIFs) are a subclass of MOFs. They are also constituted by inorganic metallic centers linked by organic imidazolate ligands. However, they share structural features with zeolites, as bonding angles between metallic centers and imidazolate linkers mimic those of Si and O found in zeolite. As a result, topological counterparts to zeolites are obtained, which may be tailored to accommodate larger pores within. The transition metal employed can be also substituted, although the basic structures include Zinc coordinates in their metallic centers. Figure 2 depicts one of the structures used in this work, ZIF-71, with 4,5-dichloroimidazole linkers.

ZIFs were first described by Yaghi *et al.* in 2006[59]. As of today, over a hundred different structures have been reported[60]. Being structures that share fundamental features with both zeolites (topologies) and MOFs (flexibility and tenability), ZIFs materials are currently utilized in a variety of separation and storage processes, mainly of small gases such as CO_2[61-63]. Other uses of ZIFs include catalysis[64-66], and biomedical applications such as drug delivery[67-69].

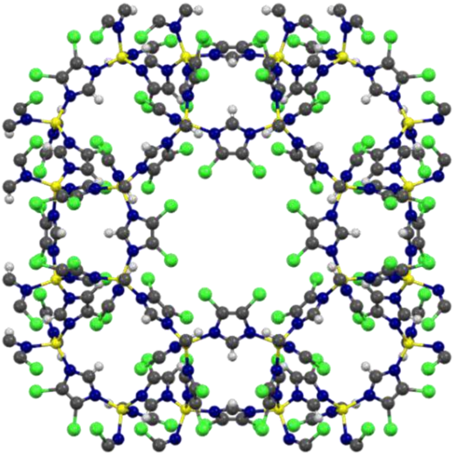

Figure 2. Representation of the crystallographic positions of the atoms in ZIF-71. Color code: Carbon (grey), nitrogen (blue), hydrogen (white), zinc (yellow), and chlorine (green).

In this thesis, the performance of ZIF-1, -2, -3, -4, -6, -10, -20, -22, -62, -68, -71, -80, -93, -96, and 97 is evaluated in terms of adsorption and separation capacity. These structures contain Zn as metallic center linked by ligands such as Iimidazole (Im), nitroimidazole (nIm), methylimidazole (mIm), 1,5-dicyclohexyl imidazole (dcIm), benzimidazole (bIm), hydroxymethylmethyl imidazole (hymeIm), 4-aldemethylimidazole (almeIm), cyanide amine imidazole (cyamIm), or purinate (pur). These linkers lead to large variety of topologies and pore sizes. For instance, ZIF-1, -2, -3, -4, -6, and -10 have imidazole (Im) as ligand, but their connections and orientations generate differences in the topologies (*crb, crb, dft, cag, gis*, and *mer*, respectively) and pore sizes. Other structures share the same topology and differ in linkers. This is the case of ZIF-71, -93, -96, and -97, structures with *rho* topology but with other functionalized imidazole (dcIm, almeIm, cyamIm, and hymeIm, respectively). ZIF-20 and -22 are structures with *lta* topology and large linkers (pur and bIm, respectively). Structures formed by two types of linkers such as ZIF-62 (Im, bIm), ZIF-68 (nIm, bIm), and ZIF-80 (nIm, dcIm) are also studied.

2. Simulation methods

Empirical methods are critical as a preliminary step in the study of the physical-chemical properties of a system. In the context of chemical separation of interesting compounds, molecular simulation techniques pave the way for experimental procedures by narrowing the search for useful structures. The simulation methods varied upon the characteristic under study.

Monte Carlo (MC) simulations are used to study average properties of the setup. With this method, a view of the stationary state of the system is obtained by sampling a number of its microstates. This method follows a statistical approach

[70,71]. The evolution of the properties of the system over time can also be studied using Molecular Dynamics (MD). MD simulations allow for a deterministic study of these changes. Information on the position and trajectory of the particles within the model is gained by solving classical motion equations (Newton's laws of motion)[72].

These methods can be applied to finite systems. Large simulation samples require long simulation times, and thus the total computational cost will be proportional to the sample size. To avoid such burden, periodic boundary conditions are established, where a finite simulation box is replicated infinitely in the three spatial directions.

2.1. Monte Carlo

Monte Carlo simulations are employed to understand the adsorptive behavior of the different adsorbates. The analysis derived from MC simulations draws a link between a series of microscopic variables and average thermodynamic features. These simulations are useful to measure and calculate several system's properties, such as adsorption isotherms or enthalpy of adsorption. MC is used in the context of several thermodynamic ensembles, namely grand canonical (μVT), canonical (NVT), and Gibbs (NVT) ensembles.

2.1.1 Ensembles

Grand Canonical (μVT)

MC simulations in the grand canonical ensemble (GCMC) are performed to calculate the number of molecules adsorbed inside the structure. The data output from GCMC simulations provide the adsorption isotherms. In this ensemble, the chemical potential (μ), volume (V) and temperature (T) are kept fixed at equilibrium with gas outside the system. Molecules inside the simulation box are allowed to be exchanged with molecules from a reservoir, having both the same chemical potential as to keep this property stable.[12,73] The chemical potential is related to the pressure, which is also set in the simulation, via fugacity (f).

$$\mu = \mu^0 + RT \ln\left(\frac{f}{f^0}\right) \qquad (1)$$

where μ^0 is the standard chemical potential, R is the ideal gas constant, T is the temperature and f^0 is the standard fugacity. Fugacity is related to pressure (P) according to a fugacity coefficient (Φ), which will be different for each gas species[74].

$$f = \Phi P \qquad (2)$$

where Φ is 1 for ideal gases. For most light gasses, it is also assumed that fugacity equals pressure when the real gas pressure is below 10^5 Pa.

Having fixed these parameters, after the simulation run, the number of molecules inside the structure (n_{abs}) is obtained. This is the absolute adsorption value, which is not equal to what is experimentally referred to as adsorption, as there are gas molecules which are inside the structure without them interacting with said structure – not properly adsorbed. To calculate the number of adsorbed molecules, excess adsorption or n_{exc}, the following equation is employed[75-78]:

$$n_{exc} = n_{abs} - V^g \rho^g \qquad (3)$$

where V^g is the pore volume and ρ^g is the molar density of the gas on the bulk. To use equation (3), the pore volume of the structure needs to be determined by studying the adsorption of helium (helium void fraction). This value may also be obtained the pore volume from experimental studies.

Canonical (NVT)

Simulations to perform energy calculations of an adsorbate/adsorption-surface couple are carried out in the canonical ensemble. In this ensemble, a constant number of particles (N), volume (V) and temperature (T) is maintained.

Energy calculations allow measuring the interaction between the adsorbate molecules and the structure. To ascertain appropriate values without interference of molecule-to-molecule interaction, simulations are performed at extreme diluted conditions – zero loading. This simulation framework allows the use of the Widom test particle method: a sole particle is inserted within the structure; the energy of the molecule-framework interaction is computed, and the molecule's Rosenbluth factor is re-evaluated; finally, the particle is deleted and a new one is inserted, with the new Rosenbluth factor[79-81].

Among the number of thermodynamic properties that can be deducted from the calculations, isosteric heats of adsorption (Q_{st}) and Henry coefficients (K_H) are calculated directly from the energy output of the system. The values of these energies are averaged throughout the simulation. These are related to the variation of internal energy within the system (ΔU). ΔU can be calculated from the average measures of potential energy of the host-guest (U_{HG}) by subtracting the average potential energy of host (U_H) and guest (U_G), respectively.

$$Q_{st} = RT - \Delta U \qquad (4)$$

$$\Delta U = (\langle U_{HG} \rangle - \langle U_H \rangle - \langle U_G \rangle) \qquad (5)$$

where R is the ideal gas constant and T is the temperature of the system.

Experimentally, to calculate the Henry coefficients (K_H), the chemical potential of the molecules is estimated. From the simulation point of view, this coefficient may also be linked to the Rosenbluth weight:

$$K_H = \frac{\langle W \rangle}{RT\rho\langle W^{IG} \rangle} \qquad (6)$$

where R is the ideal gas constant, T is the temperature, ρ is the density, $\langle W \rangle$ is the average Rosenbluth factor for a molecule in the system and $\langle W^{IG} \rangle$ is the average Rosenbluth factor for a molecule in an ideal gas.

Gibbs (NVT)

The Gibbs ensemble is based on the use of two coupled simulation boxes in the bulk of a fluid; one for the gas phase and another for the liquid phase. In both regions, periodic boundary conditions are applied independently. The temperature is kept fixed. Volume is constant for the whole of the system: while the two differentiated regions suffer volume fluctuations, total volume of the system is not altered, maintaining a constant pressure (Figure 3). Molecules may drift inside their box or be transferred from one region to the other in order to keep a constant chemical potential.

Simulations in the Gibbs ensemble are used to compute vapor-liquid equilibrium curves, as the densities of the fluid inside both boxes may be inferred after the system stability is reached. These calculations need experimental values of the critical parameters of the molecule: P_c, T_c and ρ_c as the critical point will be approached and calculations will require said data to be correctly calibrated. These parameters may also be obtained using density correction scales to calculate the critical temperature (T_c), the law of rectilinear diameters for the vapor-liquid equilibrium phase to calculate the critical density (ρ_c) and the Clausius-Clapeyron equation to calculate the critical pressure (P_c)[82-85].

$$\rho_{liq} - \rho_{vap} = B\,(T - T_c)^{\beta} \qquad (7)$$

$$\frac{(\rho_{liq} + \rho_{vap})}{2} = \rho_c + A\,(T - T_c) \qquad (8)$$

$$\ln P = C + \frac{C'}{T}, \qquad (9)$$

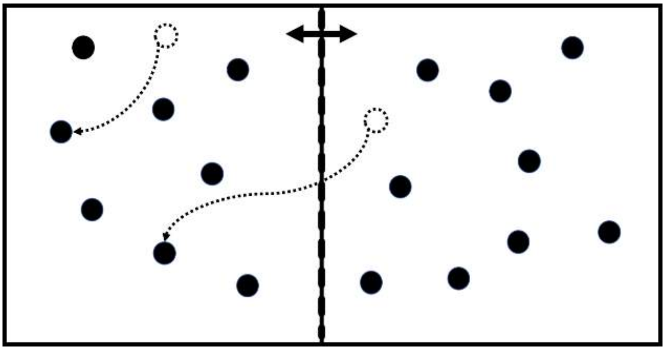

Figure 3. Molecules inside the simulation boxes in a Gibbs ensemble MC simulation. Boxes connection is represented by a movable permeable wall, allowing relative volume adjustments and molecule exchange.

2.1.2 MC calculations and techniques

MC is a stochastic technique where a bias can be applied at the sampling level to enhance its performance. Specifically, Markov Chain Monte Carlo (MCMC) is employed. A Markov process is based on the knowledge that a future state of a system will be dependent only on its current state. Each possible system configuration will have an assigned probability. Depending on these probabilities, transitions from current to future states would be accepted or declined. The changes proposed from state to state are given through random particle moves. These moves may or may not be accepted depending on an evaluation of the system's internal energy variation. There is a finite number of possible moves to be performed on a molecule: insertion into a random spatial place inside the simulation box, deletion from its current position inside the simulation box and rotation around the molecule's center of mass. A certain molecule may also be regrown, be it a partial or complete regrowth. When performing a simulation with a mixture of different molecules, one molecule may be swap by another one (identity change).

To accept or reject certain move, the probability of finding the system in the current simulation state ($P_S(1)$) is calculated and compared to the probability of it being at a newer state ($P_S(2)$). The probability of performing a move between the one state and the other ($(1 \rightarrow 2)$ or $M(2 \rightarrow 1)$), as well as the probability of accepting said trial move forward or backwards ($P_A(1 \rightarrow 2)$ or ($P_A(2 \rightarrow 1)$), are also taken into account. A balance between both simulation states is assumed.

$$P_S(1)\, M(1 \rightarrow 2)\, P_A\,(1 \rightarrow 2) = P_S(2)\, M(2 \rightarrow 1)\, P_A(2 \rightarrow 1) \qquad (10)$$

Since the sheer probability of moving thru states is equal, $M(1 \rightarrow 2) = M(2 \rightarrow 1)$, the probability of accepting the trial move can be calculated following the algorithm acceptance rule:

$$P_A(1 \rightarrow 2) = \min\left(1, \frac{P_S(2)}{P_S(1)}\right) \qquad (11)$$

The move will be accepted when the probability is equal to or over 1 and will be randomly accepted or rejected if the probability is lower.

As is, MCMC simulations would require a large computational time due to initial low insertion probabilities of the molecules inside the set framework. Simulation time is sensibly increased when larger molecules enter the structures, as they may overlap with one another. To bypass these issues, the molecular growth within the background framework is biased by using Configurational Bias Monte Carlo (CBMC)[86]. The way this method works enables the molecules to grow in sequential steps, in parts denoted as beads. Each new bead will be given a set probability of growing in a certain direction and orientation, basically dividing the overall probabilities calculations previously stated in several parts, accepting the growing path which leads to a lower value of internal energy within the molecule and external energy within the system.

$$P_i(j) = \frac{e^{-\beta U_i^{ext}(j)}}{\sum_{l=1}^{k} e^{-\beta U_i^{ext}(l)}} = \frac{e^{-\beta U_i^{ext}(j)}}{\omega_i} \qquad (12)$$

Where T is the temperature, $k_B$is the Boltzmann constant, β is inversely proportional to k_B ($\beta = 1/(k_B T)$) and the Rosenbluth weight is denoted by ω_i.

The probability of the molecule growing through this path is related to the Rosenbluth factor, which must be re-evaluated after a new trial bead is added to the growing chain.

$$W = \prod_i \omega_i \qquad (13)$$

2.2. Molecular Dynamics

Molecular Dynamics (MD) simulations are carried out to obtain the evolution of the system over time. In MD, Newton's laws of motion equations are solved for the atoms and molecules involved. MD simulations are carried out within fixed volume, temperature and number of particles (canonical ensemble). To limit temperature fluctuations, the Nosé-Hoover thermostat is employed[87,88].

Each simulation state gives information about each particle's position, velocity and acceleration vectors, and it is possible to estimate its path forward. Future simulation states are computed based upon motion information from previous steps. Acceleration information is derived from force balances computed using the set force field. Knowing the initial velocity and spatial position of a particle, its velocity and position at a future simulation state (time t) can be calculated.

$$v_i(t) = v_i(0) + \int_0^t \frac{dv}{dt}\, dt \qquad (14)$$

$$r_i(t) = r_i(0) + \int_0^t v_i(t)\, dt \qquad (15)$$

where v_i is the velocity vector of the particle, and r_i is the particle's position vector.

Integration algorithms are effective to save computational time. The Velvet algorithm calculates the position (r) and velocity (v) moving forward or backwards in the simulation state pool[89,90].

$$r_i(t+\tau) = r_i(t) + v_i(t)\,\tau + \frac{f_i(t)}{2m_i}\tau^2 \qquad (16)$$

$$r_i(t-\tau) = r_i(t) - v_i(t)\,\tau + \frac{f_i(t)}{2m_i}\tau^2 \qquad (17)$$

where r_i is the position vector, v_i is the velocity vector, f_i is the force vector, τ is the simulation time step, and m_i is the mass of the particle.

From equations (15) and (16) a joint equation to compute the following spatial positions is derived.

$$r_i(t+\tau) = -\,r_i(t-\ \tau) + 2\,r_i(t)\,\tau + \frac{f_i(t)}{m_i}\tau^2 \qquad (18)$$

To calculate velocity, since it is not present at the position equation, the velocity Velvet algorithm is used and solved for v_i.

$$v_i(t) = \frac{r_i(t+\tau) - r_i(t-\tau)}{2\tau} \qquad (19)$$

With this information, self-diffusion coefficients (Ds) can be calculated from the displacement of the particles in each directional axis. The mean square displacement for each particle is computed with respect to its center of mass. D_s can be determined from the value of the gradient at long simulation times. Self-diffusion coefficients are obtained for each axial direction (${D_s}^x$, ${D_s}^y$ and ${D_s}^z$). The following equation is used to calculate ${D_s}^x$, with the other directional values being calculated identically.

$$D_s^x = \frac{1}{2N} \lim_{t\to\infty} \frac{d}{dt}\left[\sum_{i=1}^{N}\left({r_i}^x(t) - {r_i}^x(t_0)\right)^2\right] \qquad (20)$$

where N is the total number of particles and ${r_i}^x$ is the positional component on the *x*-axis.

To determine the total D_s, ${D_s}^x$, ${D_s}^y$ and ${D_s}^z$ are averaged.

3. Force fields and models

Computational models are needed for the adsorbates the structures and their interactions in order to perform the simulations. These models need to be able to reproduce the kind of interactions and outcomes expected from them in real conditions. The use of simulation methods can be coupled with experimental procedures as far as the models are accurate representations of their empirical counterparts.

To recreate the interactions between adsorbates themselves, and consider the adsorbate-structure interactions, a series of parameters based on classical mechanics calculations are set.

3.1. Force fields

A set of rules is described to compute the total internal energy of the system (U^{TOTAL}) as a simple sum of the interactions of pairs of defined particles within the setup. These interactions may come from the internal energy of some of the molecules involved, U^{BONDED}, or from interactions between non-bonded atoms ($U^{NON-BONDED}$).

$$U^{TOTAL} = U^{BONDED} + U^{NON-BONDED} \qquad (21)$$

<u>Internal energy within molecules</u>

The bonded component of the sum is obtained from interaction energies within atoms of the same molecule, which are bonded to each other. Potential energies for atomic pairs, three, and four atom chains are considered.

The interaction between two consecutive atoms sets the bond potential energy (U^{BOND}). This energy is computed using a harmonic potential which is directly related to the distances between the two atoms (i and j).

$$U^{BOND} = \frac{1}{2} k_B (r - r_0)^2 \qquad (22)$$

where k_B is the potential constant for the bond interaction, r is the distance between atoms i and j, and r_0 is the distance between these atoms at equilibrium.

When three consecutive atoms within a molecule are evaluated, the resulting potential energy is related directly to the angle they form. The bend potential energy (U^{BEND}) is also calculated according to a harmonic potential.

$$U^{BEND} = \frac{1}{2} k_A \left(\theta_{ijk} - \theta_0\right)^2 \quad (23)$$

where k_A is the angle bend constant, θ_{ijk} is the angle formed between atoms *i*, *j* and *k*, and θ_0 is the angle between the atoms at equilibrium.

The interaction between four consecutive atoms (*i*, *j*, *k*, and *l*) is accounted for in the torsion energy calculation ($U^{TORSION}$). This potential is related to the angle formed between the planes of the bending angle θ_{ijk} and θ_{jkl}. These types of straightforward interactions are known as proper torsion. When the four atoms are not arranged consecutively forming a chain, and there is a central atom (*i*) connected to the other three, an improper torsion can be defined. The improper torsion potential depends on the angle formed between the plane three (*i*, *j*, *k*) and the position of the other atom (*l*). Both proper and improper torsions are calculated via TraPPE dihedral potential.

$$U^{TORSION} = p_0 + p_1\left[1 + \cos\left(\varphi_{ijkl}\right)\right] + p_2\left[1 - \cos\left(2\varphi_{ijkl}\right)\right] + p_3\left[1 + \cos\left(3\varphi_{ijkl}\right)\right] \quad (24)$$

where p_o, p_1, p_2, p_3 are parameters of the potential and φ_{ijkl} is the dihedral angle.

The total bonded internal energy is calculated as a sum of the bond, bend and torsion potentials.

$$U^{BONDED} = U^{BOND} + U^{BEND} + U^{TORSION} \quad (25)$$

Internal energy between molecules

To calculate the non-bonded internal energy of the system, the interaction potential between atoms on different molecules (or more than 4 atoms away in the same molecule) is considered, as they are not accounted for by the bonded potential. These non-bonded interactions are calculated as a sum of van der Waals and coulombic potentials.

$$U^{NON-BONDED} = U^{vdW} + U^{COULOMBIC} \quad (26)$$

To define the van der Waals interactions, Lennard-Jones potentials are used.

$$U^{vdW} = 4\varepsilon\left[\left(\frac{\sigma}{r}\right)^{12} - \left(\frac{\sigma}{r}\right)^{6}\right] \quad (27)$$

where ε is an energy parameter representing the depth of the potential well, r is the distance between the two atoms, and σ is the distance parameter at which the potential is zero.

The energy and distance parameters of the potential are equivalent for same-atom interactions. To calculate the potential interaction between different atoms (*i* and *j*), new parameters must be obtained depending on the values of ε and σ of each atom type. Lorentz-Berthelot mixing rules are employed to calculate these parameters[91].

$$\varepsilon_{ij} = \sqrt{\varepsilon_{ii}\,\varepsilon_{jj}} \qquad (28)$$

$$\sigma_{ij} = \frac{1}{2}\,(\sigma_{ii} + \sigma_{jj}) \qquad (29)$$

Coulomb's law is used to define the electrostatic interactions.

$$U^{COULOMBIC} = \frac{q_i q_j}{4\pi\varepsilon_0\varepsilon_r r} \qquad (30)$$

where q_i and q_j are the point charges defined for atoms *i* and *k* respectively, ε_0 is the vacuum permittivity, ε_r is the relative permittivity of the system and r is the distance between *i* and *k*.

Both coulombic and van der Waals interactions may result in unnecessary usage of computational power, and limitations are set to prevent such outcome. As Lennard-Jones potentials fail to decrease to zero at short distances, a correction factor is applied for distances over 12 Å (cut-off distance), at which energies they are cut and shifted. An energy correction is also applied to the coulombic interaction. The coulombic sums are slow to reach convergence, so the Ewald Summation method is used to calculate the electrostatic component of the system[92].

3.2. Molecular models

To carry out the simulations, computational models for both the adsorbates and the adsorbents must be defined. There is a wide range of possibilities regarding flexibility and particle definition. The choices put forward in this work come from a compromise between experimental parallels and computational costs, ensuring that models used can reproduce experimental parameters before carrying out future calculations.

Models for the adsorbates

The adsorbates employed throughout this thesis are defined as rigid. The possible influences of flexibility were tested early on, as it was the case with the ethane model employed, and it was concluded that the results were identical, whereas computation times were shortened because of the long-range interaction that did not need to be attended for.

- Acyclic compounds – paraffins and olefins

United atom models for ethane and ethylene are used. Each CHx group is defined as an interaction center, with Lennard-Jones parameters taken from Dubbledam *et al.*[93] and the bond length from Liu *et al.*[94]]. Partial charges for the adsorbates are not considered, as to follow the already defined models. Both models reproduce experimental properties such as the vapor-liquid equilibrium curve.

- Aromatic carbons

Several cyclic carbons have been employed, all components of BTEX mixtures: Benzene, ethylbenzene, toluene, *o*-xylene, *m*-xylene, and *p*-xylene. The molecules are modelled as a mixed full-atom / united-atom model, with the benzene ring as full atom and the radicals (methyl and ethyl groups, respectively) as united atom models. Tests were carried out using full atom models for ethylbenzene and toluene, with no different outcome for adsorptive or diffusive behavior. Models for the BTEX molecules are taken from Castillo *et al.*[95], Rai *et al.*[96], Jorgensen *et al.*[97], and Caleman *et al.*[98].

- Side compounds

Throughout this thesis, different compounds have been used to simulate more realistic mixture conditions. These compounds are out of the interest of the separation / removal procedures, although they cause different effects on the adsorption and mobility of the molecules of interests, thus making them essential to reproduce conditions as close to experimental as possible. N_2, O_2, CH_4, CO, CO_2, and H_2.

N_2 (Martin-Calvo *et al.*)[99], H_2 (Deeg *et al.*)[100], O_2 (Calero *et al.*)[101], CO (Martin-Calvo *et al.*)[102], CO_2 (García-Sánchez *et al.*)[103] are described using full atom models. The diatomic molecules N_2, O_2 and CO have two interaction centers plus a dummy atom defined equidistant of both atoms in the center of the line linking both. This is needed to reproduce the dipolar moment, as the dummy atom is given a charge value but not a mass. The model of H_2 considers Feynman-Hibbs quantum corrections. CH_4 is defined as a single Lennard-Jones interaction center (united atom model), and the molecular model is taken from Dubbeldam *et al.*[104]

<u>Models for the structures</u>

The models for the structures are derived from experimental crystallographic information on the atomic positions of the structures. Regarding flexibility, although MOFs are known to be relatively flexible, the computational cost and the lack of force field parameters availability associated with flexibility computations made rigid models then most appropriate choice. To be consistent with experimental results, the structures used do not display large flexibility at the loading, temperature, and pressure they are worked on.

Atoms of the structures are defined as unique, with potential calculations being made using Lennard-Jones parameters and charges on each atom. UFF[105] and DREIDING[106] force fields are used to define said parameters.

4. Outline of the thesis

In this thesis, the use of molecular simulations as a fast and convenient method to understand the adsorptive behavior of complex systems is proposed. This thesis focuses on industrially relevant chemical separations which are either not fully optimized or highly energy-consuming. The separation methods described could prove useful within the chemical and petrochemical industries. This thesis is divided in three chapters, each one addressing a separation challenge known and offering several MOFs which could help improving current methods.

Study of the effect of the linker type and length on the adsorption of paraffins and olefins (Chapter 2)

Along this thesis, the tunability of MOFs and its effect on the adsorptive properties of the structures are studied. One of the key features that may be altered from one structure to another is the type of linker. Chapter 2 analyzes the differences among the members of the IRMOF family and the way the affect adsorption and diffusion of adsorbates. Different ethane/ethylene mixtures are tested, looking for a structure capable of enhancing the separation of these linear compounds.

The effect of the length of the linker chain and the influence of having interpenetrated cages inside the structure are also examined. Several structures capable of favoring the adsorption of ethane, thus leaving an enriched effluent of ethylene, have been described.

Topology effect on the adsorption of paraffins and olefins (Chapters 3)

Several mixtures are employed to assess the separation capabilities of the structures at different conditions. At the experimental level, ethane/ethylene mixtures are carried out using a high proportion of molecular nitrogen in a ternary mixture. The effect that the presence of nitrogen has on this separation is studied. Since there have been reported good separation results using this mixture on zeolites, an array of ZIFs have been employed to study possible differences in adsorption due to the topological disparities between them. To prevent other effects, the simulations are limited to zinc based ZIFs.

Industrial mixture guides indicate the presence of gases other than ethane and ethylene, and several gases have been added to the simulation mixture. A seven-component mixture of ethane, ethylene, hydrogen, oxygen, carbon monoxide, carbon dioxide, and methane is studied. Under these mixture conditions, several structures able to capture ethane have been found, which leave a cleaner route for the complete separation of ethylene.

Differential adsorption of similar aromatic compounds (Chapter 4)

Another industrial application of interest is the separation of ethylbenzene from BTEX mixtures. Benzene, toluene, ethylbenzene and xylene isomers are found at petrochemical industrial setups, where an interest in obtaining an enriched ethylbenzene mixture is crucial. Being similar compounds, the effect of the type of framework topology is studied, comparing adsorption and diffusion results between MOFs structurally divided in cages (MOF-1, IRMOF-1) with MOFs characterized by large one-dimensional channels (MIL-47).

Different linkers orientation and metallic centers can influence the behavior of the adsorbates, and it is possible to separate ethylbenzene from the other components given its longer shape. An enriched mixture of *o*-xylene, also an industrially relevant compound, can also be obtained.

Conclusions (Chapter 5)

Conclusions from the previous chapters, as well as global conclusions and reflections are collected in chapter 5.

Bibliography

(1) Schmid, A.; Dordick, J. S.; Hauer, B.; Kiener, A.; Wubbolts, M.; Witholt, B. *Nature* **2001**, *409*, 258.

(2) Ravot, G.; Masson, J.-M.; Lefevre, F. In *Extremophiles*; Rainey, F. A., Oren, A., Eds. 2006; Vol. 35, p 785.

(3) Yaakob, Z.; Ali, E.; Zainal, A.; Mohamad, M.; Takriff, M. S. *Journal of Biological Research-Thessaloniki* **2014**, *21*.

(4) Andersohn, F.; Konzen, C.; Garbe, E. *Annals of Internal Medicine* **2007**, *146*, 657.

(5) Fujita, M.; Oguro, D.; Miyazawa, M.; Oka, H.; Yamaguchi, K.; Ogura, K. *Nature* **1995**, *378*, 469.

(6) Yaghi, O. M.; Li, H. L.; Groy, T. L. *Journal of the American Chemical Society* **1996**, *118*, 9096.

(7) Janiak, C. *Angewandte Chemie-International Edition* **1997**, *36*, 1431.

(8) Eddaoudi, M.; Li, H. L.; Yaghi, O. M. *Journal of the American Chemical Society* **2000**, *122*, 1391.

(9) Yaghi, O. M.; Li, H. L. *Journal of the American Chemical Society* **1995**, *117*, 10401.

(10) Li, H.; Eddaoudi, M.; O'Keeffe, M.; Yaghi, O. M. *Nature* **1999**, *402*, 276.

(11) Czaja, A. U.; Trukhan, N.; Mueller, U. *Chemical Society Reviews* **2009**, *38*, 1284.

(12) Frenkel, D.; Smit, B. *Undesrtanding Molecular Simulation: From Algorithms to Applications*; Academic Press: San Diego. C.A., 2002.

(13) Dueren, T.; Bae, Y.-S.; Snurr, R. Q. *Chemical Society Reviews* **2009**, *38*, 1237.

(14) Krishna, R.; van Baten, J. M. *Chemical Engineering Journal* **2007**, *133*, 121.

(15) Salgado-Gordon, H.-J.; Valbuena-Moreno, G. *Ct&F-Ciencia Tecnologia Y Futuro* **2011**, *4*, 73.

(16) True, W. R. *Oil Gas J.* **2012**, *110*.

(17) Xie, T. Y.; McAuley, K. B.; Hsu, J. C. C.; Bacon, D. W. *Industrial & Engineering Chemistry Research* **1994**, *33*, 449.

(18) Kim, J.; Chang, C.; Tucker, M. L. *Frontiers in Plant Science* **2015**, *6*.

(19) Dijkema, G. P. J.; Grievink, J.; Weijnen, M. P. C. *Process Safety and Environmental Protection* **2003**, *81*, 331.

(20) Mehlman, M. A. *Teratogenesis Carcinogenesis and Mutagenesis* **1990**, *10*, 399.

(21) Rosell, M.; Lacorte, S.; Barcelo, D. *Journal of Chromatography A* **2006**, *1132*, 28.

(22) Baltrenas, P.; Baltrenaite, E.; Sereviciene, V.; Pereira, P. *Environmental Monitoring and Assessment* **2011**, *182*, 115.

(23) Liu, K.; Quan, J.; Mu, Y.; Zhang, Q.; Liu, J.; Gao, Y.; Chen, P.; Zhao, D.; Tian, H. *Atmospheric Environment* **2013**, *73*, 11.

(24) Barraque, M. *Actualite Chimique* **1997**, 18.

(25) Castro, A. J. R.; Soares, J. M.; Filho, J. M.; Oliveira, A. C.; Campos, A.; Milet, E. R. C. *Fuel* **2013**, *108*, 740.

(26) He, J.; Li, R.; Gu, F. *Journal of Applied Polymer Science* **2013**, *128*, 1673.

(27) Seifi, L.; Torabian, A.; Kazemian, H.; Bidhendi, G. N.; Azimi, A. A.; Farhadi, F.; Nazmara, S. *Water Air and Soil Pollution* **2011**, *219*, 443.

(28) Torabian, A.; Kazemian, H.; Seifi, L.; Bidhendi, G. N.; Azimi, A. A.; Ghadiri, S. K. *Clean-Soil Air Water* **2010**, *38*, 77.

(29) Ranck, J. M.; Bowman, R. S.; Weeber, J. L.; Katz, L. E.; Sullivan, E. J. *Journal of Environmental Engineering-Asce* **2005**, *131*, 434.

(30) Fletcher, A. J.; Thomas, K. M.; Rosseinsky, M. J. *Journal of Solid State Chemistry* **2005**, *178*, 2491.

(31) Zhou, H.-C. J.; Kitagawa, S. *Chemical Society Reviews* **2014**, *43*, 5415.

(32) Rosi, N. L.; Eckert, J.; Eddaoudi, M.; Vodak, D. T.; Kim, J.; O'Keeffe, M.; Yaghi, O. M. *Science* **2003**, *300*, 1127.

(33) Murray, L. J.; Dinca, M.; Long, J. R. *Chemical Society Reviews* **2009**, *38*, 1294.

(34) Suh, M. P.; Park, H. J.; Prasad, T. K.; Lim, D.-W. *Chemical Reviews* **2012**, *112*, 782.

(35) *Metal-Organic Frameworks: Applications from Catalysis to Gas Storage*, 2011.

(36) Yuan, S.; Feng, L.; Wang, K.; Pang, J.; Bosch, M.; Lollar, C.; Sun, Y.; Qin, J.; Yang, X.; Zhang, P.; Wang, Q.; Zou, L.; Zhang, Y.; Zhang, L.; Fang, Y.; Li, J.; Zhou, H.-C. *Advanced Materials* **2018**, *30*.

(37) Groom, C. R.; Bruno, I. J.; Lightfoot, M. P.; Ward, S. C. *Acta Crystallographica Section B-Structural Science Crystal Engineering and Materials* **2016**, *72*, 171.

(38) Eddaoudi, M.; Kim, J.; Rosi, N.; Vodak, D.; Wachter, J.; O'Keeffe, M.; Yaghi, O. M. *Science* **2002**, *295*, 469.

(39) Hirscher, M.; Panella, B. *Scripta Materialia* **2007**, *56*, 809.

(40) Hirscher, M.; Panella, B.; Schmitz, B. *Microporous and Mesoporous Materials* **2010**, *129*, 335.

(41) Zhou, H.-C.; Long, J. R.; Yaghi, O. M. *Chemical Reviews* **2012**, *112*, 673.

(42) Zhao, X.; Wang, Y.; Li, D.-S.; Bu, X.; Feng, P. *Advanced Materials* **2018**, *30*.

(43) Li, H.; Wang, K.; Sun, Y.; Lollar, C. T.; Li, J.; Zhou, H.-C. *Materials Today* **2018**, *21*, 108.

(44) Lee, J.; Farha, O. K.; Roberts, J.; Scheidt, K. A.; Nguyen, S. T.; Hupp, J. T. *Chemical Society Reviews* **2009**, *38*, 1450.

(45) Llabres i Xamena, F. X.; Abad, A.; Corma, A.; Garcia, H. *Journal of Catalysis* **2007**, *250*, 294.

(46) Shen, K.; Chen, X.; Chen, J.; Li, Y. *Acs Catalysis* **2016**, *6*, 5887.

(47) Chaikittisilp, W.; Ariga, K.; Yamauchi, Y. *Journal of Materials Chemistry A* **2013**, *1*, 14.

(48) Sun, D. F.; Ma, S. Q.; Ke, Y. X.; Collins, D. J.; Zhou, H. C. *Journal of the American Chemical Society* **2006**, *128*, 3896.

(49) Horcajada, P.; Gref, R.; Baati, T.; Allan, P. K.; Maurin, G.; Couvreur, P.; Ferey, G.; Morris, R. E.; Serre, C. *Chemical Reviews* **2012**, *112*, 1232.

(50) Torad, N. L.; Li, Y.; Ishihara, S.; Ariga, K.; Kamachi, Y.; Lian, H.-Y.; Hamoudi, H.; Sakka, Y.; Chaikittisilp, W.; Wu, K. C. W.; Yamauchi, Y. *Chemistry Letters* **2014**, *43*, 717.

(51) Orellana-Tavra, C.; Baxter, E. F.; Tian, T.; Bennett, T. D.; Slater, N. K. H.; Cheetham, A. K.; Fairen-Jimenez, D. *Chemical Communications* **2015**, *51*, 13878.

(52) Wu, M.-X.; Yang, Y.-W. *Advanced Materials* **2017**, *29*.

(53) Burtch, N. C.; Jasuja, H.; Walton, K. S. *Chemical Reviews* **2014**, *114*, 10575.

(54) Wu, T.; Shen, L.; Luebbers, M.; Hu, C.; Chen, Q.; Ni, Z.; Masel, R. I. *Chemical Communications* **2010**, *46*, 6120.

(55) Zuluaga, S.; Fuentes-Fernandez, E. M. A.; Tan, K.; Xu, F.; Li, J.; Chabal, Y. J.; Thonhauser, T. *Journal of Materials Chemistry A* **2016**, *4*, 5176.

(56) Barthelet, K.; Marrot, J.; Riou, D.; Ferey, G. *Angewandte Chemie-International Edition* **2002**, *41*, 281.

(57) Dybtsev, D. N.; Chun, H.; Kim, K. *Angewandte Chemie-International Edition* **2004**, *43*, 5033.

(58) Mishra, P.; Edubilli, S.; Mandal, B.; Gumma, S. *Microporous and Mesoporous Materials* **2013**, *169*, 75.

(59) Park, K. S.; Ni, Z.; Cote, A. P.; Choi, J. Y.; Huang, R.; Uribe-Romo, F. J.; Chae, H. K.; O'Keeffe, M.; Yaghi, O. M. *Proceedings of the National Academy of Sciences of the United States of America* **2006**, *103*, 10186.

(60) Yaghi, O. M.; Yang, J.; Zhang, Y. 20180326397, **2018**.

(61) Banerjee, R.; Phan, A.; Wang, B.; Knobler, C.; Furukawa, H.; O'Keeffe, M.; Yaghi, O. M. *Science* **2008**, *319*, 939.

(62) Venna, S. R.; Carreon, M. A. *Journal of the American Chemical Society* **2010**, *132*, 76.

(63) Perez-Pellitero, J.; Amrouche, H.; Siperstein, F. R.; Pirngruber, G.; Nieto-Draghi, C.; Chaplais, G.; Simon-Masseron, A.; Bazer-Bachi, D.; Peralta, D.; Bats, N. *Chemistry-a European Journal* **2010**, *16*, 1560.

(64) Nguyen, L. T. L.; Le, K. K. A.; Truong, H. X.; Phan, N. T. S. *Catalysis Science & Technology* **2012**, *2*, 521.

(65) Miralda, C. M.; Macias, E. E.; Zhu, M.; Ratnasamy, P.; Carreon, M. A. *Acs Catalysis* **2012**, *2*, 180.

(66) Wang, F.; Liu, Z.-S.; Yang, H.; Tan, Y.-X.; Zhang, J. *Angewandte Chemie-International Edition* **2011**, *50*, 450.

(67) Sun, C.-Y.; Qin, C.; Wang, X.-L.; Yang, G.-S.; Shao, K.-Z.; Lan, Y.-Q.; Su, Z.-M.; Huang, P.; Wang, C.-G.; Wang, E.-B. *Dalton Transactions* **2012**, *41*, 6906.

(68) He, M.; Zhou, J.; Chen, J.; Zheng, F.; Wang, D.; Shi, R.; Guo, Z.; Wang, H.; Chen, Q. *Journal of Materials Chemistry B* **2015**, *3*, 9033.

(69) Zheng, H.; Zhang, Y.; Liu, L.; Wan, W.; Guo, P.; Nystrom, A. M.; Zou, X. *Journal of the American Chemical Society* **2016**, *138*, 962.

(70) Rubinstein, R. Y.; Kroese, D. P. *Simulation and the Monte Carlo method*; John Wiley & Sons, Inc., Hoboken, New Jersey, 2016; Vol. 10.

(71) Binder, K.; Heermann, D. *Springer series in solid-state sciences.*

(72) Nose, S. *Molecular Physics* **1984**, *52*, 255.

(73) Liu, J.; Culp, J. T.; Natesakhawat, S.; Bockrath, B. C.; Zande, B.; Sankar, S. G.; Garberoglio, G.; Johnson, J. K. *Journal of Physical Chemistry C* **2007**, *111*, 9305.

(74) Peng, D.; Robinson, D. B. *Industrial & Engineering Chemistry Fundamentals* **1976**, *15*, 59.

(75) Talu, O.; Myers, A. L. *Aiche Journal* **2001**, *47*, 1160.

(76) Duren, T.; Sarkisov, L.; Yaghi, O. M.; Snurr, R. Q. *Langmuir* **2004**, *20*, 2683.

(77) Myers, A. L. *Aiche Journal* **2002**, *48*, 145.

(78) Myers, A. L.; Monson, P. A. *Langmuir* **2002**, *18*, 10261.

(79) Widom, B. *Journal of Chemical Physics* **1963**, *39*, 2808.

(80) Vlugt, T. J. H. *Molecular Simulation* **1999**, *23*, 63.

(81) Vlugt, T. J. H.; Garcia-Perez, E.; Dubbeldam, D.; Ban, S.; Calero, S. *Journal of Chemical Theory and Computation* **2008**, *4*, 1107.

(82) Atkins, P. W. *Physical Chemistry*; Oxford Higher Educations: New York, 1990.

(83) Martin, M. G.; Siepmann, J. I. *Journal of Physical Chemistry B* **1998**, *102*, 2569.

(84) Rowlinson, J. S.; Swinton, F. L. *Liquids and Liquid Mixtures*; Butterworhts: London, 1982.

(85) Rowlinson, J. S.; Widom, B. *Molecular Theory of Capillarity*; Oxford University Press: New York, 1989.

(86) Siepmann, J. I.; Frenkel, D. *Molecular Physics* **1992**, *75*, 59.

(87) Nosé, S. *Journal of Chemical Physics* **1984**, *81*, 511.

(88) Hoover, W. G. *Physical Review A* **1985**, *31*, 1695.

(89) Verlet, L. *Physical Review* **1967**, *159*, 98.

(90) Verlet, L. *Physical Review* **1968**, *165*, 201.

(91) Allen, M. P.; Tildesley, D. J. *Computer Simulation of Liquids* Oxford Clarendon Press, 1987.

(92) Ewald, P. P. *Annalen Der Physik* **1921**, *64*, 253.

(93) Dubbeldam, D.; Calero, S.; Vlugt, T. J. H.; Krishna, R.; Maesen, T. L. M.; Beerdsen, E.; Smit, B. *Physical Review Letters* **2004**, *93*.

(94) Liu, B.; Smit, B.; Rey, F.; Valencia, S.; Calero, S. *Journal of Physical Chemistry C* **2008**, *112*, 2492.

(95) Castillo, J. M.; Vlugt, T. J. H.; Calero, S. *Journal of Physical Chemistry C* **2009**, *113*, 20869.

(96) Rai, N.; Siepmann, J. I. *Journal of Physical Chemistry B* **2007**, *111*, 10790.

(97) Jorgensen, W. L.; Nguyen, T. B. *Journal of Computational Chemistry* **1993**, *14*, 195.

(98) Caleman, C.; van Maaren, P. J.; Hong, M.; Hub, J. S.; Costa, L. T.; van der Spoel, D. *Journal of Chemical Theory and Computation* **2012**, *8*, 61.

(99) Martin-Calvo, A.; Garcia-Perez, E.; Garcia-Sanchez, A.; Bueno-Perez, R.; Hamad, S.; Calero, S. *Physical Chemistry Chemical Physics* **2011**, *13*, 11165.

(100) Deeg, K. S.; Jose Gutierrez-Sevillano, J.; Bueno-Perez, R.; Parra, J. B.; Ania, C. O.; Doblare, M.; Calero, S. *Journal of Physical Chemistry C* **2013**, *117*, 14374.

(101) Calero, S.; Martin-Calvo, A.; Hamad, S.; Garcia-Perez, E. *Chemical Communications* **2011**, *47*, 508.

(102) Martin-Calvo, A.; Lahoz-Martin, F. D.; Calero, S. *Journal of Physical Chemistry C* **2012**, *116*, 6655.

(103) Garcia-Sanchez, A.; Ania, C. O.; Parra, J. B.; Dubbeldam, D.; Vlugt, T. J. H.; Krishna, R.; Calero, S. *Journal of Physical Chemistry C* **2009**, *113*, 8814.

(104) Dubbeldam, D.; Calero, S.; Vlugt, T. J. H.; Krishna, R.; Maesen, T. L. M.; Smit, B. *Journal of Physical Chemistry B* **2004**, *108*, 12301.

(105) Rappe, A. K.; Casewit, C. J.; Colwell, K. S.; Goddard, W. A.; Skiff, W. M. *Journal of the American Chemical Society* **1992**, *114*, 10024.

(106) Mayo, S. L.; Olafson, B. D.; Goddard, W. A. *Journal of Physical Chemistry* **1990**, *94*, 8897.

Adsorptive Separation of Ethane and Ethylene Using Isoreticular Metal-Organic Frameworks

2

Francisco D. Lahoz-Martína, Sofía Calero, Juan José Gutiérrez-Sevillano, and Ana Martin-Calvo

This computational study focuses on the adsorption and diffusion of ethane and ethylene in IsoReticular Metal-Organic Frameworks (IRMOFs). We selected the IRMOFs family for the diversity of linkers, which allows understanding the effect that functionalized groups, ligand length, cyclic groups, or interpenetrating cavities has on the accessible pore volume of the structures and on the selective behaviour towards the components of the mixture. At atmospheric pressure and 298 K, we found that the smaller interpenetrated structures (IRMOF-9, -11, and -13) exhibit larger adsorption selectivity than their non-interpenetrated counterparts (IRMOF-10, -12, and 14, respectively). Based on these findings we discuss the advantages of using interpenetrating structures for ethane capture. On the other hand, structures with large pore volume such as IRMOF-16 seem to reverse the adsorption selectivity in favour of ethylene.

1. Introduction

Mixtures containing ethane and ethylene are often found in industrial processes.[1] The importance of this separation in the industrial production of ethylene is evident taking into account the amount of ethylene produced annually worldwide, well over 140 million tons.[2] The uses of ethylene range from chemical synthesis (polyethylene production)[3] to food industry, since this molecule has a direct effect in the ripening of fruits.[4] Nowadays, the separation of these two compounds is carried out through high-cost processes.[1] This work analyses the advantages of using crystalline molecular sieves to enhance the ethane/ethylene separation efficiency. Previous studies reflect promising results originated from the use of zeolites.[5-7] However, the performance of Metal-Organic Frameworks (MOFs) in the separation of ethane and ethylene has not been extensively studied, with only a few recent works addressing olefin/paraffin separation using this type of materials.[8-15] Among MOFs, the use of IsoReticular Metal-Organic Frameworks (IRMOFs) in the separation of this mixture has not been studied yet. To the best of our knowledge only IRMOF-8 has been considered for this separation, but without encouraging results.[10,16,17]

The main goal of this work is to identify suitable IRMOFs for the separation process of ethane and ethylene. The high tunability of IRMOFs places this family of materials as potential candidates to perform separations of molecules with small differences in size and volatility but with different applications of their derivatives, such as ethane/ethylene. The IRMOF family was first synthesized by Yaghi *et al.*[18] These structures have a 3D network consisting of a cubic array of $Zn_4O(CO_2)_6$ units connected by different organic linkers. The linkage of the Zn_4O complexes is forced to alternate between linkers pointing outwards and inwards, resulting in a structure with two alternating cavities of different sizes. Several uses have been described for this family of MOFs, most of them in the field of adsorption and storage of gases.[19,20] Previous studies show the performance of these materials for methane or hydrogen storage, and the strong relation of the storage capacity with the pore volume and the surface area.[18,21]

This work deals with the adsorption and separation capacity of the IRMOFs-n, (n=1-16). A particularity of some of these MOFs is that their organic linkers are functionalized, affecting therefore to their adsorptive and diffusion properties. Among these frameworks, IRMOF-1 is the simplest, well-known structure. This MOF has been widely studied in terms of gas adsorption for separation and storage.[19,22-24] The organic linker of IRMOF-1 is 1,4-benzenedicarboxylate and its orientation defines two cages of about 11 Å and 15 Å in diameter. IRMOFs-n (n=2-5) contain the same linker and therefore, have Pore Size Distributions (PSDs) similar to IRMOF-1 (Figure A1 from Appendix 1). Differences between structures are due to the chemical composition of functionalized groups in the phenyl ring. IRMOF-2 and -3 have bromine and amine groups, respectively. These small functional groups slightly reduce the size of their smallest cavities, being about 10 Å in diameter. IRMOF-4 and -5 have 2,5-propanoyl-1,4-benzenedicarboxylate and 2,5-pentanoyl-1,4-benzenedicarboxylate as linkers, respectively. In these structures the big cavity of 15 Å in diameter disappears, being occupied by the functional group of the linker. Therefore, the adsorption in these structures is limited to the cavities of about 10 Å in diameter. IRMOF-10 and -16 resemble IRMOF-1, but with increasing number of phenyl groups (2 phenyl groups in IRMOF-10, and 3 phenyl groups in IRMOF-16). The PSDs of these two structures evidence wide pores because of the largest length of the organic linkers. IRMOF-10 contains cages of about 17 Å and 20 Å in diameter, while the cavities of IRMOF-16 are about 23 Å and 25 Å in diameter (Figure A2 from Appendix 1). IRMOF-7 and -8 have a naphthalene group, connected through a double bond, but the groups are connected to each other differently. In the case of IRMOF-7 the carbon atoms connected to the two metallic centres are located in the same benzene ring, while for IRMOF-8 each cyclic group connects to one metallic centre. The conformation of the linker molecules leads to differences in the pores as showed on the PSD obtained for the two structures (Figure A3 from the Appendix 1). IRMOF-7 has one single type of cavities of 10 Å in diameter, while IRMOF-8 has cavities of about 13 Å and 18 Å in diameter. IRMOF-6 is another structure with two cyclic groups. The ligand of the structure is benzocyclobutene dicarboxylate, and the PSD evidences cavities of about 10 Å and 15 Å in diameter (Figure A4 from Appendix 1). IRMOF-12 and -14 have hexahydropyrene dicarboxylate and pyrene dicarboxylate as linkers, respectively. The main difference between these structures is the delocalization of the double bonds in the linker that affects to the total number of hydrogen atoms of each structure. As expected, the PSD obtained for the two structures is very similar, indicating cavities of 15 Å and 20 Å in diameter for IRMOF-14. The largest cavities are a bit smaller for IRMOF-12, since this structure contains more hydrogen atoms (Figure A5 from Appendix 1). IRMOF-9, -11, -13, and -15 are like IRMOF-10, -12, -14, and -16, respectively, but with interpenetrating cavities. The resulting PSDs for these structures show a variety of cavities of 12 Å in diameter at maximum. (Figure A6 from Appendix 1).

In this work, we provide the adsorption capacity of the 16 IRMOFs for ethane and ethylene as well as the separation performance for the mixtures at room temperature. The study is based on the adsorption and diffusion of the two gases within the pores of the structures.

2. Simulation methods and models

Simulations are performed with the RASPA code.[25] Pore Size Distributions (PSDs), surface areas (SSA) and pore volumes were calculated using the RASPA code. Details of the simulation methods can be found elsewhere in literature.[26-28] Adsorption isotherms are calculated using Monte Carlo (MC) simulations in the grand canonical ensemble. In this ensemble, chemical potential, volume, and temperature are kept fixed to obtain the number of adsorbed molecules. MC simulations are performed with 10^6 simulation cycles. Pressure is related to fugacity by the Peng—Robinson equation of state. The MC simulations allow moves of insertion, deletion, rotation, translation, reinsertion and identity change (for mixtures). The self-diffusion of the molecules in the structures is calculated with Molecular Dynamics (MD). MD simulations are carried out in the NVT ensemble, for 2 x 10^7 cycles and 0.0005 ps of time step. We use the Nosé-Hoover thermostat.[29,30] Atomic interactions are described by Lennard-Jones parameters, using Lorentz-Berthelot mixing rules for crossed Lennard-Jones parameters. The cut-off is 12 Å.

We use united atom models for ethane and ethylene, with CHx groups (CH_3 and CH_2) as a single interaction centres. For ethane, we use the model previously reported by Dubbeldam *et al.*[31] with Lennard Jones parameters σ = 3.76 Å and ε/kB = 108 (K), and a fixed bond length of 1.54 Å. We tested this flexible model and its equivalent rigid (avoiding bond stretch), obtaining identical results in the adsorption and diffusion properties calculated. The model for ethylene was reported by Liu *et al.*[32] with bond length fixed at 1.33 Å. The adsorbate-adsorbate Lennard Jones parameters are σ = 3.685 Å and ε/kB = 93 K. As first step to validate the molecular models, we calculated the vapour-liquid equilibrium curves of these hydrocarbons using Gibbs ensemble MC simulations. Our results are in agreement with the experimental values (Figure A7 from Appendix 1). To consider the possible effect of a charged model, alongside the model described for ethylene, we tested a similar charged neutral variant with point charges in the position of the CH_2 groups and a dummy atom in the middle (0.665 Å distance to each CH_2 group) to compensate charges, reproducing the experimental quadrupole moment of the molecule, resulting both of them on nearly identical results. Therefore, and to keep consistency with the model employed for ethane, we use the model of ethylene reported by Liu *et al.*[32] The accuracy of the adsorbate-absorbent interactions of ethane and IRMOF-1 was validated in previous publications.[33,34] However, no experimental isotherms of ethylene have been found on the IRMOFs under

Table 1. Henry coefficients, entropies and energies of adsorption computed at zero coverage for the different sites of Cu-BTC at 298 K. Number in brackets gives the statistical errors in the last digits.

Structure	a (Å)	b (Å)	c (Å)	α	β	γ	PV (cm³/g)	SSA (m²/g)
IRMOF-1	25.832	25.832	25.832	90	90	90	1.355	3587.686
IRMOF-2	25.772	25.772	25.772	90	90	90	1.002	2745.550
IRMOF-3	25.746	25.746	25.746	90	90	90	1.240	3389.715
IRMOF-4	25.849	25.849	25.849	90	90	90	0.582	1437.869
IRMOF-5	25.764	25.764	25.764	90	90	90	0.374	860.532
IRMOF-6	25.842	25.842	25.842	90	90	90	1.161	3065.531
IRMOF-7	25.829	25.829	25.829	90	90	90	1.036	3331.311
IRMOF-8	30.091	30.091	30.091	90	90	90	1.897	4378.549
IRMOF-9	17.147	23.322	25.255	90	90	90	1.145	3386.760
IRMOF-10	34.281	34.281	34.281	90	90	90	2.688	4939.373
IRMOF-11	24.822	42.992	56.734	90	90	90	0.889	2535.385
IRMOF-12	34.281	34.281	34.281	90	90	90	2.275	5207.668
IRMOF-13	24.822	24.822	56.734	90	90	120	0.956	2727.847
IRMOF-14	34.381	34.381	34.381	90	90	90	2.370	4826.415
IRMOF-15	21.459	21.459	21.459	90	90	90	2.147	6079.604
IRMOF-16	42.981	42.981	42.981	90	90	90	4.478	6063.294

study. To the best of our knowledge, the only set of adsorption isotherms of ethylene in IRMOF-8 was reported by Pires *et al.*[17] although, they use an interpenetrated version of the structure which is not the one used in this work. Figure A8 from Appendix 1 compares the adsorption isotherms in IRMOF-8 obtained from an equimolar binary mixture (non-interpenetrated structure) with previous simulation data taken from the work of Pillai *et al.*[16]

The adsorbents were considered as rigid structures, using the reported crystallographic position of the atoms for each structure.[18] We acknowledge that large ligands like these of IRMOF-4 and -5 may show flexibility. However, there is no existing model to reproduce flexibility in these structures, and therefore we employ this rigid approach. The Lennard-Jones parameters are taken from UFF generic force field[35] and for the interactions with the adsorbates we use Lorentz-Berthelot mixing rules. Table 1 contains the unit cell parameters of the structures as well as pore volumes and surface areas, calculated with helium probes.

3. Results

The adsorption and separation performance of these MOFs is analysed in terms of a) existence of functionalized groups (IRMOF-n, n=1-5), b) ligand length (IRMOF-1, -10, and -16), c) connections between two cyclic groups (IRMOF-10, -7, and -8), d) type of cyclic groups (IRMOF-6 and -7), e) delocalization of double bonds in ligands with four cyclic groups (IRMOF-12 and -14), and f) interpenetrating structures (IRMOF-9, -11, -13, -15). The Henry Coefficients (K_H) for ethane and ethylene were calculated at 298 K and zero loading (Figure 1). Ethane exhibits the highest values of K_H for all the structures. The values K_H calculated for ethylene are also high for small interpenetrated structures (IRMOF-9, -11, and -13), and for structures with non-accessible large cavities (IRMOF-4 and -5).

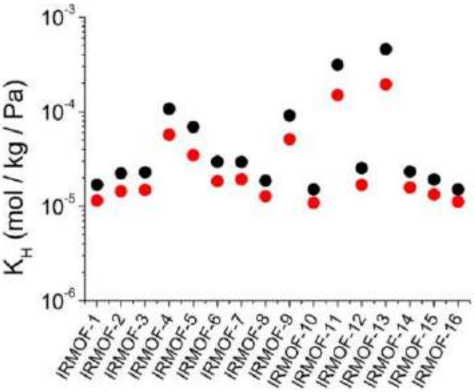

Figure 1. Henry coefficients of ethane (black) and ethylene (red) at 298K.

The calculated adsorption isotherms for the equimolar mixture at 298 K are shown in Figures 2-5. All the structures show preferential adsorption for ethane over ethylene. This can be explained by the presence of a double bond in the alkene, which shortens the molecule. Ethane is also defined by larger interaction centres due to the additional hydrogen atoms embedded in the pseudo atoms. The isotherms obtained for the first group of structures are shown in Figure 2. The largest difference between the adsorption of ethane and ethylene in the structures of this group occurs at

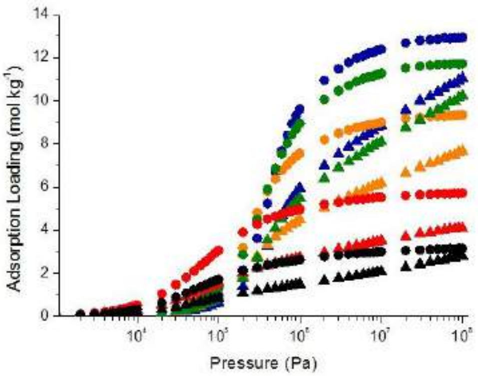

Figure 2. Adsorption isotherms of the equimolar mixture of ethane (circles) and ethylene (triangles) at 298K in IRMOF-1 (blue), IRMOF-2 (orange), IRMOF-3 (green), IRMOF-4 (red), and IRMOF-5 (black).

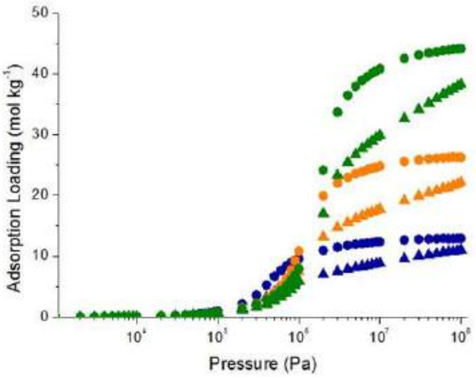

Figure 3. Adsorption isotherms of the equimolar mixture of ethane (circles) and ethylene (triangles) at 298K in IRMOF-1 (blue), IRMOF-10 (orange), and IRMOF-16 (green).

values of pressure in the range from $6 \cdot 10^5$ Pa to $3 \cdot 10^6$ Pa. Direct measurements of the distances between the carbon atom of the phenyl ring were the functional group is connected and the farthest atom of each functional group (Table A1 in Appendix 1) indicate that the structures with larger functional groups exhibit lower adsorption capacity. The available surface area of the structures is directly related to the size of the functional groups (see Table 1) and consequently, differences in the adsorption of ethane and ethylene decrease for C5-alkyl < C3-alkyl < Br < NH_2.

Figure 3 shows the adsorption isotherms for the equimolar mixture in the structures of the second group. The structure with the longest ligand exhibits the largest saturation capacity. Hence, the saturation capacities of IRMOF-10 and IRMOF-16 are respectively two and three times the saturation capacity of IRMOF-1. This is directly related to the differences between the pore volumes of the three structures (Table 1).

The largest variations between the adsorption of ethane and ethylene are found in the interval of pressure from $3 \cdot 10^6$ Pa to $6 \cdot 10^6$ Pa, with differences twice larger than at saturation. In the case of structures with two cyclic groups with different connections to the metallic centres the adsorption capacity is related to the length of the linker (Figure 4). The highest adsorption capacity is obtained for IRMOF-10 (structure with ligands of 7.047 Å in length) followed by IRMOF-8 (with ligand of 5.013 Å in length), and IRMOF-7. The latter structure has two cyclic groups in the organic linker, but one single ring connects with the metal centres, leading to an effective ligand length of only 2.607 Å. IRMOF-1 and -

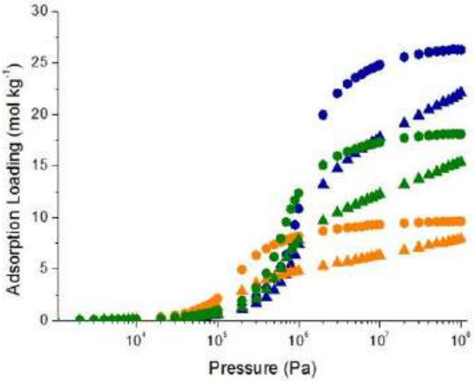

Figure 4. Adsorption isotherms of the equimolar mixture of ethane (circles) and ethylene (triangles) at 298 K in IRMOF-10 (blue), IRMOF-7 (orange), and IRMOF-8 (green).

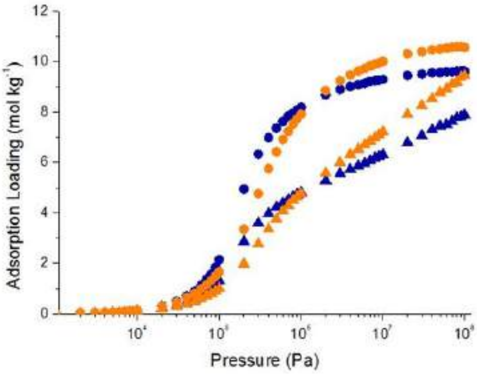

Figure 5. Adsorption isotherms of the equimolar mixture of ethane (circles) and ethylene (triangles) at 298K in IRMOF-7 (blue) and IRMOF-6 (orange).

7 are similar in terms of ligand length. However, the second cyclic group of IRMOF-7 occupies part of the available space in the structure and this leads to lower values of adsorption (Figure A9 from Appendix 1). The structures with two different cyclic groups in the organic linkers, IRMOF-6 and -7, show similar adsorption (Figure 5), but IRMOF-6 exhibits slightly larger saturation capacity than IRMOF-7. As observed from the PSD (Figures A3 and A4 from Appendix 1) these two structures contain cavities of about 10 Å in diameter, but larger cavities of 15 Å are also accessible in IRMOF-6. These cavities result from the size of the heterocycles, with 6- and 4-member rings for IRMOF-6 and only 6-member rings for IRMOF-7. The largest difference between the adsorption of ethane and ethylene is found at $2 \cdot 10^6$ Pa in both structures, being IRMOF-7 the structure with the best separation performance. IRMOF-12 and -14 show similar trends in the adsorption of ethane and ethylene, since the main difference between them is the delocalization of the double bonds of the linkers (Figure A10 from Appendix 1) and this delocalization does not affect adsorption when the adsorbates are non-polar.

The almost negligible difference between the adsorption of ethane and ethylene in the two structures (IRMOF-12 < IRMOF-14) could be attributed to the number of hydrogen atoms that form part of the framework, that is larger for IRMOF-12. In the case of interpenetrated structures the adsorption capacities of IRMOF-9, -11, -13, and -15 are less than half of their non-interpenetrating counterparts (Figure A11 from Appendix 1), as can be deduced from the PSDs of the frameworks.

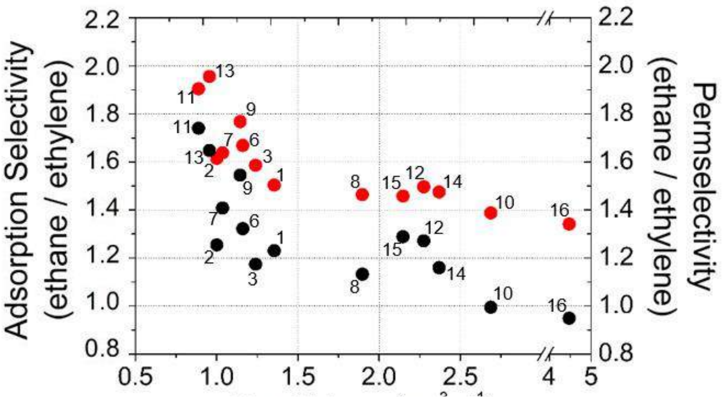

Figure 6. Ethane/ethylene adsorption selectivity (red) and permselectivity (black) obtained from the adsorption of equimolar mixtures at 298 K and 100 kPa. Selectivity for the IRMOFs is represented as a function of the pore volume of the structures.

Figure 6 shows the adsorption selectivity of ethane over ethylene at 100 kPa as a function of the pore volume of the structures. In all cases the selectivity values are larger than 1, indicating the preferential adsorption of ethane previously observed form the calculated adsorption isotherms. It is interesting to note that the structures with small pore volumes exhibit high selectivity for ethane, proving the role of the entropy on the adsorption/separation process. The observed effect is due to both, entropy and enthalpy differences caused by enhanced dispersion interactions for ethane. We could state that enthalpy is essential at low pressure whereas entropy prevails at saturation. The main differences between the molecules of ethane and ethylene reside in the length of the molecule and in the size of the interaction centre. Therefore the structures where one of the adsorbates fits better than the other exhibit highest adsorption selectivity for the former. Ethane is slightly larger than ethylene, entering the IRMOF cavities at lower values of pressure. IRMOFs are structures with large surface areas. This is usually related to the lack of preferential adsorption sites for small hydrocarbons and low adsorption selectivity. However, this scenario changes for the diffusion of the molecules within the pores. As observed in Figure 6 all structures reduce the selectivity towards ethane when considering molecular diffusion. We calculate the self-diffusion coefficients of the adsorbates, using mixture compositions equivalent to the results of the binary adsorption at 10^5 Pa and 298 K. Particularly, IRMOF-4 and -5 are automatically excluded as diffusion is prevented by the presence of the large functional groups in the organic ligands (Table A2 from Appendix 1). In this case, our rigid model for the structures does not account for flexibility in the linker chain, which could otherwise allow a certain diffusion of the adsorbates.

The calculated self-diffusion coefficients for IRMOF-8 agree with the gas chromatography study carried out by Pires *et al.*[17] In this study, higher diffusion of ethylene is also observed for an equimolar mixture of ethane/ethylene. The diffusion selectivity of ethylene over ethane is 1.56 at 301 K and atmospheric pressure while our simulations provide a selectivity of 1.30 at 298 K and 10^5 Pa. IRMOF-10 and -16 show values of selectivity below 1, indicating permselectivity towards ethylene in these structures.

The molecules of ethylene diffuse much faster than the molecules of ethane in IRMOF-10 and -16, and these differences in diffusion hinder the adsorption selectivity in favour of ethane that we previously stated. The remaining structures exhibit permselectivity towards ethane. Since molecular diffusion is crucial for efficient adsorption/separation processes, we identify IRMOF-11 and -13 as the structures with optimal separation performance based on permselectivity. We also put the focus on IRMOF-16 for being the only structure with selective behaviour towards ethylene.

The last part of our study is to analyse the performance of IRMOF-11, IRMOF-13 and IRMOF-16 for the separation of ethane/ethylene mixtures at working conditions of 298 K and 100 kPa. The ethane/ethylene concentrations in the reservoir range from 10:90 to 90:10. Figure 7 shows the adsorption selectivity obtained for these mixtures in the three structures. Adsorption selectivity is obtained from the adsorption loading of the two adsorbates, using the following expression: $S_{i/j} = \frac{\theta_i}{\theta_j} \cdot \frac{X_j}{X_i}$ where $\boldsymbol{\theta_i}$ and $\boldsymbol{\theta_j}$ are the adsorption loadings of molecules i and j; and $\boldsymbol{X_i}$, $\boldsymbol{X_j}$ are the molar fractions.

IRMOF-13 is the structure with the highest adsorption selectivity for ethane, followed by IRMOF-11. Apart from IRMOF-4 and -5, excluded here for preventing the diffusion of ethane and ethylene, IRMOF-13 and 11 have the smallest pore volume of the structures used because of their interpenetrating cavities. This generates frameworks with small cavities and crannies that favour the adsorption of molecules. Besides the large main cavities, these structures contain small cavities non-existent in other interpenetrated IRMOFs (see PSDs of Figure A6 from Appendix 1) explaining the differences in adsorption and the optimal separation performance. The

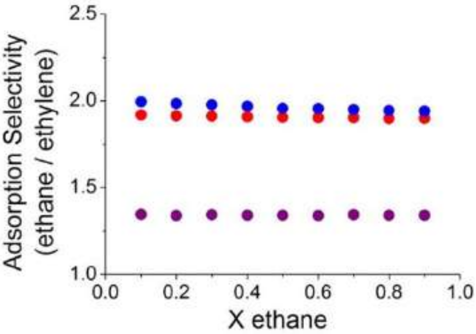

Figure 7. Ethane/ethylene adsorption selectivity obtained from the adsorption of the binary mixtures at 298 K and 100 kPa in IRMOF-11 (red), -13 (blue), and -16 (purple).Adsorption isotherms of the equimolar mixture of ethane (circles) and ethylene (triangles) at 298 K in IRMOF-10 (blue), IRMOF-7 (orange), and IRMOF-8 (green).

low adsorption selectivity in IRMOF-16 relative to that of IRMOF-11 and IRMOF-13 is yet another sign of the entropic effect during adsorption, as this structure has the largest pore volume out of the three. We found tiny dependence of the selective behaviour with the molar fractions of the mixture in IRMOF-13. This dependence is negligible for the structures with larger pore volumes. The adsorption selectivity obtained for all the IRMOFs can be found in Table A3 from Appendix 1. When including molecular diffusion, we observe that all the structures reduce their selective performance (Table A4 from Appendix 1). To calculate the permselectivity of ethane over ethylene, we use the following equation:

$$Permselectivity_{i/j} = \frac{\theta_i}{\theta_j} \cdot \frac{X_j}{X_i} \cdot \frac{D_i}{D_j}$$

where $\boldsymbol{\theta_i}$ and $\boldsymbol{\theta_j}$ are the adsorption loadings of molecules i and j; $\boldsymbol{X_i}$, $\boldsymbol{X_j}$ are the molar fractions; and $\boldsymbol{D_i}$, $\boldsymbol{D_j}$are the diffusion coefficients.

Regarding the diffusion coefficients obtained for the selected structures, Figure 8 shows the values obtained for ethane and ethylene for mixtures with several molar fractions. As can be seen, in structures with small cages and interpenetrating cavities (IRMOF-11 and -13) diffusion is slower. As the two adsorbates have almost the same size, large differences are not observed (the molecules of ethylene diffuse slightly faster than the molecules of ethane due to their relatively smaller size). Variations attributed to the composition of the mixture are negligible. On the contrary, differences between the diffusion coefficients of ethane and ethylene in IRMOFs with large pore volume are remarkable, especially for IRMOF-16 that is the structure with the largest accessible volume. The diffusion coefficients calculated for ethane and ethylene in all IRMOFs are collected in Table A2 from Appendix 1. As shown in Figure 9, IRMOF-11 and -13 exhibit the largest

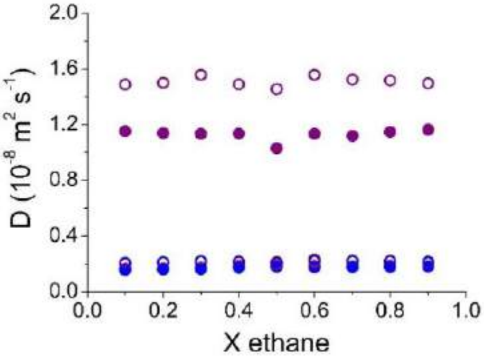

Figure 8. Self-diffusion coefficients of ethane (full symbols) and ethylene (empty symbols) in IRMOF-11 (red), -13 (blue), and -16 (purple) at 298 K. The number of molecules was taken from the adsorption isotherms of the binary mixtures at 100 kPa.

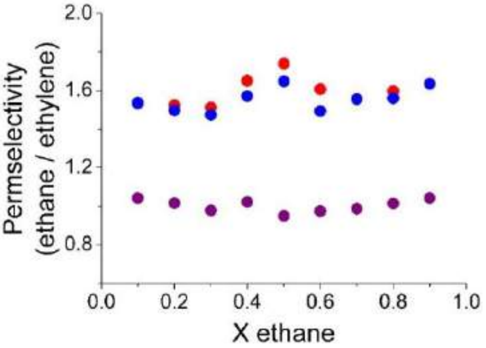

Figure 9. Ethane/ethylene permselectivity obtained from the binary mixtures at 298 K and 100 kPa in IRMOF-11 (red), -13 (blue), and -16 (purple).

adsorption selectivity and the lowest molecular diffusion. This implies large permselectivity, allowing the adsorption of ethane and the release of ethylene. On the other hand, the adsorption selectivity for IRMOF-16 is low since the molecular diffusion within the pores of the structure is large, and overall, slightly selective in favour of ethylene.

Conclusions

Based on molecular simulations we point out that IRMOFs with interpenetrated cavities are interesting materials for the separation of ethane/ethylene mixtures. This agrees with the conclusion reached by Pillai *et al.*[16] about the enhancement in the selectivity of ethane for interpenetrated structures. These structures exhibit the perfect combination of pore volume and crannies that favours the adsorption of specific small molecules. We found that IRMOF-11 and -13 are the structures for the optimal separation of ethane from ethylene. We also showed that the presence of large functional groups in the organic linkers can severely affect the diffusion of small molecules such as ethane and ethylene. Structures with large cavities as IRMOF-16 could invert ethane/ethylene selectivity, slightly preferring ethylene when considering the diffusion of the adsorbates.

Bibliography

(1) Salgado-Gordon, H.-J.; Valbuena-Moreno, G. *Ct&F-Ciencia Tecnologia Y Futuro* **2011**, *4*, 73.

(2) True, W. R. *Oil Gas J.* **2012**, *110*.

(3) Xie, T. Y.; McAuley, K. B.; Hsu, J. C. C.; Bacon, D. W. *Industrial & Engineering Chemistry Research* **1994**, *33*, 449.

(4) Kim, J.; Chang, C.; Tucker, M. L. *Frontiers in Plant Science* **2015**, *6*.

(5) Berlier, K.; Olivier, M. G.; Jadot, R. *Journal of Chemical and Engineering Data* **1995**, *40*, 1206.

(6) Kim, J.; Lin, L.-C.; Martin, R. L.; Swisher, J. A.; Haranczyk, M.; Smit, B. *Langmuir* **2012**, *28*, 11923.

(7) Aguado, S.; Bergeret, G.; Daniel, C.; Farrusseng, D. *Journal of the American Chemical Society* **2012**, *134*, 14635.

(8) Zhang, Y.; Li, B.; Krishna, R.; Wu, Z.; Ma, D.; Shi, Z.; Pham, T.; Forrest, K.; Space, B.; Ma, S. *Chemical Communications* **2015**, *51*, 2714.

(9) Martins, V. F. D.; Ribeiro, A. M.; Ferreira, A.; Lee, U. H.; Hwang, Y. K.; Chang, J.-S.; Loureiro, J. M.; Rodrigues, A. E. *Separation and Purification Technology* **2015**, *149*, 445.

(10) Liao, P.-Q.; Zhang, W.-X.; Zhang, J.-P.; Chen, X.-M. *Nature Communications* **2015**, *6*.

(11) Pires, J.; Pinto, M. L.; Granadeiro, C. M.; Barbosa, A. D. S.; Cunha-Silva, L.; Balula, S. S.; Saini, V. K. *Adsorption-Journal of the International Adsorption Society* **2014**, *20*, 533.

(12) Li, P.; He, Y.; Arman, H. D.; Krishna, R.; Wang, H.; Weng, L.; Chen, B. *Chemical Communications* **2014**, *50*, 13081.

(13) Huang, L.; Cao, D. *Journal of Materials Chemistry A* **2013**, *1*, 9433.

(14) Yoon, J. W.; Seo, Y.-K.; Hwang, Y. K.; Chang, J.-S.; Leclerc, H.; Wuttke, S.; Bazin, P.; Vimont, A.; Daturi, M.; Bloch, E.; Llewellyn, P. L.; Serre, C.; Horcajada, P.; Greneche, J.-M.; Rodrigues, A. E.; Ferey, G. *Angewandte Chemie-International Edition* **2010**, *49*, 5949.

(15) Weston, M. H.; Colon, Y. J.; Bae, Y.-S.; Garibay, S. J.; Snurr, R. Q.; Farha, O. K.; Hupp, J. T.; Nguyen, S. T. *Journal of Materials Chemistry A* **2014**, *2*, 299.

(16) Pillai, R. S.; Pinto, M. L.; Pires, J.; Jorge, M.; Gomes, J. R. B. *Acs Applied Materials & Interfaces* **2015**, *7*, 624.

(17) Pires, J.; Pinto, M. L.; Saini, V. K. *Acs Applied Materials & Interfaces* **2014**, *6*, 12093.

(18) Eddaoudi, M.; Kim, J.; Rosi, N.; Vodak, D.; Wachter, J.; O'Keeffe, M.; Yaghi, O. M. *Science* **2002**, *295*, 469.

(19) Rosi, N. L.; Eckert, J.; Eddaoudi, M.; Vodak, D. T.; Kim, J.; O'Keeffe, M.; Yaghi, O. M. *Science* **2003**, *300*, 1127.

(20) Karagiaridi, O.; Lalonde, M. B.; Bury, W.; Sarjeant, A. A.; Farha, O. K.; Hupp, J. T. *Journal of the American Chemical Society* **2012**, *134*, 18790.

(21) Frost, H.; Dueren, T.; Snurr, R. Q. *Journal of Physical Chemistry B* **2006**, *110*, 9565.

(22) Luebbers, M. T.; Wu, T.; Shen, L.; Masel, R. I. *Langmuir* **2010**, *26*, 11319.

(23) Zhao, Z.; Li, Z.; Lin, Y. S. *Industrial & Engineering Chemistry Research* **2009**, *48*, 10015.

(24) Sarkisov, L. *Dalton Transactions* **2016**, *45*, 4203.

(25) Dubbeldam, D.; Calero, S.; Ellis, D. E.; Snurr, R. Q. *Molecular Simulation* **2016**, *42*, 81.

(26) Walton, K. S.; Snurr, R. Q. *Journal of the American Chemical Society* **2007**, *129*, 8552.

(27) Sarkisov, L.; Harrison, A. *Molecular Simulation* **2011**, *37*, 1248.

(28) Gelb, L. D.; Gubbins, K. E. *Langmuir* **1999**, *15*, 305.

(29) Nosé, S. *The Journal of Chemical Physics* **1984**, *81*, 511.

(30) Hoover, W. G. *Physical Review A* **1985**, *31*, 1695.

(31) Dubbeldam, D.; Calero, S.; Vlugt, T. J. H.; Krishna, R.; Maesen, T. L. M.; Beerdsen, E.; Smit, B. *Physical Review Letters* **2004**, *93*.

(32) Liu, B.; Smit, B.; Rey, F.; Valencia, S.; Calero, S. *Journal of Physical Chemistry C* **2008**, *112*, 2492.

(33) Dubbeldam, D.; Frost, H.; Walton, K. S.; Snurr, R. Q. *Fluid Phase Equilibria* **2007**, *261*, 152.

(34) Martin-Calvo, A.; Garcia-Perez, E.; Manuel Castillo, J.; Calero, S. *Physical Chemistry Chemical Physics* **2008**, *10*, 7085.

(35) Rappe, A. K.; Casewit, C. J.; Colwell, K. S.; Goddard, W. A.; Skiff, W. M. *Journal of the American Chemical Society* **1992**, *114*, 10024.

Effect of Light Gases in the Ethane/Ethylene Separation Using Zeolitic Imidazolate Frameworks

Francisco D. Lahoz-Martín, Ana Martín-Calvo, Juan José Gutiérrez-Sevillano, and Sofía Calero

3

We use molecular simulations to study the adsorption of ethane and ethylene in zeolitic imidazolate frameworks. The separation of these two compounds is a crucial step in many industrial processes, most of them related to production of ethylene. Separation methods such as fractional cryogenic distillation require of large energy consumption which increases the costs of ethylene production. Here we analyse the suitability of zeolitic imidazolate frameworks for the separation of these gases based on structural and chemical features. We pay special attention to the effect exerted by other gases on the adsorption and diffusion of ethane and ethylene in the structures. We found that nitrogen has an important role in the separation process, and depending on the structure it can enhance or hinder the adsorption selectivity for ethane. The presence of gasses other than nitrogen also causes an effect on the ethane/ethylene separation. A mixture containing hydrogen, oxygen, methane, carbon monoxide, carbon dioxide, ethane, and ethylene in zeolitic imidazolate frameworks is also investigated. Our results identify ZIFs with *rho, crg*, and *lta* topologies as good candidates for the separation of ethane and ethylene.

1. Introduction

The worldwide production of ethylene exceeds 140 million tons per year.[1] This olefin is one of the most used in industry, as it plays a role in the production of polyethylene, ethylene oxide, and ethylbenzene.[2] Ethylene is also a biologically active molecule acting as plant hormone involved in the ageing process.[3] It is used in the food industry to force the ripening of fruits.[4] Ethane, with a production of more than 5 million tons per year,[1] is usually found in mixtures with ethylene. The main process used to separate ethane from ethylene in industry is the fractional cryogenic distillation.[5] This process requires high levels of energy consumption, being the cryogenic distillation columns responsible for more than 25% of the total energy spent during gas separation. Therefore, finding alternative methods to achieve the separation is essential. One plausible option is the use of porous materials, such as zeolites or Metal Organic Frameworks as molecular sieves.[6,7] There is extensive work focused on the adsorption of ethane and ethylene, as well as in binary mixture separation in zeolites and MOFs.[8-19] A notable example is the experimental study carried out by Aguado *et al.* on silver type-A zeolite, where they achieve high selectivity of ethylene over ethane in ternary mixtures with nitrogen.[20]

The aim of this work is to study the performance of Zeolitic Imidazolate Frameworks (ZIFs) on the separation of ethane from ethylene. ZIFs are part of a still emerging group of Metal-Organic Frameworks (MOFs). These structures are closely related to zeolites as many of them have zeolite topology. ZIFs are formed by metallic centers of Zn or Co that are tetrahedrally coordinate by imidazolate ligands. The large variety of metal-imidazolate combinations are responsible from the vast number of structures that can be synthesized. Among other applications, ZIFs can be used in adsorption processes,[21] gas storage,[22] heterogeneous catalysis,[23,24] and as molecular sensors.[25]

We study the adsorption and separation capacity of ZIF-1, -2, -3, -4, -6, -10, -20, -22, -62, -68, -71, -80, -93, -96, and 97. These structures contain Zn as metallic center linked by ligands such as Iimidazole (Im), nitroimidazole (nIm), methylimidazole (mIm), 1,5-dicyclohexyl imidazole (dcIm), benzimidazole (bIm), hydroxymethylmethyl imidazole (hymeIm), 4-aldemethylimidazole (almeIm), cyanide amine imidazole (cyamIm), or purinate (pur). These linkers lead to large variety of topologies and pore sizes. For instance, ZIF-1, -2, -3, -4, -6, and -10 have imidazole (Im) as ligand, but their connections and orientations generate differences in the topologies (*crb, crb, dft, cag, gis*, and *mer*, respectively) and pore sizes (Figure A1 from Appendix 2). It should be noted that ZIF-4 exhibits thermal crystal-amorphous transition above 573 K.[26] Other structures may share the same topology and differ in linkers. This is the case of ZIF-71, -93, -96, and -97, structures with *rho* topology but with other functionalized imidazole (dcIm, almeIm, cyamIm, and hymeIm, respectively). The Pore Size Distribution (PSD) reveals that the four structures have main cavities between 16 and 17 Å in diameter (Figure A2 from Appendix 2). ZIF-20 and -22 are structures with lta topology and large linkers (pur and bIm, respectively). These structures show similar PSD with big cavities of 14 and 15 Å in diameter, and small cavities of about 7 Å limited by the ligand size (Figure A3 from Appendix 2). Structures formed by two types of linkers such as ZIF-62 (Im, bIm), ZIF-68 (nIm, bIm), and ZIF-80 (nIm, dcIm) are also studied. This situation favours the creation of a variety of cavities, as evidenced by the PSDs (Figure A4 from the Appendix 2).

We analyse the performance of the materials on the separation of ethane and ethylene from a) binary mixtures (50:50 and 60:40), b) ternary mixture with nitrogen (10:10:80), and c) seven-component mixture with similar composition than the resulting from flue gas in industrial processes - ethane (2.9%) / ethylene (4.2%) / methane (76.9%) / hydrogen (2.1%) / oxygen (3.7%) / carbon monoxide (0.5%) / carbon dioxide (9.7%).

2. Simulation methods and models

In this work we use molecular models for ethane and ethylene that were validated in previous works.[19,27,28] These models reproduce experimental properties of the gases such as liquid density as a function of temperature and vapour-liquid equilibria. Previous experimental adsorption data of ethane and ethylene in ZIF-8 are in agreement with the values obtained using these models (Figure A5 from Appendix 2).[18,29] Studies on adsorption and diffusion of the two hydrocarbons in this structure,[30,31] report the swing effect in the imidazolate linkers of the structure, opening a small window that connects the main cavities of the framework. From the molecular simulation point of view this structural flexibility could have major effect on dynamic properties. However, this effect is negligible on adsorption studies at room temperature, as evidenced by the agreement between experiments and simulations (Figure A5 from Appendix 2). Reported models that are well validated for adsorption in zeolites and MOFs were used for nitrogen,[32] hydrogen,[33] oxygen,[34] methane,[35] carbon monoxide,[36] and carbon dioxide.[37] Ethane, ethylene, and methane are modelled using a united atom approach, with CH_3 (ethane), CH_2 (ethylene), and CH_4 (methane) defined as single interaction centres. Nitrogen, hydrogen, oxygen, carbon monoxide, and carbon dioxide are described with full atom models. Nitrogen, oxygen, and carbon monoxide models include a dummy atom equidistant to the other two atoms. This dummy atom is needed to reproduce the multipole moment of the molecule. The model used for hydrogen also takes into account Feynman-Hibbs quantum corrections.[33] Table A1 from Appendix 2 lists the parameters and point charges of all the molecules. Lennard-Jones parameters and point charges of the structure are taken from transferable force fields and compiled in Tables A2 and A3 from Appendix 2.[38] We use rigid models for ZIFs, and the crystallographic positions are taken from the literature.[20,39] The calculated pore volume, surface area, helium void fraction, and topology of the structures are collected in Table A4 from Appendix 2.

We calculate Coulombic interactions with the Ewald summation method with a relative precision of 10^{-6}. Host-guest and guest-guest Lennard-Jones interactions are estimated using Lorentz-Berthelot mixing rules. The Lennard-Jones potential is cut and shifted at a cut-off distance of 12 Å.

To calculate adsorption isotherms, we performed Monte Carlo (MC) simulations in the grand canonical (GC) ensemble. In our simulations, we relate the pressure to the fugacity using the Peng-Robinson equation of state. Adsorption selectivity is inferred from the isotherms. Absolute adsorption is directly related to excess adsorption using the equation:[40]

$$Adsorption_{exc} = Adsorption_{abs} - \frac{PV}{zRT}$$

where P, V, and T are the pressure, volume and temperature of the system, R is the gas constant, and z is the gas compressibility.

Henry coefficients (K_H) and adsorption energies and entropy are obtained from MC simulations in the canonical ensemble and carried out at zero coverage using the Widom test-particle method.[41] Pore volumes, surface areas, pore size distributions, and helium void fractions of the structures are calculated using helium probes using the aforementioned Widom particle insertion method.

Molecular Dynamic (MD) simulations in the canonical ensemble (NVT) are used to estimate the self-diffusion coefficient of the adsorbates in the structures, integrating Newton's laws of motion using the velocity Vertlet algorithm. The temperature is fixed with the Nosé-Hoover thermostat.[42,43]

All simulations were carried out using the RASPA simulation code.[44]

3. Results

Deep knowledge on the distribution of the cavities of the ZIFs and their size is crucial to understand the adsorption and diffusion of guest molecules in these structures. Therefore, for accurate analysis of our simulation data we will refer to PSDs. Figure 1 shows the Henry coefficients of the adsorbates in the 15 structures at 298 K. The values of Henry coefficient obtained for nitrogen are, in all the structures, at least one order of magnitude lower than the values obtained for ethane and ethylene. This indicates that the molecules of nitrogen do not interact strongly with the structures. Ethane shows the highest values of Henry coefficient for all the adsorbents, i.e. the interaction with the atoms of the structures is stronger for ethane than for ethylene. The adsorption energies are compiled in Table A5 from Appendix 2.

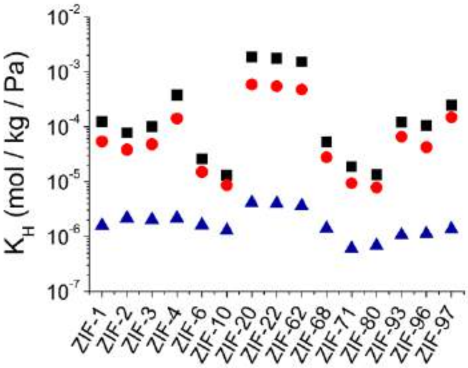

Figure 1. Henry coefficients of ethane (black squares), ethylene (red circles), and nitrogen (blue triangles) in several ZIFs at 298 K. Error bars are within the symbol size.

Adsorption isotherms are calculated at pressures ranging from 10^2 to 10^6 Pa for pure components, binary mixtures of ethane and ethylene (50:50 and 60:40), and a ternary mixture of ethane, ethylene, and nitrogen (10:10:80) at 298 K. Absolute adsorption data is converted to excess adsorption following the equation noted in the Models and Methods section. The results obtained are depicted in Figures 2-4 and Figures A6-A10 from Appendix 2. Following the same trend found for the adsorption energy, pure component adsorption isotherms (Figure 2, Figures A6 and A7 from Appendix 2) show that the adsorption of nitrogen is notably lower than the adsorption of ethane and ethylene for all the structures. Ethane is adsorbed over ethylene in most of the pressure range. For the structures that

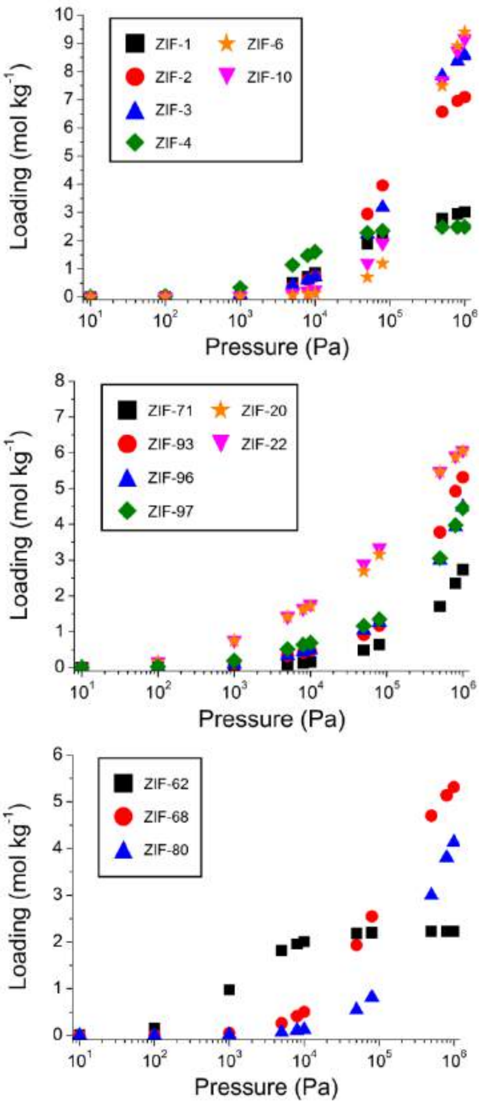

Figure 2. Adsorption isotherms of ethane in several ZIFs at 298 K. Error bars are within the symbol size.

reach saturation at the conditions used in this study (ZIF-1, -2, -4, -20, -22, and -62), the loading of ethane and ethylene at 10^6 Pa is similar. Overall, similar trends have been found comparing the results for ethane, ethylene, and nitrogen.

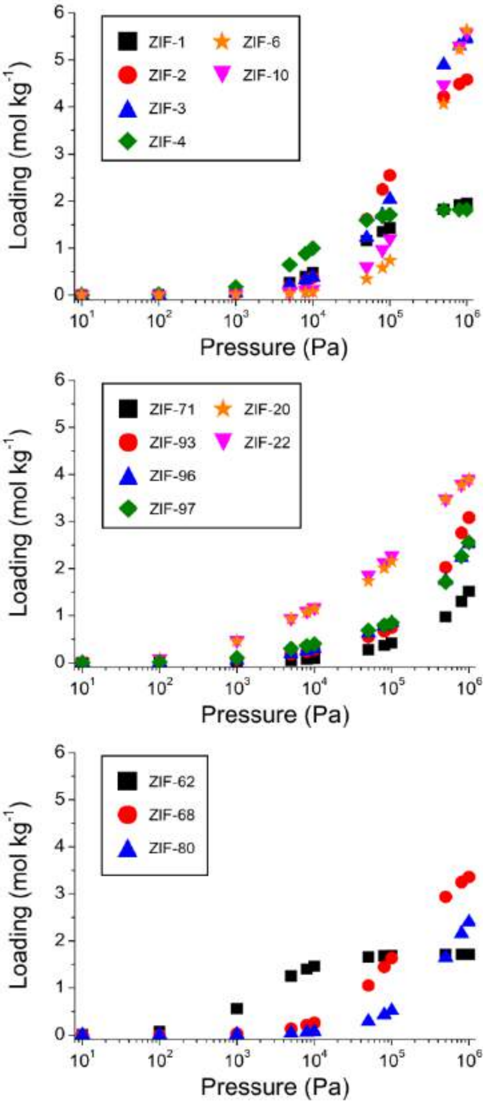

Figure 3. Adsorption isotherms of ethane from the binary equimolar mixture in several ZIFs at 298 K. Error bars are within the symbol size.

Focusing on the results for ethane, we discuss the adsorption and separation performance of each structure. Structures with Im as sole linker are depicted in Figure 2 (top). ZIF-1 and ZIF-4 reach a plateau at 10^5 Pa, and the adsorption loading in both structures is one third of that for ZIF-2, -3, -6, or -10. This is due to the limited void space available inside these two structures (Table A4 from Appendix 2). Figure 2 (middle) shows the results from structures with *lta* or *rho* topology, which are also the structures with the largest pore diameters. ZIF-20 and -22 (*lta*, pores of ~15 Å) exhibit the highest values of loading, especially at 10^3 and 10^5 Pa. At these values of pressure, their pores can be filled by guest molecules more easily than these of ZIF-71, -93, -96, and -97 (*rho*, pores of 16 to 17 Å). Three structures, ZIF-62, -68, and -80, are depicted in Figure 2 (bottom). From this set, ZIF- 62 is saturated at 10^4 Pa, whereas ZIF-68 and -80 (*gme* topology) do not reach saturation at 10^6 Pa, the highest value of pressure under study. An overall preference towards the adsorption of ethane is also supported by the results from the binary and ternary mixtures.

The adsorption isotherms of the 50:50 and 60:40 binary mixtures (Figure 3 and Figures A8 and A9 from Appendix 2) show that ethane is the most adsorbed gas in the complete pressure range. As expected, the difference between the uptake of ethane and ethylene is larger for the 60:40 mixture than for the 50:50 mixture for all the structures.

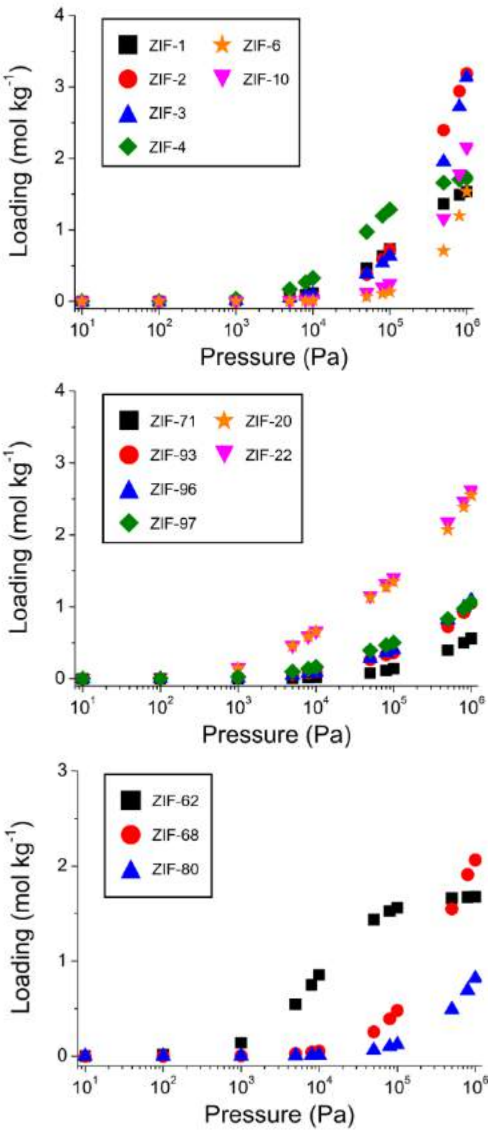

Figure 4. Adsorption isotherms of ethane from a mixture containing 10% ethane, 10% ethylene and 80% nitrogen in several ZIFs at 298 K. Error bars are within the symbol size.

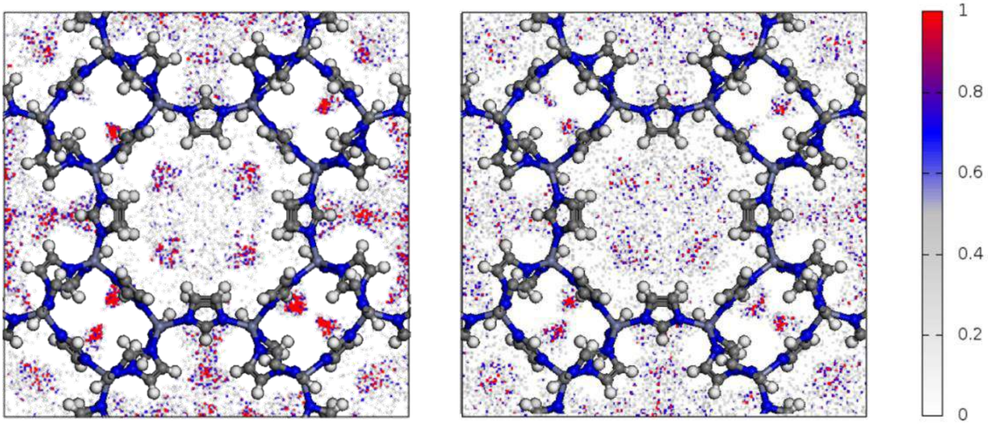

Figure 5. Distribution profile of ethylene (left) and nitrogen (right) in ZIF-10 from the 10:10:80 ethane/ethylene/nitrogen mixture at 106 Pa and 298 K.

Based on previous studies for separation of ethane and ethylene using zeolites,[20] we performed additional simulations adding nitrogen. The goal was to evaluate the effect of this gas in the adsorption selectivity. Simulations were carried out for a 10:10:80 ethane/ethylene/nitrogen mixture and the obtained results are depicted in Figure 4 as well as in Figure A9 from Appendix 2. As shown in Figure 4, the adsorption of ethane in the ternary mixture has noticeable differences compared to the adsorption of the pure component (Figure 2) and binary mixtures (Figure 3). In the first group of structures, with Im linker (Figure 4 (top)), previous marked difference between the loading of ethane in structures with higher (ZIF-2, -3, -6, and -10) and lower (ZIF-1, -4) void fractions disappears. For these structures, the loading of ethane in the ternary mixture varies between 2 and 3.5 mol/kg at 10^6 Pa. On the other hand, our results for the equimolar binary mixtures (Figure 3, top) show molecular loading ranging from 2 (ZIF-4) to 6 (ZIF-6) mol/kg. Similar variations are also found for the other structures. This is due to the lower concentration in the bulk of ethane and ethylene which effectively reduces the larger adsorption loading at 10^6 Pa (Figure 4 and Figure A10 from Appendix 2). The adsorption is now like the obtained at 10^4 or 10^5 Pa for the binary mixtures. The loading of is remarkably lower for nitrogen than for the hydrocarbons, except for ZIF-10, -71, and -80, where the adsorption of nitrogen is similar to the adsorption of ethylene (Figure A10 from Appendix 2). In these three structures, ethylene and nitrogen compete for the same adsorption sites in analogous concentration. This is evidenced in Figure 5 that compares the distribution profiles of ethylene and nitrogen in ZIF-10.

We study the adsorption selectivity to compare the affinity towards ethane of each structure. To calculate the adsorption selectivity, we use adsorption loading data of the adsorbates, following this expression:

$$S_{i/j} = \frac{\theta_i}{\theta_j} \cdot \frac{X_j}{X_i}$$

where θ_i and θ_j are the adsorption loadings of molecules i and j; And X_i, X_j are the molar fractions.

The adsorption selectivity results from

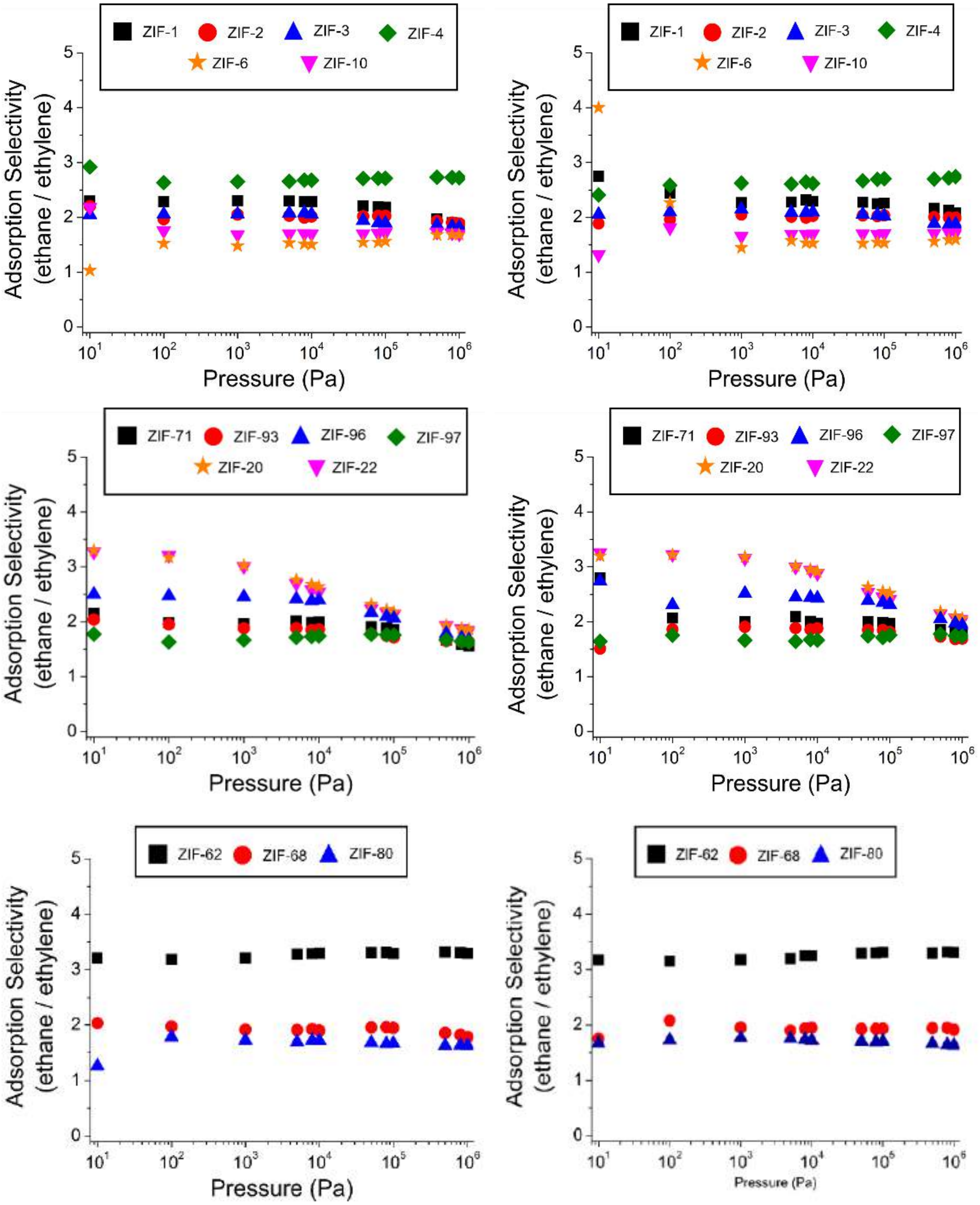

Figure 6. Adsorption selectivity of ethane over ethylene from the binary 50:50 (left) and the ternary 10:10:80 (right) mixtures at 298 K. Error bars are within the symbol size.

the binary and ternary mixtures in all the structures are shown in Figure 6 and Figure A11 from Appendix 2. Figure 6 shows the adsorption selectivity of ethane over ethylene in the 50:50 binary and the ternary mixtures. The values obtained for all the structures are quite similar, and we only observe some differences at 10^5 Pa and lower values of pressure. For instance, in ZIF-20 and -22 the adsorption selectivity towards ethane in the equimolar binary mixture decreases when the value of pressure goes from 10^3 Pa to 10^4 Pa. In the case of the ternary mixture, this reduction is observed at pressures above 10^4 Pa. The adsorption selectivity obtained for 50:50 (Figure 6) and 60:40 (Figure A11 from Appendix 2) ethane/ethylene binary mixtures is similar for all the structures under study.

Although nitrogen can be used experimentally to mimic industrial separation conditions of ethane and ethylene, other gasses such as methane, hydrogen, oxygen, carbon monoxide, and carbon dioxide can also be found during the separation process. Therefore, we performed additional simulations to study the effect of these gases on the ethane/ethylene adsorption selectivity. Simulations were carried out at 298 K and 10^6 Pa using a seven-component mixture of ethane (2.9%), ethylene (4.2%), methane (76.9%), hydrogen (2.1%), oxygen (3.7%), carbon monoxide (0.5%), and carbon dioxide (9.7%) in the 15 ZIFs. These amounts are related to the estimated composition of the Oxidative Coupling of Methane (OCM) effluent. The OCM method is used in the industrial production of ethylene.[45] Figure A12 in Appendix 2 contains the adsorption isotherms of ethane and ethylene in the seven-component mixture at 298K.

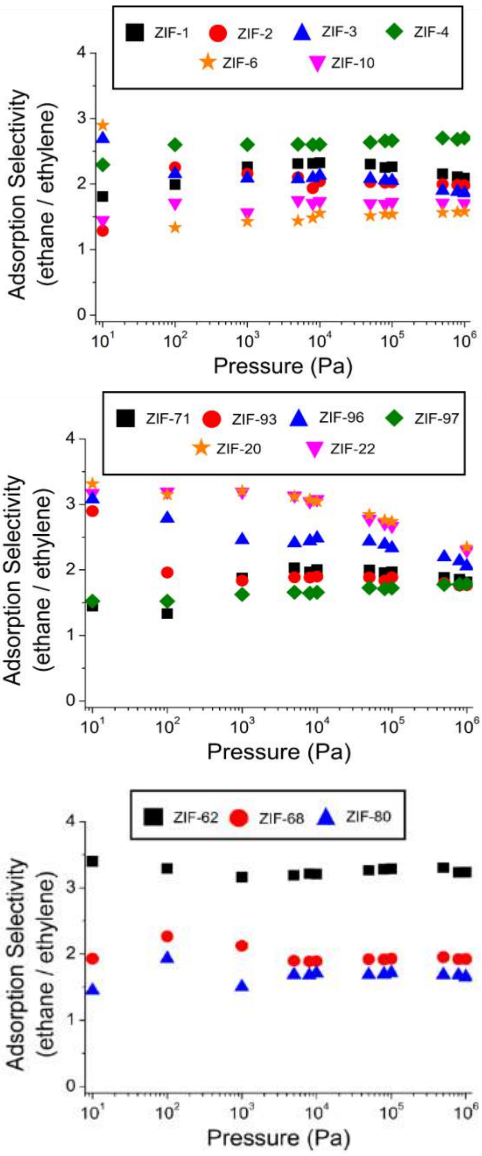

Figure 7. Adsorption selectivity of ethane over ethylene from the seven-component mixture at 298 K. Error bars are within the symbol size.

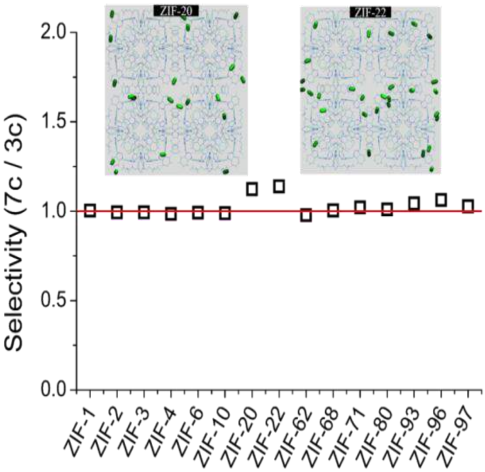

Figure 8. Increment of the adsorption selectivity of ethane over ethylene from the seven-component mixture compared to the ternary mixture in ZIF-1, -2, -3, -4, -6, -10, -20, -22, -62, -68, -71, -80, -93, -96, and -97 at 298 K and 106 Pa. The red line indicates no increment. It is also depicted the location of nitrogen molecules (green) in ZIF-20 and -22 in the ternary mixture at 10^6 Pa. Error bars are within the symbol size.

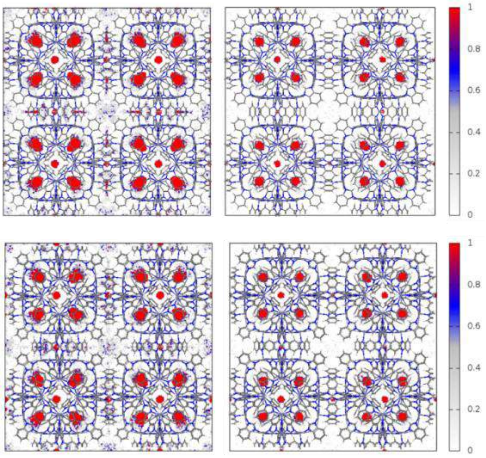

Figure 9. Distribution profile of ethane molecules in ZIF-20 (top) and ZIF-22 (bottom) from the 50:50 ethane / ethylene (left) and 7 component mixtures (right) at 10^4 Pa and 298 K.

Adsorption selectivity of ethane over ethylene from this mixture is depicted in Figure 7. All structures show preferential adsorption of ethane over ethylene. The highest adsorption selectivity is found for ZIF-4 and -62 (*cag* topology), followed by ZIF-20 and -22, (*lta* topology). Figure 8 compares the adsorption selectivity obtained from the mixtures with three and seven components. It also illustrates the location of nitrogen molecules inside the framework. In general, variations are negligible. ZIF-20 and -22 exhibit a slightly higher selectivity with the seven-component mixture. This is analogous to the higher selectivity found for the ternary mixture when compared to the binary mixture. ZIF-20 and -22 are formed by large cages, with relatively small linkers. The available surface for the adsorbates in these ZIFs is amongst the largest in this study, at about 1800 m^2/g (Table A4 from Appendix 2). For these two structures, the higher the loading of ethane and ethylene, the lower the adsorption selectivity. Therefore, there is competitive advantage for ethane at low concentrations. This is the reason why the adsorption selectivity resulting from binary mixtures drops from 3 to 2 at pressure values above 10^3 Pa. For ternary mixtures, this decrease appears at higher values of pressure (above 10^4 Pa), and the same is observed for the seven component mixtures above 10^5 Pa. The lower concentration in the bulk, combined with the presence of other gases, forces the hydrocarbons to adsorb in the main cavities, where the selectivity of ethane over ethylene is favoured. Figure 9 depicts the adsorption location of the ethane molecules in ZIF-20 and -22 for the equimolar binary mixture and the seven-component mixture. It can be noted how, even at relatively low loadings (seven-component mixtures) the ethane molecules tend to occupy the same spots inside the structures.

For a better knowledge of the dynamic behaviour of the adsorbates inside the structures, we calculated the self-diffusion coefficient of the gases from the binary (50:50 and 60:40), ternary, and the seven component mixtures at 298 K and 10^6 Pa (Tables A6-A8 from Appendix 2). The diffusion of the molecules at the simulation conditions is low in ZIF-1, -4, and -62. In these ZIFs, the cavities are interconnected by narrow channels which act as bottleneck for the molecular diffusivity, as depicted in Figure 10. The diffusion coefficient obtained for ethylene is equal or higher than that obtained for ethane in all structures and for all mixtures studied (within the error bars). This is the expected trend based on the higher adsorption of ethane. Differences in diffusion between ethane and ethylene are not larger than one order of magnitude in any case.

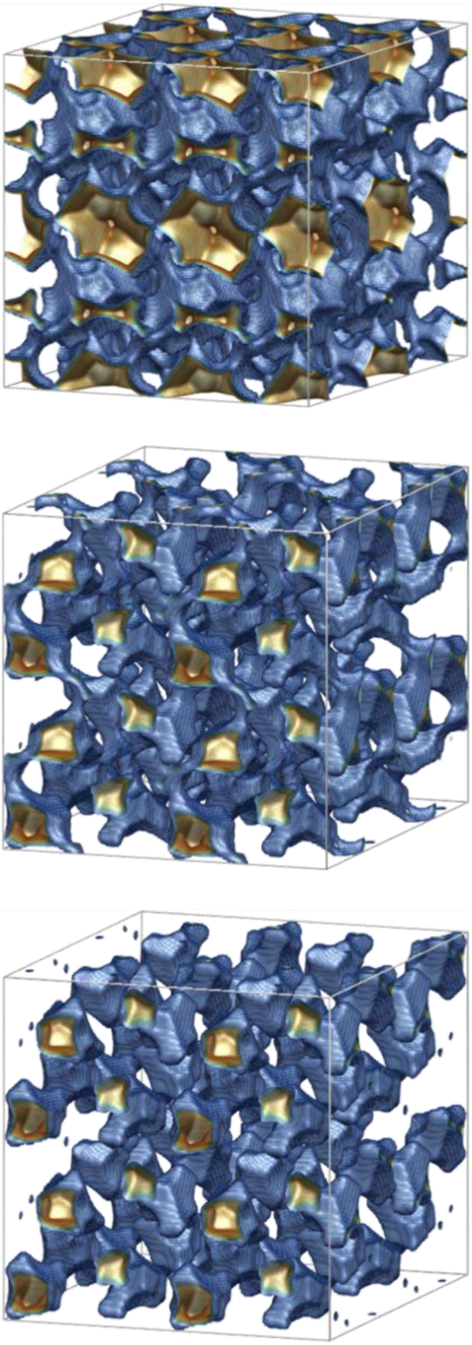

Figure 10. 3D surface of ZIF-1 (top), -4 (middle), and -62 (bottom) constructed with a methane atom probe.

We calculate the permselectivity of ethane over ethylene using the adsorption loading data and the diffusion coefficients, following this equation:

$$Permselectivity_{i/j} = \frac{\theta_i}{\theta_j} \cdot \frac{X_j}{X_i} \cdot \frac{D_i}{D_j}$$

where θ_i and θ_j are the adsorption loadings of molecules i and j; X_i, X_j are

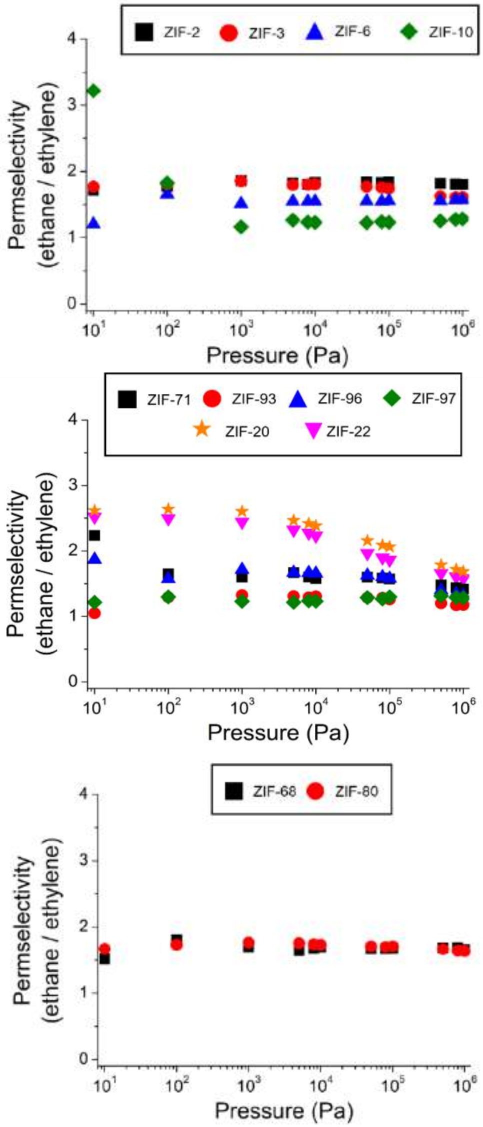

Figure 11. Permselectivity of ethane over ethylene from the 10:10:80 ternary mixture in ZIF-2, -3, -6, -10, -20, -22, -68, -71, -80, -93, -96, and -97 at 298 K. Error bars are within the symbol size.

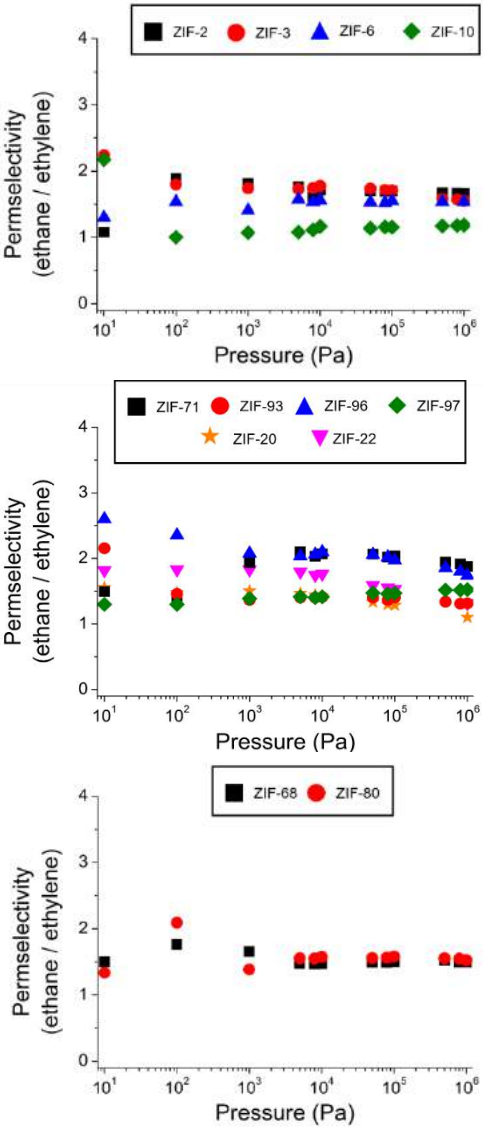

Figure 12. Permselectivity of ethane over ethylene from the seven-component mixture in ZIF-2, -3, -6, -10, -20, -22, -68, -71, -80, -93, -96, and -97 at 298 K. Error bars are within the symbol size.

the molar fractions; and D_i, D_j are the diffusion coefficients.

Figures 11, 12 and Figures A13, A14 from Appendix 2 show the permselectivity of ethane over ethylene for all mixtures and structures. ZIF-1, -4, and -62 were excluded since the adsorbates are unable to diffuse within their pores. These structures contain similarly sized windows connecting the main cavities, of 3.5 Å in diameter. Given the size of the molecules, and the rigidity of our frameworks, they are unable to diffuse through these windows. Permselectivity is similar for the 50:50 and the 60:40 binary mixtures. (Figures A13, A14 from Appendix 2). However, ZIF-2 (*crb*), -20 (*lta*), -22 (*lta*), -68 (*gme*), and -80 (*gme*) exhibit higher permselectivity for the ternary mixture (Figure 11). In contrast, for ZIF-10 (*mer*), -93 (*rho*), -96 (*rho*), and -97 (*rho*) permselectivity is lower for the ternary mixture. This decrease of permselectivity is especially noticeable on ZIF-10, which suggests a negative effect of the *mer* topology on the diffusion of ethane. In the case of ZIF-93, -96, and -97, the combination of large pores and rho topology impede the diffusion of ethane.

Permselectivity towards ethane is lower for the seven-component mixture in all the structures, except for ZIF-71, -93, -96, and -97, with *rho* topology (Figure 12). As already discussed, these four structures show either no difference (ZIF-71) or lower (ZIF-93, -96, -97) permselectivity for the ternary mixtures compared to the binary mixture. Permselectivities taken from the seven-component and the ternary mixture are compared in Figure 13.

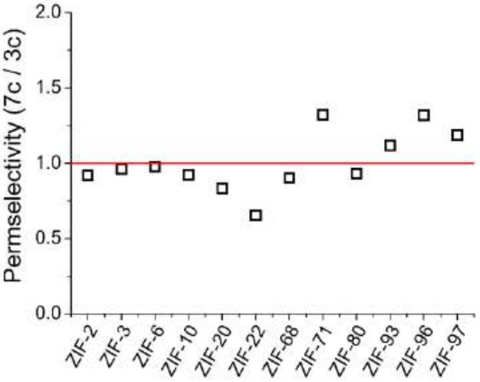

Figure 13. Increment of the permselectivity of ethane over ethylene from the seven-component mixture compared to the permselectivity in the ternary mixture in ZIF-2, -3, -6, -10, -20, -22, -68, -71, -80, -93, -96, and -97 at 298 K and 106 Pa. The red line indicates no increment. Error bars are within the symbol size.

The self-diffusion coefficients are listed in Tables A6 to A8 from Appendix 2 and can be used to interpret gas separation in ZIF-71, -93, -96, -97. For the binary 50:50 mixture, the diffusion coefficients for ethylene are higher than for ethane, with differences ranging from 16% to 22%. For the ternary mixture differences in diffusion go from 25% to 47%. Though adsorption selectivity taken from the isotherms of the ternary mixture is higher than for the binary mixture, the largest difference in diffusion, result in a net decrease of the permselectivity for the former scenario. In the seven-component mixture, differences in diffusion of ethane and ethylene range from 17% to 34%.

Conclusions

We show that enriched ethylene mixtures can be obtained using ZIFs with high affinity for ethane. The application of these molecular sieves in the industrial production of ethylene could reduce the amount of energy employed to achieve the separation of ethane and ethylene. Simulations support previous findings for zeolites and show that the presence of nitrogen also affects the selective behaviour of ethane and ethylene in several ZIFs. Seven out of the fifteen structures analysed here showed enhanced adsorption selectivity: ZIF-1, -20, -22, -93, -96, and -97. However, the values obtained for permselectivity reduce the list of potentially useful structures to ZIF-2, (with *crg* topology), ZIF-20, and -22 (with *lta* topology).

The introduction of a seven-component mixture to the study provides further details on the understanding of the separation process of existent mixtures. We found an increase of permselectivity for ZIF-71, -93, -96, and -97 (*rho* topology). This suggests that a realistic approach to the separation of ethane and ethylene could be performed using these structures. Further studies including other structures with rho topology, as well as structures with *crg* and *lta* topology could follow, as derived from this study. These findings are potentially applicable to enhance the separation step in ethylene production.

Bibliography

(1) True, W. R. *Oil Gas J.* **2012**, *110*.

(2) Xie, T.; McAuley, K. B.; Hsu, J. C. C.; Bacon, D. W. *Industrial & Engineering Chemistry Research* **1994**, *33*, 449.

(3) Kim, J.; Chang, C.; Tucker, M. L. *Frontiers in Plant Science* **2015**, *6*, 20.

(4) Wills, R. B. H.; Golding, J. B. *Journal of the Science of Food and Agriculture* **2015**, *95*, 1379.

(5) H. J. Salgado-Gordon, G. V.-M. *CFT Cienc. Tecnol. Futuro* **2011**, *4*, 15.

(6) Berlier, K.; Olivier, M.-G.; Jadot, R. *Journal of Chemical & Engineering Data* **1995**, *40*, 1206.

(7) Kim, J.; Lin, L.-C.; Martin, R. L.; Swisher, J. A.; Haranczyk, M.; Smit, B. *Langmuir* **2012**, *28*, 11914.

(8) Banerjee, D.; Liu, J.; Thallapally, P. K. *Comments on Inorganic Chemistry* **2015**, *35*, 18.

(9) Yang, S.; Ramirez-Cuesta, A. J.; Newby, R.; Garcia-Sakai, V.; Manuel, P.; Callear, S. K.; Campbell, S. I.; Tang, C. C.; Schröder, M. *Nature Chemistry* **2014**, *7*, 121.

(10) Maghsoudi, H. *Adsorption* **2016**, *22*, 985.

(11) Pires, J.; Fernandes, J.; Fernandes, A. C.; Pinto, M. *Separation Science and Technology* **2017**, *52*, 51.

(12) Ploegmakers, J.; Japip, S.; Nijmeijer, K. *Journal of Membrane Science* **2013**, *428*, 445.

(13) Ploegmakers, J.; Japip, S.; Nijmeijer, K. *Journal of Membrane Science* **2013**, *428*, 331.

(14) Bao, Z.; Alnemrat, S.; Yu, L.; Vasiliev, I.; Ren, Q.; Lu, X.; Deng, S. *Langmuir* **2011**, *27*, 13554.

(15) Zhang, Y.; Li, B.; Krishna, R.; Wu, Z.; Ma, D.; Shi, Z.; Pham, T.; Forrest, K.; Space, B.; Ma, S. *Chemical Communications* **2015**, *51*, 2714.

(16) Pillai, R. S.; Pinto, M. L.; Pires, J.; Jorge, M.; Gomes, J. R. B. *ACS Applied Materials & Interfaces* **2015**, *7*, 624.

(17) Martins, V. F. D.; Ribeiro, A. M.; Ferreira, A.; Lee, U. H.; Hwang, Y. K.; Chang, J.-S.; Loureiro, J. M.; Rodrigues, A. E. *Separation and Purification Technology* **2015**, *149*, 445.

(18) Bux, H.; Chmelik, C.; Krishna, R.; Caro, J. *Journal of Membrane Science* **2011**, *369*, 284.

(19) Lahoz-Martin, F. D.; Calero, S.; Gutierrez-Sevillano, J. J.; Martin-Calvo, A. *Microporous and Mesoporous Materials* **2017**, *248*, 40.

(20) Aguado, S.; Bergeret, G.; Daniel, C.; Farrusseng, D. *Journal of the American Chemical Society* **2012**, *134*, 14635.

(21) Park, K. S.; Ni, Z.; Côté, A. P.; Choi, J. Y.; Huang, R.; Uribe-Romo, F. J.; Chae, H. K.; O'Keeffe, M.; Yaghi, O. M. *Proceedings of the National Academy of Sciences* **2006**, *103*, 10186.

(22) Hu, Y.; Liu, Z.; Xu, J.; Huang, Y.; Song, Y. *Journal of the American Chemical Society* **2013**, *135*, 9287.

(23) Karagiaridi, O.; Lalonde, M. B.; Bury, W.; Sarjeant, A. A.; Farha, O. K.; Hupp, J. T. *Journal of the American Chemical Society* **2012**, *134*, 18790.

(24) Tran, U. P. N.; Le, K. K. A.; Phan, N. T. S. *ACS Catalysis* **2011**, *1*, 120.

(25) Lu, G.; Hupp, J. T. *Journal of the American Chemical Society* **2010**, *132*, 7832.

(26) Bennett, T. D.; Goodwin, A. L.; Dove, M. T.; Keen, D. A.; Tucker, M. G.; Barney, E. R.; Soper, A. K.; Bithell, E. G.; Tan, J.-C.; Cheetham, A. K. *Physical Review Letters* **2010**, *104*, 115503.

(27) Dubbeldam, D.; Calero, S.; Vlugt, T. J. H.; Krishna, R.; Maesen, T. L. M.; Beerdsen, E.; Smit, B. *Physical Review Letters* **2004**, *93*, 088302.

(28) Liu, B.; Smit, B.; Rey, F.; Valencia, S.; Calero, S. *The Journal of Physical Chemistry C* **2008**, *112*, 2492.

(29) Böhme, U.; Barth, B.; Paula, C.; Kuhnt, A.; Schwieger, W.; Mundstock, A.; Caro, J.; Hartmann, M. *Langmuir* **2013**, *29*, 8592.

(30) Chmelik, C.; Freude, D.; Bux, H.; Haase, J. *Microporous and Mesoporous Materials* **2012**, *147*, 135.

(31) Chokbunpiam, T.; Chanajaree, R.; Saengsawang, O.; Reimann, S.; Chmelik, C.; Fritzsche, S.; Caro, J.; Remsungnen, T.; Hannongbua, S. *Microporous and Mesoporous Materials* **2013**, *174*, 126.

(32) Martin-Calvo, A.; Garcia-Perez, E.; Garcia-Sanchez, A.; Bueno-Perez, R.; Hamad, S.; Calero, S. *Physical*

Chemistry Chemical Physics **2011**, *13*, 11165.

(33) Deeg, K. S.; Gutiérrez-Sevillano, J. J.; Bueno-Pérez, R.; Parra, J. B.; Ania, C. O.; Doblaré, M.; Calero, S. *The Journal of Physical Chemistry C* **2013**, *117*, 14374.

(34) Calero, S.; Martin-Calvo, A.; Hamad, S.; Garcia-Perez, E. *Chemical Communications* **2011**, *47*, 508.

(35) Dubbeldam, D.; Calero, S.; Vlugt, T. J. H.; Krishna, R.; Maesen, T. L. M.; Smit, B. *The Journal of Physical Chemistry B* **2004**, *108*, 12301.

(36) Martín-Calvo, A.; Lahoz-Martín, F. D.; Calero, S. *The Journal of Physical Chemistry C* **2012**, *116*, 6655.

(37) García-Sánchez, A.; Ania, C. O.; Parra, J. B.; Dubbeldam, D.; Vlugt, T. J. H.; Krishna, R.; Calero, S. *The Journal of Physical Chemistry C* **2009**, *113*, 8814.

(38) Gutierrez Sevillano, J. J.; Calero, S.; Ania, C. O.; Parra, J. B.; Kapteijn, F.; Gascon, J.; Hamad, S. *Journal of Physical Chemistry C* **2013**, *117*, 466.

(39) Banerjee, R.; Phan, A.; Wang, B.; Knobler, C.; Furukawa, H.; O'Keeffe, M.; Yaghi, O. M. *Science* **2008**, *319*, 939.

(40) Frenkel, D.; Smit, B. *Understanding Molecular Simulation: From Algorithms to Applications*; 2nd ed.; Academic Press, 2001.

(41) Heinbuch, U.; Fischer, J. *Molecular Simulation* **1987**, *1*, 109.

(42) Nosé, S. *The Journal of Chemical Physics* **1984**, *81*, 511.

(43) Hoover, W. G. *Physical Review A* **1985**, *31*, 1695.

(44) Dubbeldam, D.; Calero, S.; Ellis, D. E.; Snurr, R. Q. *Molecular Simulation* **2016**, *42*, 81.

(45) Amoco-Corporation US5015799A, **1991**.

Selective Separation of BTEX Mixtures Using Metal-Organic Frameworks

4

Francisco D. Lahoz-Martín, Ana Martín-Calvo and Sofía Calero

We use molecular simulation to study the selective adsorption of BTEX mixtures (benzene, toluene, ethylbenzene, xylenes) in metal-organic frameworks. The adsorption of these compounds is a basic step in reutilizing petrochemical industry derivatives. BTEX mixture components are precursors to polymers such as polyethylene terephthalate. It is also important to store these molecules due to their high toxicity to humans. We study the storage, adsorption selectivity, distribution, and overall behaviour of the adsorbed molecules inside the structures. We use MOF-1, MIL-47, and IRMOF-1 to test the effect of the size of the cavities and the topology of the structure in the adsorption of the components of the mixture. We found that these structures are useful to separate ethylbenzene and *o*-xylene from the BTEX mixtures.

1. Introduction

Benzene, toluene, ethylbenzene, and the isomers of xylene (*o*-, *m*-, and *p*-xylene) form a group of aromatic compounds widely known as BTEX. The importance of these components in petrochemical industry can be pointed out from their uses that span from production of resistant plastics as polystyrene (ethylbenzene) and polyethylene terephthalate (xylenes) to nylon (benzene and toluene).[1,2] The components of the BTEX mixtures are highly toxic.[3,4] Toxicity tests have been run in vulnerable places, such as fuel stations. The presence of these compounds in air has been proved harmful for humans and other living beings.[5-7] Studies carried out showed a link between the presence of BTEX compounds and the increment of cancer and toxic-related illnesses. On field measurements, Liu *et al.*,[7] estimated the amount of BTEX molecules in air at ground level near a fuel station. The results obtained by gas chromatography revealed the contents of BTEX in a cubic meter of air: 0.66 ng/m^3 of benzene, 2.03 ng/m^3 of toluene, 5.91 ng/m^3 of ethylbenzene, 5.45 ng/m^3 of ortho-xylene, and 6.49 ng/m^3 of meta- and para-xylene. The environmental effect of BTEX mixtures has promoted the need of searching for techniques to efficiently separate their components.[8-10]

Currently, most industrial processes involving BTEX components undergo separation through molecular sieves. These structures are an alternative to less selective and more aggressive separation and production methods such as on-site carbon regeneration or gas stripping.[11,12] We focus on Metal Organic Frameworks (MOFs) as structures to adsorb and separate mixtures.[13,14] MOFs are nanoporous materials, formed by metallic centres connected by organic linkers, which create unique networks of cages and windows of different geometries and sizes. Some MOFs are characterized by large pore size and high selectivity due to the possibility of varying the synthesis building blocks and relative physical and chemical stability.[15-17] Depending on the organic linker, its orientation, and the metallic centre, the MOFs obtained would have distinctive properties. MOFs can be modified in many ways to enhance or to diminish the adsorption of different molecules. This flexibility makes MOFs promising structures for the separation of gases. We use molecular simulation to study the selective adsorption of BTEX mixtures in three MOFs. The selectivity for each molecule varies depending on the MOF and on the component to separate. The structures used are IRMOF-1,[17] MIL-47,[16] and MOF-1.[15] IRMOF-1 is one of the most studied MOFs. It is the smallest isoreticular metal-organic framework, a family of MOFs widely used in separation processes.[13,17] It contains zinc as coordinated metal, and 1,4-benzenedicarboxylate (BDC) as organic linker. IRMOF-1 is the largest structure used in this study.[17] The other two structures, MIL-47 and MOF-1, have been previously applied to the adsorption separation of isomers of xylene and ethylbenzene.[18,19] MIL-47 belongs to the MIL series (Material of Institut Lavoisier), and was first synthesized by Barthelet *et al.*[20] It contains vanadium as coordinated metallic centre, and BDC as organic linker. This structure is characterized by diamond shaped straight channels in one direction.[20] MOF-1 is the smallest structure under study. It is characterized by the presence of zinc as coordinated metallic centre and BDC as organic ligand. Along with the organic linkers, half of the metallic centres of the structure are linked via 1,4-diazabicyclo [2, 2, 2] octane (Dabco) groups.[15,21]

We use molecular simulations to evaluate the applicability of MOFs to the selective separation of BTEX compounds. In section 2 we describe the models and methods used. Results and discussion can be found in section 3, and the main conclusions are summarized in section 4.

2. Simulation methods and models

MOF-1, MIL-47, and IRMOF-1 have been selected in order to study the effect of the void space available, the orientation of the organic linker, and the type of metallic centre in the adsorption of BTEX compounds.[22,23]

We use rigid models of the structures MOF-1, MIL-47, and IRMOF-1. Flexibility in Metal-Organic Frameworks remains a formidable challenge from the simulation point of view. A very efficient force field that predicts negative thermal expansion in IRMOF-1 can be found in the literature,[24] but to the best of our knowledge flexible force fields for MOF-1 and MIL-47 have not been developed yet. In structures that do not exhibit large structural changes (e.g. breathing or gate-opening effects), framework flexibility usually has minor effects on static properties,[25] and results of dynamic properties when flexibility is included depend very much on the model used.[26] There is not experimental evidence of large structural changes of IRMOF-1, MIL-47, and MOF-1 at the temperature and range of pressure under study. This fact combined with the lack of force fields lead us to consider the use of rigid models as a reasonable approximation.

MOF-1 contains a network of cavities of 7.5 Å connected by 4 Å windows.[21] We use a rigid model for the structure based on the crystallographic position of the atoms reported by Dybtsev *et al.*[15] Computed helium void fraction, surface area, and pore volume of MOF-1 are 0.639, 2342.450 m^2/g, and 0.773 m^3/kg respectively. For MOF-1, we use a simulation box of 3 x 3 x 3. MIL-47 is formed by diamond shaped channels with 10.5 x 11.0 Å of side.[20] We use a rigid model with the crystal structure from Alaerts *et al.*[16] Computed helium void fraction, surface area, and pore volume of this structure are 0.620, 1837.770 m^2/g, and 0.620 m^3/kg, respectively. For MIL-47, we use a simulation box of 4 x 2 x 2. The linkers of BDC of IRMOF-1 are alternatively oriented towards the centre of the structure cages, creating two types of cavities: Large cavities, with 15 Å in diameter, and slightly smaller cages, with 11 Å in diameter. The model for this structure is rigid and based on the structure reported by Eddaoudi *et al.*[17] Computed helium void fraction, surface area, and pore volume of this structure are 0.815, 3821.540 m^2/g, and 1.373 m^3/kg, respectively. For IRMOF-1, we use a simulation box of 1 x 1 x 1.

The Lennard-Jones parameters of MOF-1, IRMOF-1, and MIL-47 are taken from DREIDING generic force field[27] except those of the metallic centres, which are taken from UFF.[28] Partial charges of the atoms in the structures are taken from Bueno-Perez *et al.*[29] for MIL-47, Dubbeldam *et al.*[30] for MOF-1, and Frost *et al.*[31] and Dubbeldam *et al.*[32] for IRMOF-1.

The models for benzene, toluene, ethylbenzene, and the three isomers of xylene (ortho-, meta-, and para-xylene) are taken from Castillo *et al.*,[33] Rai *et al.*,[34] Jorgensen *et al.*,[35] and Caleman *et al.*[36] These are full atom models for the benzene rings and united atom models for the methyl and ethyl groups, where each CH_x group acts as one single interaction centre.

The Lennard-Jones parameters of the interactions between the adsorbates and between the adsorbate and the structure have been calculated using Lorentz-Berthelot mixing rules.[30] We use the Ewald summation method for the Coulombic interactions with a relative precision of 10^{-6}. The Lennard-Jones potential is cut and shifted at a *cut-off* distance of 12 Å. Lennard-Jones parameters and partial charges for the models of the structures and the adsorbates, as well as the labels of the atoms of the structures, can be found in Figure A1 and Tables A1 and A2 in Appendix 3. We use Monte Carlo simulations in the grand canonical ensemble for adsorption analysis. The molecules inside the system are susceptible to be exchanged with particles from a reservoir with the same chemical potential. For real gases, the chemical potential is related to the fugacity, and fugacity relates to pressure through the fugacity coefficient (Φ). For the gases under study at room temperature and pressure under 100 kPa, we adopt fugacity as pressure. From the computed adsorption isotherms we obtain adsorption selectivities and average occupation profiles. To compare with experimental data, the absolute adsorption obtained by simulations has to be converted to excess adsorption following the equation:[37]

$$adsorption_{exc} = adsorption_{abs} - \frac{PV}{zRT}$$

where P, V, and T are the pressure, volume and temperature of the system, , R is the gas constant, and z is the gas compressibility.

We compute Henry coefficients (K_H) and heats of adsorption (Qst) for the BTEX molecules in each MOF. Simulations were performed using Monte Carlo (MC) in the canonical ensemble fixing temperature, volume, and number of particles. These simulations were carried out at zero coverage, using the Widom test particle method.[38] MC simulations in the grand canonical ensemble were carried out to compute the adsorption isotherms, radial distribution functions (RDFs), and average occupation profiles. Self-diffusion coefficients of the adsorbates are also calculated for each structure. We use Molecular Dynamic (MD) simulations in the canonical ensemble (NVT) integrating Newton's law of motion by the Vertlet's algorithm. These simulations required $3x10^7$ cycles, with time step of $5 \cdot 10^{-4}$ ps. We use the thermostat of Nosé-Hoover to keep the temperature fixed.[38] The Mean Square Displacement (MSD) is measured over time to obtain self-diffusivity of BTEX compounds. Calculations were carried out with the in-house RASPA code.[39]

3. Results

To obtain the adsorption isotherms of the BTEX components and mixtures in MOF-1, MIL-47, and IRMOF-1 we carried out molecular simulations at 423 K and 448 K for a range of pressures spanning from 10^2 to 10^5 Pa. Our results for single component adsorption are compared to previous experimental data[18,19] predicting the adsorption trend in MOF-1 and MIL-47 (Appendix 3, Figure A2). Simulation data overestimate adsorption in MOF-1 and underestimate it in MIL-47. The differences observed for MOF-1 can be attributed to the fact that simulations use idealized crystalline models, whose pore volumes are larger than the experimental structures.[40] Differences in MIL-47 were already observed by Castillo *et al.*[33] and are attributed to small variations in the framework as a function of temperature. The use of generic force fields is another factor that could lead to discrepancies between experiment and simulation. They have the advantage of being easy to implement but tend to over- or under predict experimental adsorption.[38] To our knowledge, experimental data for IRMOF-1 are not available in literature.

Figure 1 shows the computed Henry coefficients and isosteric heats of adsorption for all molecules in the three

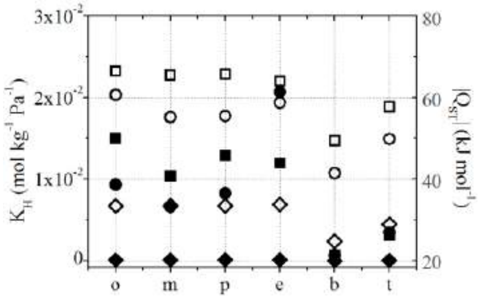

Figure 1. Computed Henry coefficients (full symbols) and isosteric heats of adsorption (empty symbols) of ortho-xylene (o), meta-xylene (m), para-xylene (p), ethylbenzene (e), benzene (b), and toluene (t) in MOF-1 (squares), MIL-47 (circles), and IRMOF-1 (diamonds) at 448 K. Error bars are within the symbol size.

structures. These properties allow estimating the strength of the interaction between the adsorbates and the structures. IRMOF-1 exhibits the lowest values of Henry coefficients and heats of adsorption. This indicates weak interactions between the molecules and the structure. The interactions of the molecules with MIL-47 and MOF-1 are stronger than these for IRMOF-1 due to both size and shape of the cavities of these MOFs. Adsorbates inside small cavities interact strongly with the atoms of the structure. These interactions are similar in MOF-1 and MIL-47, since the small size of the cages of MOF-1 is comparable to the narrow corners of the channels of MIL-47. The effect of the corners of the channels of MIL-47 is especially remarkable for ethylbenzene. The presence of a longer radical (ethyl group), and the fact that ethylbenzene is slightly less symmetric than the rest of BTEX compounds could favour the adsorption of the molecule closer to the corners of the channels of MIL-47. Likewise, the fact that MIL-47 has channels instead of cavities (as MOF-1) can affect the distribution of ethylbenzene, improving its adsorption strength. This behaviour of ethylbenzene is clearly noticeable in Figure 1. For the rest of the adsorbates, MOF-1 shows the highest values of isosteric heats of adsorption and henry coefficients. This trend is not followed by ethylbenzene, since higher values are found for the interaction between MIL-47 and ethylbenzene than for that of ethylbenzene and MOF-1. Benzene does not interact strongly with any of the structures, exhibiting relatively low values of heats of adsorption, especially for IRMOF-1. Energies, enthalpies, and entropies of adsorption, as well as Henry coefficients for the BTEX molecules in each MOF under study can be found in Appendix 3 (Table A3). It is also interesting to highlight the different trend observed between the isosteric heats of adsorption and the computed Henry coefficients in MIL-47 (Figure 1). For a better understanding of this behaviour we compute these properties a function of temperature, for a range that spans from 100 to 700 K (Figures A3 and A4 on Appendix 3). Though differences in heats of adsorption are clearly noticeable for all molecules in the whole range of temperature, this is not true for Henry coefficients that tend to converge at the highest temperatures. The diamond shape of MIL-47 channel makes of the corners a clear preferential adsorption site at low temperatures. However, this preferential site disappears at high temperature since the higher kinetic energy of the molecules increases their mobility all around the pore.

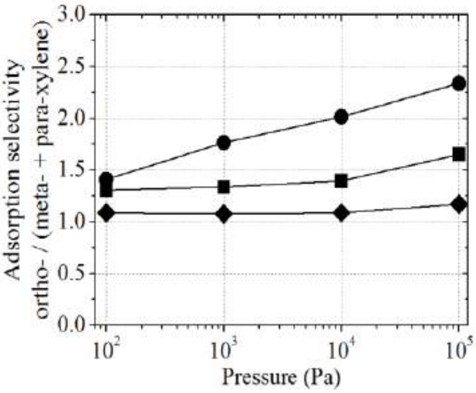

Figure 2. Adsorption selectivity of ortho- / (meta- + para-xylene) obtained from the adsorption isotherms of the equimolar ternary mixture in MOF-1 (squares), MIL-47 (circles), and IRMOF-1 (diamonds) at 448 K.

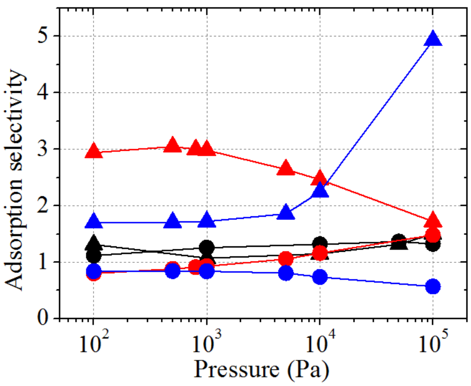

Figure 3. Adsorption selectivity of ortho- / (meta- + para-xylene + ethylbenzene) (circles) and ethylbenzene / (ortho- + meta- + para-xylene) (triangles), from the adsorption isotherms of the quaternary equimolar mixture in MOF-1 (black), MIL-47 (red), and IRMOF-1 (blue) at 448 K.

Adsorption selectivities were obtained from the computed adsorption isotherms of mixtures of xylenes (Figures A5-A9 in Appendix 3) from the expression:

$$S_{\frac{i}{j}} = \frac{\theta_i}{\theta_j} \cdot \frac{X_j}{X_i}$$

where θ_i and θ_j are the values of adsorption of the molecules i and j and X_i, X_j are the molar fractions of components i and j in the mixture.

The selectivities obtained from the equimolar ternary mixture of xylene isomers are shown in Figure 2. Ortho-xylene is the molecule that adsorbs preferentially in the structures. The largest values of selectivity were obtained in MIL-47 and MOF-1. IRMOF-1 does not exhibit high selectivity for ortho-xylene since its cavities are larger than the cavities of MOF-1 and MIL-47. Therefore, the competition between molecules is small for the range of pressures under study.

The adsorption selectivities obtained from the computed adsorption isotherms of the quaternary equimolar mixture (ortho- / meta- / para-xylene / ethylbenzene) are shown in Figure 3. The isotherms are also collected in Appendix 3 (Figure A10). Experimental data for similar mixtures were carried out by Finsy *et al.*[19] They study the adsorption behaviour of ortho-xylene, meta-xylene, para-xylene, ethylbenzene, and n-octane in MIL-47 at different temperatures. Despite the differences between our simulation conditions and those of Finsy *et al.*, we find similar trends in the adsorption isotherms, being ethylbenzene in both cases the preferentially adsorbed molecule in MIL-47.

In MOF-1 ortho-xylene adsorbs better than the other components of the quaternary mixture, followed by ethylbenzene. At low values of pressure, the adsorption of all BTEX components is quite similar. When pressure rises ortho-xylene is preferentially adsorbed, with ethylbenzene being the second most adsorbed molecule. At the highest value of pressure studied (10^5 Pa), adsorption of ethylbenzene surpasses adsorption of ortho-xylene. At this pressure, the adsorption values obtained for meta- and para-xylene are similar. The adsorption selectivities for ortho-xylene and ethylbenzene are comparable, but larger for ethylbenzene at the lowest and highest values of pressure. In MIL-47, ethylbenzene and ortho-xylene are preferentially adsorbed. At low pressure, ethylbenzene is the most adsorbed molecule. As pressure increases, the other molecules of the mixture, especially ortho-xylene, enter the structure. At 10^5 Pa, the adsorption selectivities for both ethylbenzene and ortho-xylene are almost the same. The structure exhibits high selectivity for ethylbenzene for all values of pressures studied. The loading of BTEX compounds in IRMOF-1 is low at low and medium pressure. For pressures above 10^4 Pa, the adsorption of ethylbenzene largely increases, and selectivity is in favour of ethylbenzene through the whole range of pressure. This selectivity is enhanced when pressure increases, reaching the highest value at 10^5 Pa, where ethylbenzene is adsorbed five times more than the rest of the molecules.

The most interesting mixture to study involves all components of BTEX. Therefore, the adsorption isotherms and the selectivities from the six-component equimolar mixture (ortho- / meta- / para-xylene / ethylbenzene / benzene / toluene) have been computed. Adsorption selectivities are shown in Figure 4, and the computed adsorption isotherms can be found in Appendix 3 (Figure A7). As for the quaternary equimolar mixtures, ortho-xylene and ethylbenzene are preferentially adsorbed. However, the presence of toluene affects the adsorption of both ortho-xylene and ethylbenzene at high pressures. In MOF-1, ortho-xylene and ethylbenzene are the most adsorbed molecules, followed by para- and meta-xylene. The largest difference between loadings of ortho-xylene/ethylbenzene and the rest of the molecules is obtained at 10^5 Pa. At this pressure the adsorption values of meta- and para-xylene in MOF-1 are similar, and the

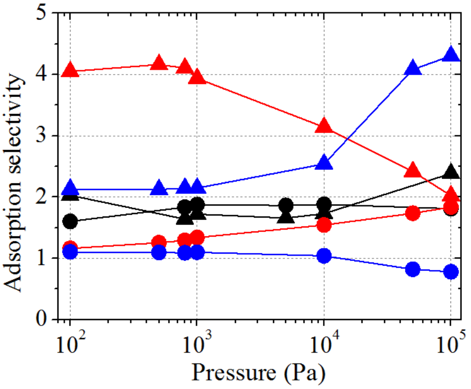

Figure 4. Adsorption selectivity of ortho- / (meta- + para-xylene + ethylbenzene + benzene + toluene) (circles) and ethylbenzene / (ortho- + meta- + para-xylene + benzene + toluene) (triangles) from the adsorption isotherms of the six-component equimolar mixture in MOF-1 (black), MIL-47 (red), and IRMOF-1 (blue) at 448 K.

adsorption of benzene is significantly lower.

The adsorption of the six-component mixture in MIL-47 shows large variation with pressure. At low values of pressure (up to 10^3 Pa) the adsorption hierarchy is ethylbenzene > ortho-xylene ≈ meta- ≈ para-xylene ≈ toluene > benzene (low adsorption). At higher values of pressure (10^3 - 10^5 Pa), the adsorption of ortho-xylene increases, reaching values similar to these obtained for ethylbenzene at 10^5 Pa. The adsorption isotherms of meta-, para-xylene, and toluene match one another for all pressure range. As for MOF-1, the adsorption of benzene in MIL-47 is low for all pressures under study.

The adsorption isotherms of the six component equimolar mixture in IRMOF-1 show ethylbenzene as the most adsorbed molecule for pressures above 10^4 Pa. The isomers of xylene and toluene have similar values of adsorption, with some preference for ortho-xylene at 10^5 Pa. The adsorption values obtained for benzene are lower than these obtained for the rest of the molecules. On the other hand, the adsorption obtained for this molecule at high pressure (above 10^4 Pa) is larger in IRMOF-1 than in MOF-1 or MIL-47. The adsorption obtained in IRMOF-1 up to 10^3 Pa is lower than this obtained in MOF-1 or in MIL-47. The large cavities of IRMOF-1 require high values of pressure to be filled. Once the pressure threshold is surpassed, loading in IRMOF-1 far exceed MOF-1 and MIL-47, since the former structure is able to allocate more molecules inside the pores. The adsorption selectivities obtained for the most adsorbed molecules (ortho-xylene and ethylbenzene) are shown in Figure 4. These values of selectivity point out the best range of pressure to separate ortho-xylene and/or ethylbenzene from the rest of the components of the mixture. It can be noted that MOF-1 separates both ortho-xylene and ethylbenzene from the other components of the mixture for the whole range of pressure. The selectivity of ortho-xylene and ethylbenzene in this structure is similar, with higher values for ethylbenzene at low and high pressure. Ethylbenzene and ortho-xylene (the later especially above 10^3 Pa) can be selectively separated from the rest of the components of the mixture using MIL-47. This structure adsorbs preferentially ethylbenzene. IRMOF-1 shows selectivity in favour of ethylbenzene for all pressures studied. The adsorption selectivity of ortho-xylene is lower in IRMOF-1 than in the other two MOFs, and it decreases severely at high pressure, as the adsorption of ethylbenzene increases.

Molecular simulation also provides information about the relative position of the molecules inside the structure. From these values, we are able to obtain occupation density profiles that allow the study of the preferential adsorption sites of each molecule, and provide a better understanding of the behaviour observed from the adsorption isotherms. These occupation density profiles are represented as projections on each spatial plane (*xy*, *yz*, and *xz*) of the centre of mass of the molecules inside the structure. The study of the distribution of BTEX molecules inside the different structures is based upon the results of the six-component equimolar mixture adsorption isotherms. Figures 5 to 7 show the average occupation profiles of the molecules from the adsorption of the six-component equimolar mixtures, and Figures A12 to A14 from Appendix 3, show the occupation profiles obtained from the pure component adsorption in each structure. The distribution of toluene and benzene is not shown in the average occupation profiles of the six-component adsorption isotherms, since the adsorption of these two molecules is almost negligible compared to the adsorption of the other components of the mixture. However, the average occupation profiles obtained from the pure component adsorption isotherms show the preferential adoption sites of these two molecules in the structures. This indicates that the differences in adsorption of toluene and benzene are due to competitive adsorption with the rest of the components of the mixtures.

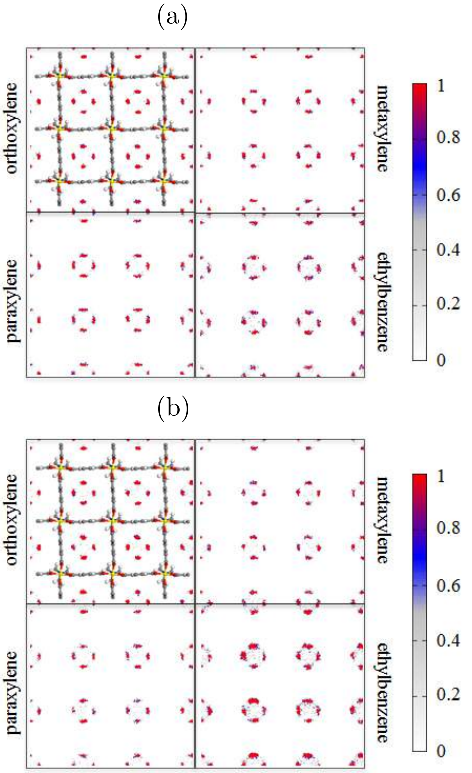

Figure 5. Average occupation profiles of ortho-, meta-, para-xylene, and ethylbenzene from the six-component mixture adsorbed in MOF-1, at 448 K and at (a) 1 kPa and (b) 100 kPa. The colour gradation is related to the occupation density. For an easier understanding of the location of the molecules, a representation of the structure has been added to one of the plots.

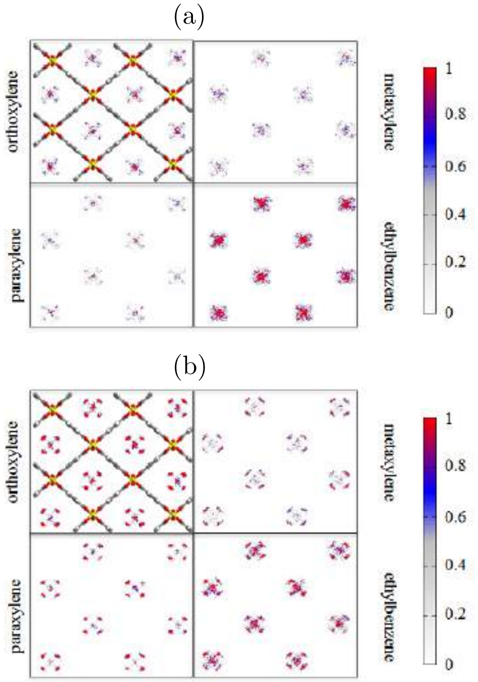

Figure 6. Average occupation profiles of ortho-, meta-, para-xylene, and ethylbenzene from the six-component mixture adsorbed in MIL-47, at 448 K and at (a) 1 kPa and (b) 100 kPa. The colour gradation is related to the occupation density. For an easier understanding of the location of the molecules, a representation of the structure has been added to one of the plots.

The average occupation profiles obtained for the six-component adsorption isotherms show that the isomers of xylene and ethylbenzene are adsorbed near the organic linkers of MOF-1 at 10^3 Pa (Figure 5). These adsorbates exhibit the same occupation density, as the adsorption of the molecules in MOF-1 at medium pressure is similar. The average occupation profile of the molecules at high pressure (10^5 Pa) is also shown in Figure 5. Ethylbenzene is the molecule that preferentially adsorbs in MOF-1 at high pressure. At low pressure the adsorbates are mainly located near the linkers of the structure. However, ethylbenzene also adsorbs closer to the Dabco groups of MOF-1 and one additional snapshot showing the orientation of the molecule in the cavities of MOF-1 can be found in Appendix 3 (Figure A15).

Figure 6 shows the average occupation profiles of BTEX compounds in MIL-47 at 10^3 and 10^5 Pa. According to the adsorption isotherms, ethylbenzene is the most adsorbed molecule at 10^3 Pa. The isomers of xylene tend to be located at the centre of the channels and near the ligands, while ethylbenzene shows a slightly less localized adsorption. At 10^5 Pa ethylbenzene and ortho-xylene are evenly adsorbed, while the other components show lower values of adsorption. The isomers of xylene as well as some molecules of ethylbenzene remain near the linkers. Both meta- and para-xylene reduce their adsorption at the centre of the channels, a space occupied by ethylbenzene and ortho-xylene. Our results are in agreement with the molecular distributions and orientations previously described by Castillo *et al.*[33] (Figure A16 of Appendix 3)

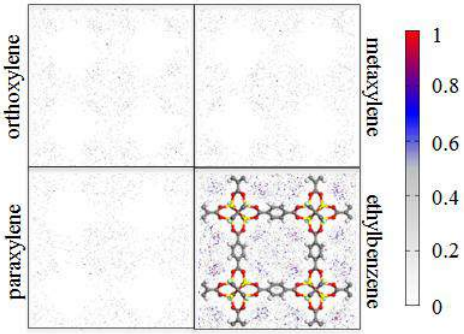

Figure 7. Average occupation profiles of ortho-, meta-, para-xylene, and ethylbenzene from the six-component mixture adsorption in IRMOF-1, at 448 K and 100 kPa. The colour gradation is related to the occupation density. For an easier understanding of the location of the molecules, a representation of the structure has been added to one of the plots.

Figure 7 shows the average occupation profiles of IRMOF-1 at 10^5 Pa. Ethylbenzene is the most adsorbed molecule, followed by ortho-, para-, and meta-xylene. The adsorbates (especially ethylbenzene) tend to be located near the metallic centres in this structure.

To support previous findings, and to improve our understanding on the behaviour of the molecules inside the structure, we compute radial distribution functions (RDFs) for the six-component equimolar mixture of BTEX. We use Monte Carlo simulations, with fixed temperature (448 K) and pressure (10^5 Pa). The obtained RDFs provide information of the probability of finding a given atom of the adsorbate at a certain distance from an atom of the structure. The RDFs are calculated for the number of molecules adsorbed on each adsorbent at the given conditions. The adsorption of toluene and benzene in the six-component mixture is almost negligible and therefore their distributions are not taken into account. The reference atoms from the structures are: The metal atom of the metallic centre, (Zn in MOF-1 and IRMOF-1, and V in MIL-47); the carbon atom labelled as C3 from the benzene ring of the organic linkers; and one of the atoms of nitrogen of the Dabco group of MOF-1. The reference atom for the adsorbates is the carbon atom of the methyl group. The obtained RDFs are shown in Figures 8 to 10.

Radial distribution functions obtained for MOF-1 (Figure 8) show a clear peak of probability for all adsorbates at 4 Å. The isomers of xylene also show a second peak at 7.5 Å. Ethylbenzene has this peak displaced to 6.5 Å, being the probability of finding ethylbenzene at this distance larger than for the other adsorbates. The RDFs obtained when one atom of nitrogen of the Dabco group is used as reference show two peaks for all molecules: one at 5.5 Å, with higher probability for ethylbenzene, and the other at ~9 Å. This second peak is slightly displaced for ethylbenzene (to 10 Å). The RDFs of the adsorbates with respect to the Zn atom in the metallic centre show three peaks for the isomers of xylene, at 5.5, 8.5, and 10.5 Å, and three less defined peaks for ethylbenzene, at around 7.5, 8.5, and 10.5 Å. According to these results, ethylbenzene is the most likely molecule to be found near the Dabco group, while the isomers of xylene tend to be located near the ligands and the metallic centres. The average occupation profiles showed that

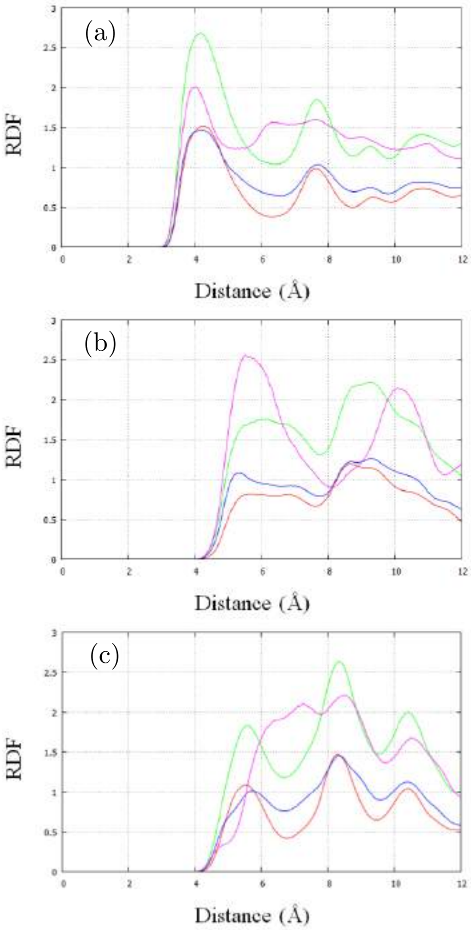

Figure 8. Computed radial distribution functions in MOF-1 of the CH_3 group of the adsorbates referring to (a) the C3 atom of the benzene group of the linker, (b) the N atom of Dabco group, and (c) the Zn atom of the metallic centre at 100 kPa and 448 K. Colour lines represent the variation of the probability with the distance for each molecule: ortho- (red), meta- (green), para-xylene (blue), and ethylbenzene (pink).

ethylbenzene and the isomers of xylene have different adsorption location. The density distribution found for ethylbenzene (Figure 5) can be related to its location near the Dabco group.

The RDFs of MIL-47 are shown in Figure 9. Taking the carbon atom of the linkers as reference atom we obtain two peaks, at 4.5 and 7.5 Å, for all adsorbates. We also found two peaks for these molecules at 5.5 and 8.5 Å using vanadium as reference atom. These results indicate that the molecules adsorb near the ligands and the metallic centres.

The peaks obtained for all adsorbates in IRMOF-1 are found at 4.5-5 Å, taking the carbon atom of the linkers or the zinc of the metallic centre as reference atom (Figure 10). The average occupation profiles obtained for IRMOF-1 showed that the molecules are near the metallic centres and the aromatic groups of the linkers.

Diffusion of BTEX compounds in metal-organic Frameworks is an interesting issue. A previous work by Rives *et al.*[41] showed the variation of the self-diffusivity of the isomers of xylene with temperature in MIL-47. They computed

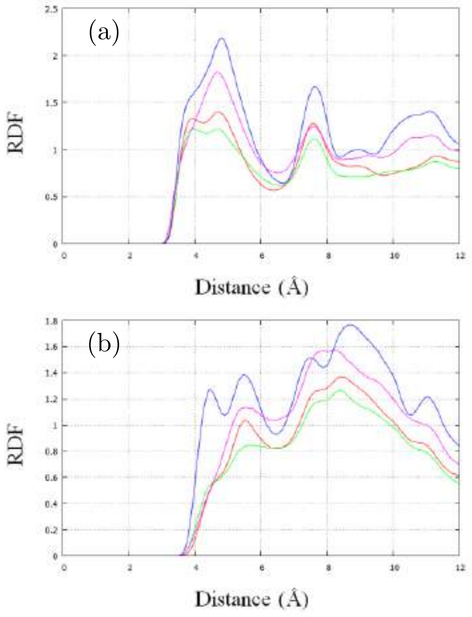

Figure 9. Computed radial distribution functions in MIL-47 of the CH_3 group of the adsorbates referring to (a) the C3 atom of the benzene group of the linker, and (b) the V atom of the metallic centre at 100 kPa and 448 K. Colour lines represent the variation of the probability with the distance for each molecule: ortho- (red), meta- (green), para-xylene (blue), and ethylbenzene (pink).

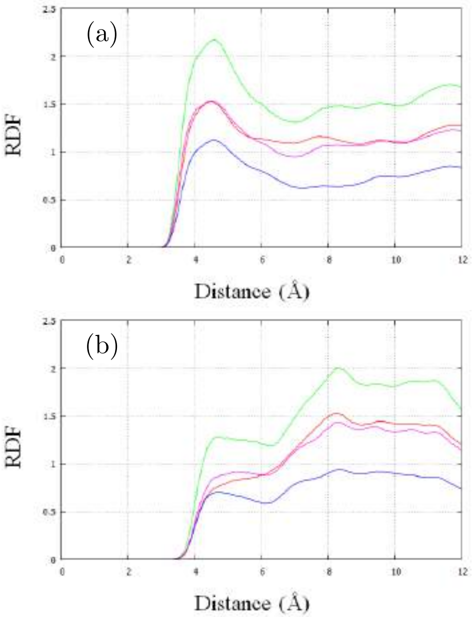

Figure 10. Computed radial distribution functions in IRMOF-1 of the CH_3 group of the adsorbates referring to (a) the C3 atom of the benzene group of the linker, and (b) the Zn atom of the metallic centre at 100 kPa and 448 K. Colour lines represent the variation of the probability with the distance for each molecule: ortho- (red), meta- (green), para-xylene (blue), and ethylbenzene (pink).

the diffusivities using Molecular Dynamic simulations for each isomer of xylene at low loading and at different temperatures. The values of the self-diffusion coefficients reported by Rives *et al.* for the isomers of xylene are in agreement with our findings. Para-xylene is the isomer with the highest diffusivity, followed by meta- and ortho-xylene in this order. We computed self-diffusion coefficients for systems containing simultaneously all BTEX components. The type and amount of molecules used for each system are taken from the six-component mixture adsorption isotherms ar 448 K and 100 kPa. This corresponds to a total loading of 62 molecules in MOF-7 (17 molecules of ortho-xylene, 9 molecules of meta-xylene, 10 molecules of para-xylene, 19 molecules of ethylbenzene, 1 molecule of benzene, and 6 molecules of toluene), 50 molecules in MIL-47 (13 molecules of ortho-xylene, 5 molecules of meta-xylene, 8 molecules of para-xylene, 15 molecules of ethylbenzene, 2 molecule of benzene, and 7 molecules of toluene), and 47 molecules in IRMOF-1 (7 molecules of ortho-xylene, 6 molecules of meta-xylene, 6 molecules of para-xylene, 21 molecules of ethylbenzene, 2 molecule of benzene, and 5 molecules of toluene). As shown in Table 1, the largest values for self-diffusion coefficients were obtained for IRMOF-1, followed by MIL-47. MOF-1 shows the lowest diffusion coefficients among the three structures.

In order to study the diffusion of the adsorbates in the structures without taking into account their relative adsorption loadings, we also computed diffusion coefficients for the single components, using the total amount of molecules inside each MOF for 62 molecules in MOF-1, 50 molecules in MIL-47, and 47 molecules in IRMOF-1 as the total loading for each component.

Table 1. Self-diffusion coefficients of the adsorbates in MOF-1, MIL-47, and IRMOF-1. MOF-1 is loaded with 17 molecules of ortho-xylene, 9 of meta-xylene, 10 of para-xylene, 19 of ethylbenzene, 1 of benzene, and 6 of toluene. MIL-47 is loaded with 13 molecules of ortho-xylene, 5 of meta-xylene, 8 of para-xylene, 15 of ethylbenzene, 2 of benzene, and 7 of toluene. IRMOF-1 is loaded with 7 molecules of ortho-xylene, 6 meta-xylene, 6 para-xylene, 21 ethylbenzene, 2 of benzene, and 5 of toluene. The error of the last digit is shown in parenthesis.

	MOF-1	MIL-47	IRMOF-1
Molecule	D ($m^2 s^{-1}$)	D ($m^2 s^{-1}$)	D ($m^2 s^{-1}$)
ortho-xylene	3.68(7) 10^{-11}	6.17(1) 10^{-10}	1.96(4) 10^{-9}
meta-xylene	3.77(2) 10^{-11}	4.20(2) 10^{-10}	1.96(2) 10^{-9}
para-xylene	6.07(9) 10^{-11}	3.47(9) 10^{-10}	1.63(2) 10^{-9}
ethylbenzene	1.95(3) 10^{-11}	4.16(4) 10^{-10}	1.84(1) 10^{-9}
benzene	8.12(9) 10^{-11}	1.12(2) 10^{-10}	2.20(3) 10^{-9}
toluene	2.30(5) 10^{-11}	7.15(3) 10^{-10}	1.97(1) 10^{-9}

Table 2. Self-diffusion coefficients of the adsorbates in MOF-1, MIL-47, and IRMOF-1. The coefficients are computed in single component simulations for each adsorbate. MOF-1 is loaded with 62 molecules of adsorbate, MIL-47 with 50 molecules of adsorbate, and IRMOF-1 with 47 molecules of adsorbate. The error of the last digit is shown in parenthesis.

	MOF-1	MIL-47	IRMOF-1
Molecule	D (m^2 s^{-1})	D (m^2 s^{-1})	D (m^2 s^{-1})
ortho-xylene	2.06(8) 10^{-11}	1.10(1) 10^{-9}	2.30(4) 10^{-9}
meta-xylene	1.81(2) 10^{-11}	8.16(6) 10^{-10}	1.32(2) 10^{-9}
para-xylene	3.45(7) 10^{-11}	9.30(7) 10^{-10}	2.21(2) 10^{-9}
ethylbenzene	2.56(6) 10^{-11}	2.01(9) 10-$^{-10}$	1.42(1) 10^{-9}
benzene	8.30(9) 10^{-11}	1.99(3) 10^{-9}	5.87(9) 10^{-9}
toluene	1.58(9) 10^{-11}	1.13(1) 10^{-9}	3.06(3) 10^{-9}

The diffusion trend obtained for the BTEX mixtures in MOF-1 is benzene > m-xylene > p-xylene ≅ o-xylene > ethylbenzene > toluene, whereas the trend obtained for pure components (Table 2) is benzene > toluene > o-xylene > p-xylene > m-xylene > ethylbenzene. As pure components, benzene and toluene are the molecules that diffuse faster due to the smaller size. It is also due to their small size that, when we compute the six-component adsorption isotherms, the adsorption of these two components is much lower that these obtained for the other components of the mixture. Therefore, though these molecules still diffuse faster than the other component of the mixture, they are hindered by the other molecules exhibiting quantitatively lower diffusion than when they were loaded as pure component in the structure. The diffusion trends for the systems containing pure components in MIL-47 and IRMOF-1 are similar to this observed for MOF-1. However, we observe interesting variations in the trends obtained for the six-component mixtures. The trends obtained for IRMOF-1 are almost the same as for pure components, i.e., benzene ≅ toluene > m-xylene ≅ ethylbenzene > o-xylene ≅ p-xylene, whereas in MIL-47 toluene becomes the slowest molecule, while benzene is still the fastest. This can be attributed to the effect of the relatively high amount of toluene molecules in the system, compared to the low number of molecules of benzene, and the interactions of those molecules with the other adsorbates.

To analyse the effect exerted by the type of model used for a given molecule, we performed additional simulations for ethylbenzene and toluene using full atom models taken from the literature.[29,42] As shown in Appendix 3 (Figures A17-A19) the average occupation profiles of these two molecules in the three MOFs are unaffected by the type of model used. However, the use of these models for the adsorption isotherms of BTEX quaternary and six-component mixtures leads to some interesting differences. Figures 11 and 12 show the adsorption selectivities obtained from the computed isotherms for the quaternary equimolar mixture of ortho-, meta-, para-xylene and ethylbenzene, and the six-component equimolar mixture of ortho-, meta-, para-xylene, ethylbenzene, benzene, and toluene, respectively. In addition, the adsorption isotherms of these equimolar mixtures are shown in Figures A20 and A21 from Appendix 3. The adsorption values of meta-, para-xylene, benzene, and toluene are not strongly affected by the type of model used for ethylbenzene and toluene. Therefore we focus the discussion on the results obtained for ortho-xylene and ethylbenzene. The adsorption of these two molecules in MOF-1 is sensitive to the type of model used. The adsorption of ethylbenzene decreases when this molecule is modelled as a full atom model, especially at high pressure. This decrease in adsorption is compensated by an increase in the overall adsorption of ortho-xylene (and also toluene in the six-component mixture). Accordingly, the adsorption selectivity of ethylbenzene decreases whereas the adsorption selectivity of ortho-xylene increases. As shown in the average occupation profiles and radial distribution functions obtained for this structure using the original molecular models (Figures 5 and 8), ethylbenzene tends to adsorb near the Dabco group. The use of full atom models for ethylbenzene and toluene provides the same preferential adsorption sites. Differences in adsorption are due to the

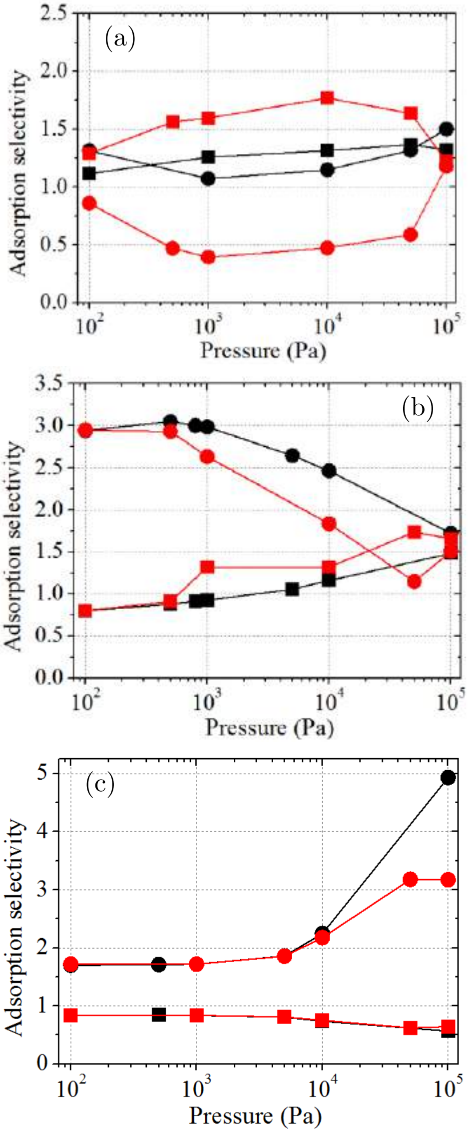

Figure 11. Adsorption selectivity of ortho- / (meta- + para-xylene + ethylbenzene) (squares) and ethylbenzene / (ortho- + meta- + para-xylene) (circles) from the adsorption isotherms of the quaternary equimolar mixture in (a) MOF-1, (b) MIL-47, and (c) IRMOF-1 at 448 K using different molecular models: original mixed models (black symbols) and full atom model of ethylbenzene (red symbols).

point charges in the hydrogen atoms of the CH_3 group, uncharged when the group is modelled as a single interaction centre. The presence of point charges in the hydrogen atoms of ethylbenzene reduces the packing efficiency of this molecule inside the structure, and therefore its overall adsorption.

The adsorption isotherm obtained for the four and six-component mixtures in MIL-47 show that the adsorption of ethylbenzene at low pressure is independent of the model used. At higher values of pressure, the use of full atom models for ethylbenzene and toluene reduces the adsorption of ethylbenzene and increases the adsorption of ortho-xylene in MIL-47. Though these variations affect to the quantitative values, adsorption selectivity follows the same trend independently of the model used. As shown in Figures 6 and 9, the corners of the channels of MIL-47 are preferential adsorption sites for ethylbenzene. The use of united atom models for the CH_3 and CH_2 groups allow the molecules of ethylbenzene to commensurate better in the corners of the channels of MIL-47. Simulations carried out with the different models for ethylbenzene and toluene in IRMOF-1 lead to similar adsorption loadings. The large cavities of this MOF allow molecular adsorption without the spatial restrictions imposed by MOF-1 and MIL-47. Independently of the molecular models used, ethylbenzene is preferentially adsorbed for all the pressures studied.

The computed radial distribution functions and the average occupation profiles obtained for the six-component

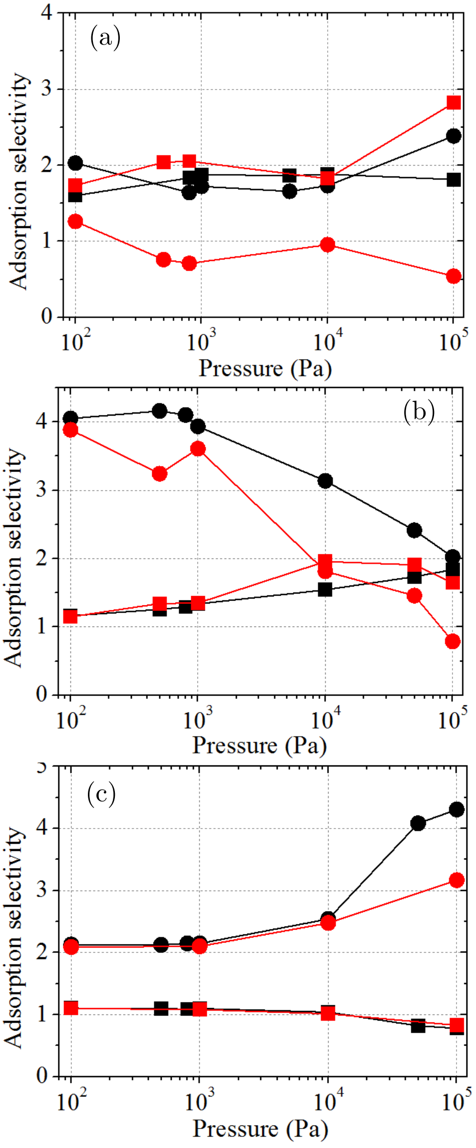

Figure 12. Adsorption selectivity of ortho- / (meta- + para-xylene + ethylbenzene + benzene + toluene) (squares) and ethylbenzene / (ortho- + meta- + para-xylene + ethylbenzene + benzene + toluene) (circles) from the adsorption isotherms of the six-component equimolar mixture in (a) MOF-1, (b) MIL-47, and (c) IRMOF-1 at 448 K using different molecular models: original mixed models (black symbols) and full atom model of ethylbenzene and toluene (red symbols).

equimolar mixtures using full atom models for ethylbenzene and toluene (Figures A22-A27 of Appendix 3) provide additional evidence that the adsorption sites are not strongly affected by the type of model. The molecules tend to be located at the same sites of the structures, but the packing inside the MOF cavities is worse when the molecules are modelled as full atoms.

Conclusions

The use of MOF-1, MIL-47 and IRMOF-1 allows separating BTEX compounds efficiently from equimolar mixtures. The three MOFs tested demonstrate different adsorption capabilities, and using one or another would depend on the needs of the desired separation. We demonstrate that the shape and size of a given structure and its cavities are the most important factors to enhance the efficiency of the separation process. Based on these properties it is possible to separate ortho-xylene, ethylbenzene, or a mixture of both for the whole range of pressure under study using one MOF or another. MOF-1 can be used to separate ortho-xylene and ethylbenzene from the mixture. This structure exhibits high selectivity in favour of ortho-xylene and ethylbenzene. MIL-47 can separate ethylbenzene from the other components of the mixture and it can also separate ortho-xylene at high pressure. The adsorption of BTEX components in IRMOF-1 below 10^3 Pa is almost negligible. However, at higher pressure, the structure successfully separates ethylbenzene from the rest of the components of the mixture. Different approaches would be needed depending on the pressure of interest in other specific separation processes.

Bibliography

(1) Castro, A. J. R.; Soares, J. M.; Filho, J. M.; Oliveira, A. C.; Campos, A.; Milet, E. R. C. *Fuel* **2013**, *108*, 740.

(2) He, J.; Li, R.; Gu, F. *Journal of Applied Polymer Science* **2013**, *128*, 1673.

(3) Dijkema, G. P. J.; Grievink, J.; Weijnen, M. P. C. *Process Safety and Environmental Protection* **2003**, *81*, 331.

(4) Mehlman, M. A. *Teratogenesis Carcinogenesis and Mutagenesis* **1990**, *10*, 399.

(5) Rosell, M.; Lacorte, S.; Barceló, D. *Journal of Chromatography A* **2006**, *1132*, 28.

(6) Baltrėnas, P.; Baltrėnaitė, E.; Šerevičienė, V.; Pereira, P. *Environmental Monitoring and Assessment* **2011**, *182*, 115.

(7) Liu, K.; Quan, J.; Mu, Y.; Zhang, Q.; Liu, J.; Gao, Y.; Chen, P.; Zhao, D.; Tian, H. *Atmospheric Environment* **2013**, *73*, 11.

(8) Seifi, L.; Torabian, A.; Kazemian, H.; Bidhendi, G.; Azimi, A.; Farhadi, F.; Nazmara, S. *Water, Air, & Soil Pollution* **2011**, *219*, 443.

(9) Torabian, A.; Kazemian, H.; Seifi, L.; Bidhendi, G. N.; Azimi, A. A.; Ghadiri, S. K. *CLEAN – Soil, Air, Water* **2010**, *38*, 77.

(10) Ranck, J. M.; Bowman, R. S.; Weeber, J. L.; Katz, L. E.; Sullivan, E.

J. *Journal of Environmental Engineering* **2005**, *131*, 434.

(11) Vidal, C. B.; Raulino, G. S. C.; Barros, A. L.; Lima, A. C. A.; Ribeiro, J. P.; Pires, M. J. R.; Nascimento, R. F. *Journal of Environmental Management* **2012**, *112*, 178.

(12) Mamedov, S. E.; Gendzhalieva, I. S.; Akhmedova, N. F. *Russian Journal of Applied Chemistry* **2013**, *86*, 116.

(13) Yaghi, O. M.; Li, G. M. *Abstracts of Papers of the American Chemical Society* **1995**, *209*, 284.

(14) Peralta, D.; Barthelet, K.; Pérez-Pellitero, J.; Chizallet, C.; Chaplais, G.; Simon-Masseron, A.; Pirngruber, G. D. *The Journal of Physical Chemistry C* **2012**, *116*, 21844.

(15) Dybtsev, D. N.; Chun, H.; Kim, K. *Angewandte Chemie-International Edition* **2004**, *43*, 5033.

(16) Alaerts, L.; Kirschhock, C. E. A.; Maes, M.; van der Veen, M. A.; Finsy, V.; Depla, A.; Martens, J. A.; Baron, G. V.; Jacobs, P. A.; Denayer, J. E. M.; De Vos, D. E. *Angewandte Chemie-International Edition* **2007**, *46*, 4293.

(17) Eddaoudi, M.; Kim, J.; Rosi, N.; Vodak, D.; Wachter, J.; O'Keeffe, M.; Yaghi, O. M. *Science* **2002**, *295*, 469.

(18) Barcia, P. S.; Nicolau, M. P. M.; Gallegos, J. M.; Chen, B. L.; Rodrigues, A. E.; Silva, J. A. C. *Microporous and Mesoporous Materials* **2012**, *155*, 220.

(19) Finsy, V.; Verelst, H.; Alaerts, L.; De Vos, D.; Jacobs, P. A.; Baron, G. V.; Denayer, J. F. M. *Journal of the American Chemical Society* **2008**, *130*, 7110.

(20) Barthelet, K.; Marrot, J.; Riou, D.; Férey, G. *Angewandte Chemie International Edition* **2002**, *41*, 281.

(21) Mishra, P.; Edubilli, S.; Mandal, B.; Gumma, S. *Microporous and Mesoporous Materials* **2013**, *169*, 75.

(22) Yaghi, O. M.; Li, H. *Journal of the American Chemical Society* **1995**, *117*, 10401.

(23) Xuan, W.; Zhu, C.; Liu, Y.; Cui, Y. *Chem Soc Rev* **2012**, *41*, 1677.

(24) Dubbeldam, D.; Walton, K. S.; Ellis, D. E.; Snurr, R. Q. *Angewandte Chemie-International Edition* **2007**, *46*, 4496.

(25) Vlugt, T. J. H.; Schenk, M. *Journal of Physical Chemistry B* **2002**, *106*, 12757.

(26) Garcia-Sanchez, A.; Dubbeldam, D.; Calero, S. *Journal of Physical Chemistry C* **2010**, *114*, 15068.

(27) Mayo, S. L.; Olafson, B. D.; Goddard, W. A. *Journal of Physical Chemistry* **1990**, *94*, 8897.

(28) Rappe, A. K.; Casewit, C. J.; Colwell, K. S.; Goddard, W. A.; Skiff, W. M. *Journal of the American Chemical Society* **1992**, *114*, 10024.

(29) Bueno-Perez, R.; Garcia-Perez, E.; Jose Gutierrez-Sevillano, J.; Merkling, P. J.; Calero, S. *Adsorption Science & Technology* **2010**, *28*, 823.

(30) Dubbeldam, D.; Galvin, C. J.; Walton, K. S.; Ellis, D. E.; Snurr, R. Q. *Journal of the American Chemical Society* **2008**, *130*, 10884.

(31) Frost, H.; Snurr, R. Q. *Journal of Physical Chemistry C* **2007**, *111*, 18794.

(32) Dubbeldam, D.; Frost, H.; Walton, K. S.; Snurr, R. Q. *Fluid Phase Equilibria* **2007**, *261*, 152.

(33) Castillo, J. M.; Vlugt, T. J. H.; Calero, S. *Journal of Physical Chemistry C* **2009**, *113*, 20869.

(34) Rai, N.; Siepmann, J. I. *J Phys Chem B* **2007**, *111*, 10790.

(35) Jorgensen, W. L.; Nguyen, T. B. *Journal of Computational Chemistry* **1993**, *14*, 195.

(36) Caleman, C.; van Maaren, P. J.; Hong, M.; Hub, J. S.; Costa, L. T.; van der Spoel, D. *Journal of Chemical Theory and Computation* **2012**, *8*, 61.

(37) Düren, T.; Sarkisov, L.; Yaghi, O. M.; Snurr, R. Q. *Langmuir* **2004**, *20*, 2683.

(38) Frenkel, D.; Smit, B. *Understanding molecular simulation: from algorithms to applications*; Access Online via Elsevier, 2001.

(39) Dubbeldam, D.; Calero, S.; Ellis, D. E.; Snurr, R. Q. *Molecular Simulation* **2016**, *42*, 81.

(40) Garcia-Perez, E.; Gascon, J.; Morales-Florez, V.; Manuel Castillo, J.; Kapteijn, F.; Calero, S. *Langmuir* **2009**, *25*, 1725.

(41) Rives, S.; Jobic, H.; Kolokolov, D. I.; Gabrienko, A. A.; Stepanov, A. G.; Ke, Y.; Frick, B.; Devic, T.; Ferey, G.; Maurin, G. *Journal of Physical Chemistry C* **2013**, *117*, 6293.

(42) Allen, M. P.; Tildesley, D. J. *Computer simulation of liquids*; Oxford university press, 1989.

5

Conclusions

This thesis highlights the usefulness of molecular simulation techniques towards the study of the adsorption and diffusion of gas mixtures. With the level of tunability shown by metal-organic frameworks, there is an interest in testing many different structures to understand the effect of different topologies, metallic centres and ligand length. Computer simulations allow for time-efficient and reliable tests using different gas compositions and molecular sieves.

The main conclusions of this thesis are:

1.- The analysis of adsorption isotherms for different ethane-ethylene mixtures in IRMOFs indicate that interpenetrated structures are better suited for the selective separation of ethane.

2.- The use of ZIFs serves to compare an array of topologies. Reviewing the adsorption results for binary mixtures of ethane and ethylene, structures with large pores and *lta* topology (ZIF-20, -22) show a marked preferential adsorption of ethane over ethylene.

3.- Taking a closer look into industrially relevant mixture data, a seven-component mixture of ethane, ethylene, carbon monoxide, carbon dioxide, oxygen, hydrogen and methane is used. Structures with *cga* (ZIF-4, -62) and *lta* (ZIF-20, -22) topologies show preferential adsorption of ethane.

4.- After considering the dynamic behaviour of the adsorbates, the ideal candidates for separation may vary. In ZIFs, structures with *rho* (ZIF-71, -93, -96, and -97), *crg* (ZIF-2) and *lta* (ZIF-20, -22) topologies exhibit a great capacity for adsorbing ethane in multicomponent mixtures.

5.- The existence of channels within a structure, as opposed to localized cavities and communicating windows, helps with the close arrangement of longer molecules, as derived from the permselectivity calculations made for BTEX mixtures. Ethylbenzene molecules are able to stand close together inside the channels of MIL-47.

6.- Large linker molecules take up a measurable amount of space inside the structures. They can have a dramatic effect on the adsorption of small organic molecules (ethane and ethylene), with the adsorption preference being reversed compared to structures with slinkier ligands. This effect is highlighted when taking into account the diffusion of the molecules. Ethylene has a slightly higher permselectivity value over ethane in IRMOF-16, in contrast to the other IRMOF structures used.

7.- The larger cavity formed by IRMOF-1 ligands causes the adsorption of BTEX components to start at higher values of pressure when compared to the smaller MOF-1 structure. Larger molecules such as ethylbenzene are allowed to adsorb better within the pores of IRMOF-1, whereas the xylene isomers are the preferentially adsorbed components on MOF-1.

8.- The presence of a chemically inert component such as nitrogen can enhance the adsorption of some species over the others. The presence of a high concentration of nitrogen allows for a competition at low partial pressures of ethane and ethylene, where the ethane adsorption can be favoured in some structures (ZIF-20, -22).

9.- Using a multicomponent mixture of seven gases is useful to test the industrial environment of ethane/ethylene separation. Although overall adsorption loading decreases, as the amount of ethane and ethylene is lower in the bulk, the selectivity towards ethane may be increased in large structures (ZIF-20, -22).

10.- The presence of a differential structural feature among the adsorbates may serve as a lead towards the selective separation of a compound. Adsorption and diffusion results for ethylbenzene depict a preferential separation in the larger structures tested, where this molecule fits better than the bulkier components of the BTEX mixtures.

These conclusions have been reached using data provided with molecular simulation techniques. The tunability of the mixture conditions generates a large number of valuable results, from which said conclusions may be reached. The application of our advances in experimental setups is key to reduce the time and financial investment required to enhance industrial processes.

Resumen (Summary in Spanish)

En la presente tesis, se propone el uso de técnicas de simulación molecular como un método rápido y eficaz para el estudio de sistemas moleculares complejos. Esta tesis se centra en procesos relevantes de la industria química que presentan pasos optimizables a nivel químico o que requieran grandes consumos de energía actualmente. Los métodos de separación de compuestos que se proponen pueden ser de utilidad en la industria química, especialmente en procesos petroquímicos. Esta tesis se divide en tres capítulos, con cada capítulo ofreciendo alternativas a procesos de separación conocidos a nivel industrial, en los que el uso de MOFs puede ser beneficioso.

Estudio del efecto del tipo y tamaño del ligando en la adsorción de parafinas y olefinas (Capítulo 2)

A lo largo de esta tesis, se estudia el efecto que tienen las diferencias estructurales y químicas de los MOFs sobre la adsorción de diferentes compuestos. Una de las principales características estructurales que puede ser modificada es el tipo de ligando orgánico. En el Capítulo 2 se analizan las diferencias en rendimiento adsortivo de miembros de la familia de los IRMOFs. Se atiende en especial al efecto que del tipo de ligando orgánico presente tiene sobre la adsorción y difusión de los adsorbatos. Se utilizan varias mezclas de etano/etileno, y se estudia la adsorción en distintas estructuras, en busca de una con potencial para realizar la separación de estos compuestos lineales.

Se estudia a su vez el efecto en los procesos de adsorción de la longitud del ligando orgánico y de la presencia de cajas interpenetradas. Se describen varias estructuras con capacidad para adsorber preferentemente etano, obteniendo un efluente rico en etileno.

Efecto de la topología estructural en la adsorción de parafinas y olefinas (Capítulo 3)

Se utilizan diferentes mezclas para estimar la capacidad de separación de varias estructuras. A nivel experimental, las mezclas de etano/etileno contienen una alta proporción de nitrógeno. El efecto que tiene la presencia del nitrógeno ha sido estudiado en la tesis, siguiendo propuestas experimentales previas que describen la separación de etileno en condiciones similares en zeolitas. Siendo estructuras topológicamente equivalentes, se han empleado ZIFs para estudiar la adsorción de los compuestos descritos. Al utilizar diferentes ZIFs, se busca comparar diferentes topologías, buscando aquellas que permitan una separación optimizada. Para evitar otros posibles efectos más allá de las diferencias topológicas, las simulaciones se han limitado a ZIFs con centros metálicos de zinc.

De forma adicional, se ha estudiado la adsorción en estas estructuras de mezclas más complejas, siguiendo guías de proporciones industriales. Se utiliza una mezcla de siete componentes (etano, etileno, hidrógeno, oxígeno, dióxido de carbono, monóxido de carbono y metano) y se comparan los resultados de adsorción entre las distintas topologías empleadas. Se han encontrado varias estructuras con capacidad para separar etano, lo cual permitiría facilitar la separación completa de etano y etileno a nivel industrial.

Adsorción de compuestos aromáticos similares (Capítulo 4)

La separación de etilbenceno de mezclas BTEX es un proceso con un alto interés industrial. Mezclas de benceno, tolueno, etilbenceno e isómeros de xileno se encuentran en procesos petroquímicos, en los que resulta decisivo obtener mezclas enriquecidas en etilbenceno. Al ser los compuestos BTEX similares, se busca encontrar estructuras capaces de adsorber diferencialmente alguno de ellos, en especial etilbenceno. Se estudia el efecto de la topología de las estructuras. Para ello, se comparan MOFs que se dividen estructuralmente en cajas interconectadas con MOFs que se caracterizan por formar canales unidimensionales (MIL-47).

Adicionalmente a la influencia que estar estructurados en cajas o canales tiene sobre la adsorción de gases, se estudia la orientación de los ligandos orgánicos, así como el tipo de centros metálicos. Se encuentran estructuras capaces de separar tanto etilbenceno como orto-xileno, otro compuesto con importancia industrial.

De esta tesis, cabe destacar la utilidad de las técnicas de simulación molecular en el estudio de la adsorción y difusión de mezclas de gases. Dado el nivel de variabilidad descrito para las estructuras metal-orgánicas (MOFs), resulta interesante comparar el comportamiento de diferentes estructuras en la adsorción de compuestos. Se puede estudiar el efecto de las diferentes topologías, ligandos orgánicos y centros metálicos presentes en estos MOFs. El utilizar simulaciones moleculares permite realizar un alto número de pruebas en diferentes condiciones de forma eficiente y fidedigna.

Las principales conclusiones que se alcanzan son:

1.- El análisis de isotermas de adsorción para diferentes mezclas de etano-etileno en IRMOFs permite concluir que las estructuras interpenetradas ofrecen mejores resultados para la separación selectiva de etano.

2.- El estudio de la adsorción en ZIFs permite comparar diferentes topologías. En mezclas binarias de etano y etileno, las estructuras con topología lta y poros de gran tamaño (ZIF-20, -22) muestran una adsorción preferente de etano.

3.- Se estudian mezclas con relevancia industrial de etano y etileno, en concreto una mezcla de siete componentes que también incluye monóxido de carbono, dióxido de carbono, oxígeno, hidrógeno y metano. El etano se adsorbe preferentemente en estructuras con topología cag (ZIF-4, -62) y lta (ZIF-20, -22).

4.- Al tener en cuenta el comportamiento dinámico de los adsorbatos, las estructuras ideales para realizar la separación pueden variar. En ZIFs, las estructuras con topología rho (ZIF-71, -93, -96, and -97), crg (ZIF-2) y lta (ZIF-20, -22) demuestran una gran capacidad para adsorber etano en mezclas de dos, tres y siete componentes.

5.- La presencia de canales unidimensionales en una estructura, en lugar de poros intercomunicados, es beneficiosa para la adsorción de moléculas con estructura elongada. En el estudio de mezclas BTEX, y teniendo en cuenta cálculos de permselectividad, las moléculas de etilbenceno pueden permanecer más juntas dentro de los canales de MIL-47 que las del resto de componentes de la mezcla.

6.- Los ligandos de IRMOF-1 forman una cavidad de mayor tamaño que los de MOF-1, lo que provoca que la adsorción de los compuestos BTEX comience a niveles de presión más altos. Moléculas largas como el etilbenceno pueden adsorber más fácilmente en los poros mayores de IRMOF-1, mientras que los isómeros de xileno muestran una adsorción preferente en MOF-1.

7.- Ligandos orgánicos que ocupan un tamaño considerable en el interior de la estructura pueden provocar efectos directos en la adsorción de moléculas orgánicas pequeñas, como etano y etileno. Este tipo de compuestos se adsorben con mayor facilidad en estructuras con ligandos menos voluminosos. Este efecto se ve ensalzado al estudiar la difusión de los adsorbatos. A modo de ejemplo, el etileno tiene un nivel de permselectividad sobre etano superior en IRMOF-16 que en otras estructuras isorreticulares empleadas.

8.- La presencia de compuestos inertes como el nitrógeno puede mejorar la adsorción de determinadas especies químicas. Estando en altas concentraciones, el nitrógeno provoca una competición del resto de adsorbatos, etano y etileno, a bajas presiones parciales. La adsorción de etano se ve favorecida por la presencia de nitrógeno en determinadas estructuras (ZIF-20, -22).

9.- La separación de etano/etileno se ve influenciada por la presencia de otros compuestos, como se observa en los resultados de la mezcla de siete componentes. La adsorción a nivel absoluto decrece, debido a la menor cantidad relativa de etano y etileno en la mezcla original, si bien la selectividad de etano se ve incrementada en algunas estructuras (ZIF-20, -22).

10.- La presencia de elementos estructurales distintos entre los adsorbatos puede ser motivo de la separación preferencial de un compuesto sobre otro. Los resultados de adsorción y difusión de etilbenceno muestran una adsorción preferencial de este compuesto sobre el resto de componentes de la mezcla BTEX en estructuras con espacios grandes, a los cuales esta molécula se puede adaptar mejor que los isómeros de xileno, benceno o tolueno.

Se ha llegado a estas conclusiones desde el estudio de datos de simulación molecular. La variabilidad de mezclas generada ha derivado en un gran número de resultados. La aplicación de estos avances y conclusiones en sistemas experimentales es la clave para reducir el tiempo y la inversión de recursos requeridos para mejorar los procesos industriales descritos.

Appendix 1

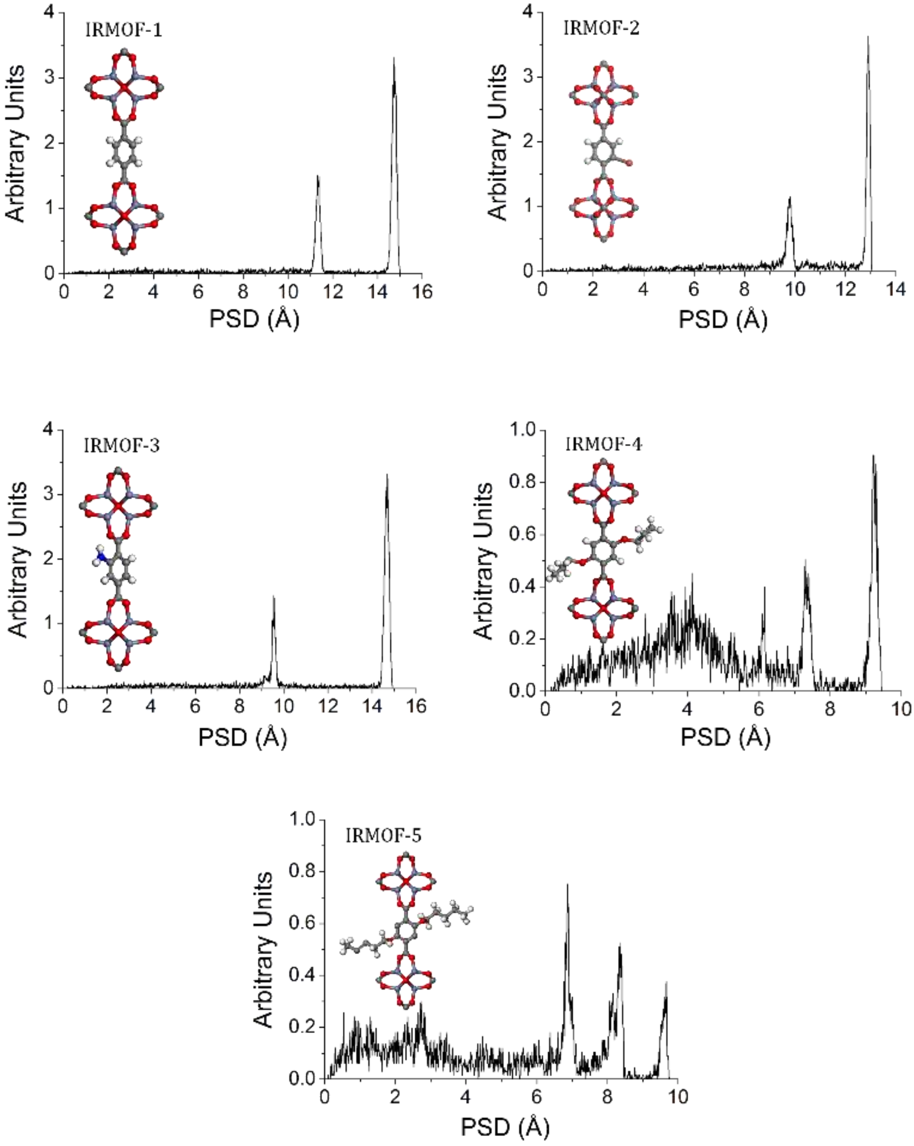

Figure A1. Pore Size Distribution of IRMOF-n (n=1-5). These structures contain the same organic linker with different functionalization. A representation of the organic linker of each structure is added for clarity.

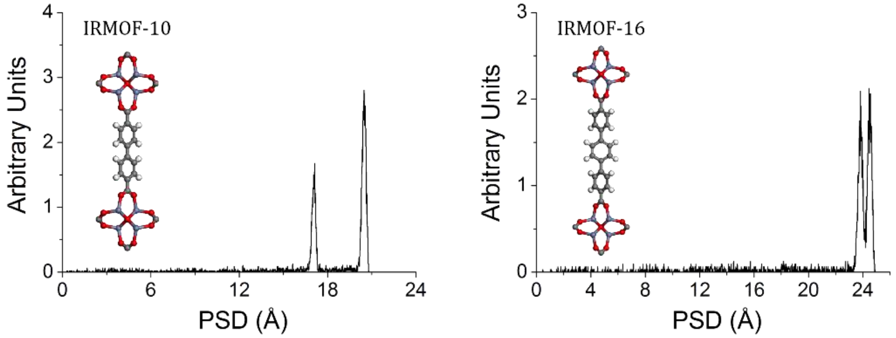

Figure A2. Pore Size Distribution of IRMOF-10 and -16. These structures have the same organic linker than IRMOF-1 but with increasing number of phenyl groups. A representation of the organic linker of each structure is added for clarity.

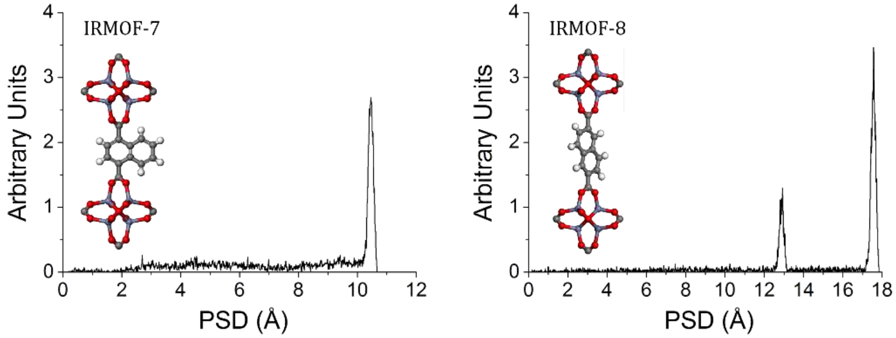

Figure A3. Pore Size Distribution of IRMOF-7 and -8. These structures have two cyclic groups as happens in IRMOF-10, but they are connected differently. A representation of the organic linker of each structure is added for clarity.

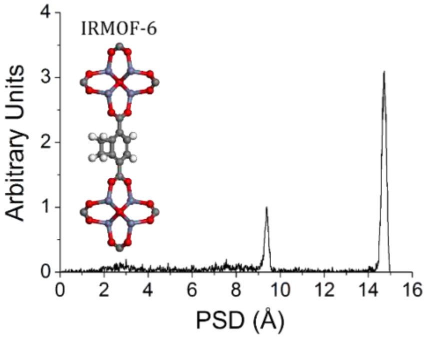

Figure A4. Pore Size Distribution of IRMOF-6. This structure has a heterocycle composed by 4 and 6 member rings sharing two carbon atoms. A representation of the organic linker of the structure is added for clarity.

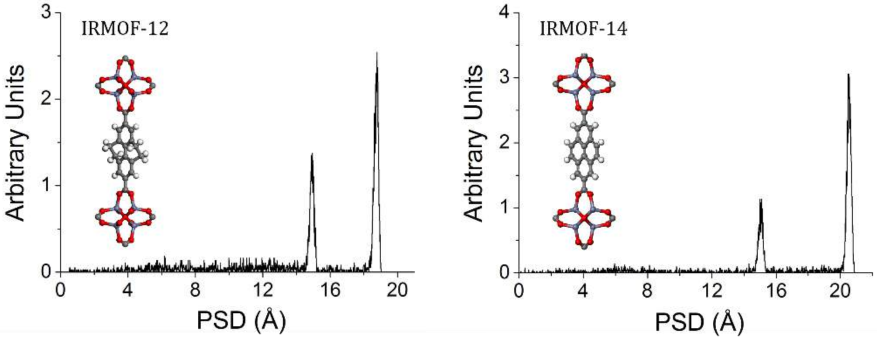

Figure A5. Pore Size Distribution of IRMOF-12 and -14. These structures have four connected cyclic groups, but different number of hydrogen atoms. A representation of the organic linker of each structure is added for clarity.

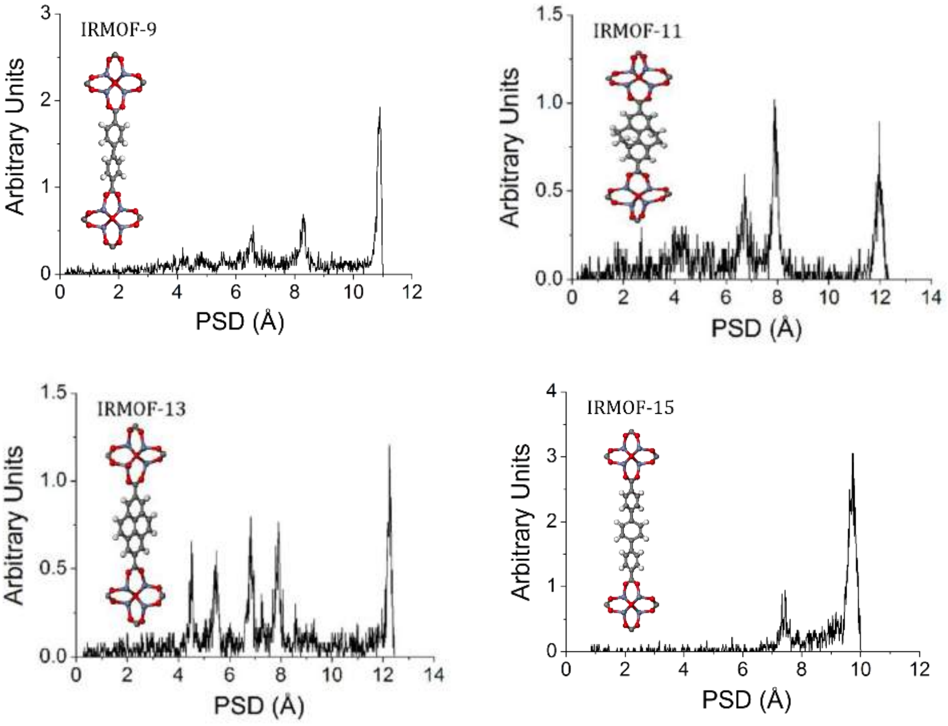

Figure A6. Pore Size Distribution of IRMOF-9, -11, -13, and -15. These structures are similar than IRMOF-10, -12, -14, and -16 but with interpenetrated cavities. A representation of the organic linker of each structure is added for clarity.

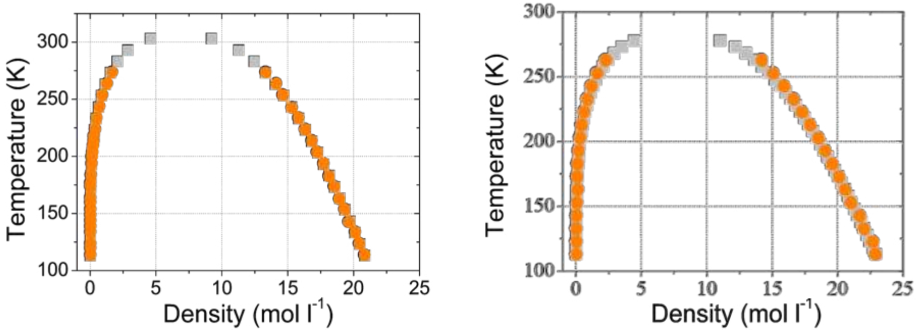

Figure A7. Vapour-Liquid Equilibrium curves of ethane (left) and ethylene (right). Comparison of experimental data (grey squares)[1] with the values obtained by simulation (orange circles).

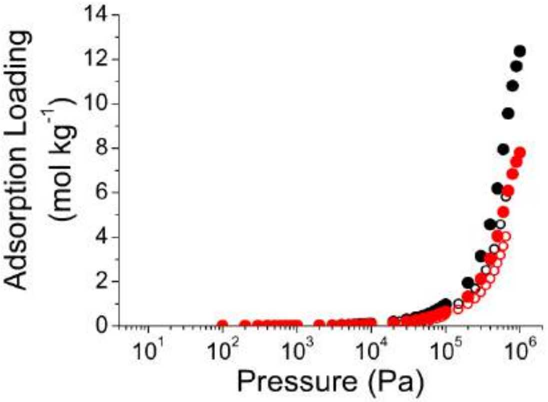

Figure A8. Adsorption isotherms for the equimolar mixture of ethane (black symbols) and ethylene (red symbols) at 298 K in IRMOF-8. Open symbols depict simulation results by Pillai *et al.* [2] Our simulation results are shown in full symbols.

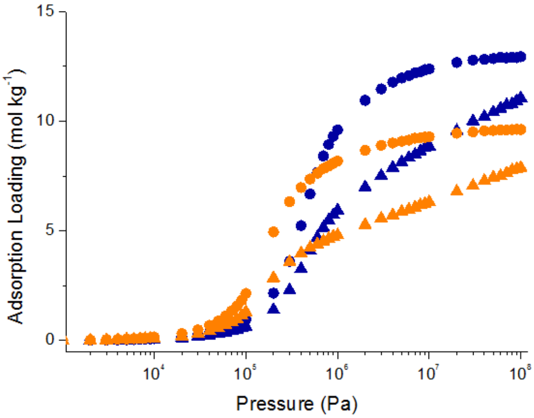

Figure A9. Adsorption isotherms for the equimolar mixture of ethane (circles) and ethylene (triangles) at 298 K in IRMOF-1 (blue) and IRMOF-7 (orange).

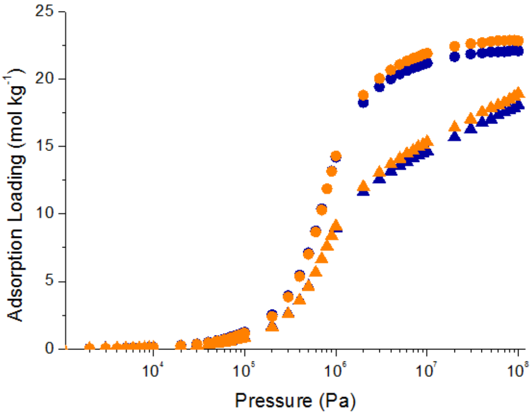

Figure A10. Adsorption isotherms for the equimolar mixture of ethane (circles) and ethylene (triangles) at 298 K in IRMOF-12 (blue) and IRMOF-14 (orange).

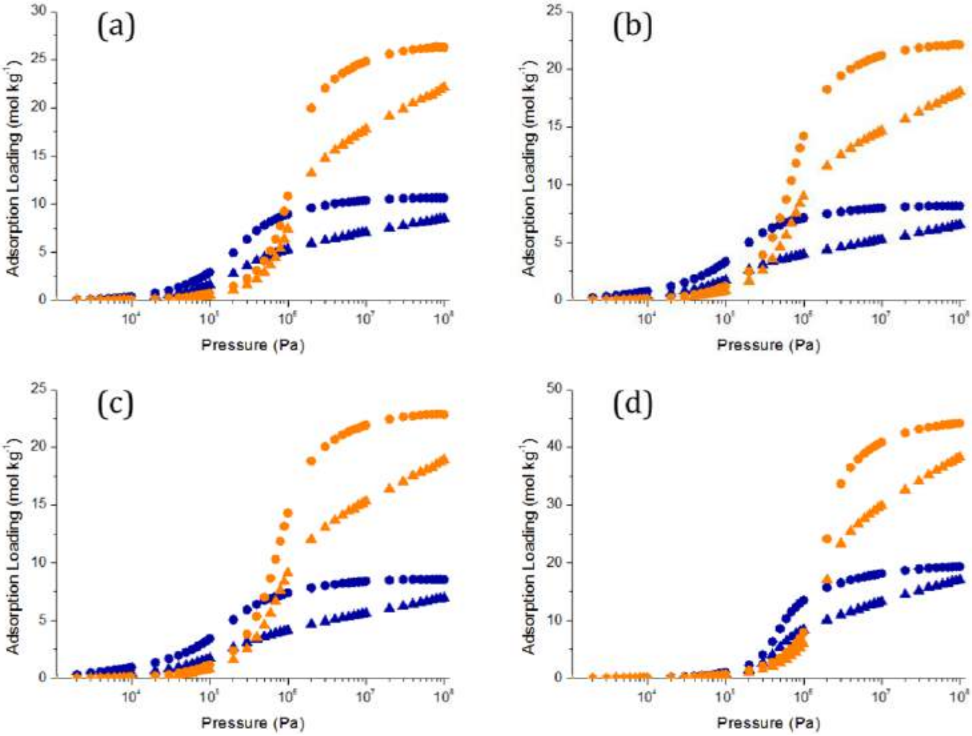

Figure A11. Adsorption isotherms for the equimolar mixture of ethane (circles) and ethylene (triangles) at 298 K in IRMOF-10, -12, -14, and -16 (orange) with their respective interpenetrated versions (blue) (a) IRMOF-9 vs. IRMOF-10, b) IRMOF-11 vs. IRMOF-12, c) IRMOF-13 vs. IRMOF-14, and d) IRMOF-15 vs. IRMOF-16.

Table A1. Size of the functional groups of the IRMOFs and largest difference in adsorption (LDA) between ethane and ethylene. The LDA were taken from the adsorption isotherms of the equimolar mixture in IRMOF-2, -3, -4, and -5.

Structure	Size of functional group (Å)	LDA (mol/kg)
IRMOF-2	2.076 (C-Br)	3.152
IRMOF-3	2.044 (C-H_NH_2)	3.661
IRMOF-4	5.538 (C-H_C3alkyl)	2.231
IRMOF-5	7.870 (C-H_C3alkyl)	1.145

Table A2. Self-diffusion coefficients (10^{-8} m^2/s) of ethane (top) and ethylene (bottom) from binary mixtures using the number of molecules adsorbed in the IRMOFs at 100 kPa and 298 K.

Structure	10:90	20:80	30:70	40:60	50:50	60:40	70:30	80:20	90:10
IRMOF-1	0.296	0.518	0.453	0.389	0.411	0.393	0.399	0.386	0.452
	0.528	0.500	0.522	0.463	0.503	0.466	0.570	0.423	0.491
IRMOF-2	0.336	0.369	0.395	0.382	0.391	0.375	0.385	0.392	0.378
	0.469	0.476	0.473	0.433	0.504	0.426	0.474	0.409	0.354
IRMOF-3	0.261	0.254	0.272	0.273	0.262	0.320	0.252	0.273	0.246
	0.345	0.316	0.326	0.346	0.355	0.302	0.311	0.316	0.259
IRMOF-6	0.158	0.212	0.265	0.238	0.228	0.241	0.236	0.231	0.231
	0.293	0.329	0.263	0.359	0.287	0.279	0.280	0.351	0.301
IRMOF-7	0.349	0.321	0.314	0.308	0.296	0.290	0.288	0.283	0.282
	0.333	0.360	0.364	0.331	0.345	0.324	0.347	0.319	0.332
IRMOF-8	0.445	0.458	0.529	0.508	0.477	0.485	0.458	0.454	0.486
	0.604	0.564	0.600	0.648	0.617	0.575	0.586	0.631	0.545
IRMOF-9	0.248	0.249	0.262	0.257	0.270	0.266	0.279	0.260	0.276
	0.316	0.312	0.326	0.305	0.309	0.304	0.323	0.285	0.311
IRMOF-10	0.885	0.659	0.802	0.760	0.734	0.693	0.805	0.787	0.770
	0.918	0.937	0.827	0.830	1.023	0.744	0.953	0.982	0.759
IRMOF-11	0.166	0.169	0.173	0.186	0.185	0.184	0.181	0.185	0.181
	0.207	0.212	0.219	0.215	0.203	0.218	0.221	0.220	0.210
IRMOF-12	0.488	0.609	0.582	0.502	0.578	0.572	0.528	0.505	0.483
	0.657	0.618	0.657	0.663	0.680	0.611	0.743	0.639	0.619
IRMOF-13	0.156	0.160	0.162	0.172	0.178	0.175	0.175	0.176	0.180
	0.202	0.211	0.217	0.216	0.211	0.229	0.219	0.220	0.214
IRMOF-14	0.550	0.524	0.540	0.572	0.517	0.523	0.545	0.474	0.546
	0.680	0.692	0.729	0.698	0.658	0.694	0.594	0.695	0.713
IRMOF-15	1.203	1.071	1.033	1.118	1.074	1.047	1.038	1.014	1.050
	1.192	1.227	1.190	1.226	1.215	1.237	1.199	1.079	1.198
IRMOF-16	1.153	1.139	1.134	1.136	1.030	1.135	1.119	1.148	1.164
	1.487	1.499	1.557	1.488	1.456	1.557	1.523	1.516	1.495

Table A3. Ethane/ethylene adsorption selectivity obtained from the adsorption isotherms of binary mixtures in the IRMOFs at 298 K and 100 kPa. Due to the lack of diffusion of ethane and ethylene in IRMOF-4 and -5, these two structures are excluded.

Structure	10:90	20:80	30:70	40:60	50:50	60:40	70:30	80:20	90:10
IRMOF-1	1.503	1.499	1.503	1.504	1.504	1.517	1.506	1.5125	1.516
IRMOF-2	1.599	1.601	1.606	1.613	1.615	1.618	1.626	1.619	1.632
IRMOF-3	1.589	1.577	1.583	1.585	1.586	1.589	1.597	1.600	1.598
IRMOF-6	1.652	1.657	1.660	1.668	1.669	1.673	1.675	1.676	1.670
IRMOF-7	1.614	1.618	1.629	1.633	1.638	1.652	1.655	1.661	1.666
IRMOF-8	1.455	1.461	1.461	1.461	1.464	1.457	1.467	1.464	1.463
IRMOF-9	1.774	1.773	1.769	1.770	1.768	1.765	1.769	1.763	1.769
IRMOF-10	1.393	1.388	1.393	1.388	1.388	1.389	1.391	1.388	1.385
IRMOF-11	1.919	1.913	1.912	1.907	1.905	1.903	1.902	1.898	1.899
IRMOF-12	1.498	1.494	1.492	1.500	1.496	1.498	1.488	1.493	1.488
IRMOF-13	1.995	1.984	1.978	1.969	1.956	1.954	1.949	1.945	1.940
IRMOF-14	1.473	1.476	1.476	1.471	1.475	1.478	1.468	1.468	1.471
IRMOF-15	1.461	1.458	1.457	1.459	1.457	1.454	1.455	1.455	1.455
IRMOF-16	1.345	1.339	1.343	1.340	1.341	1.338	1.343	1.340	1.340

Table A4. Ethane/ethylene permselectivity from binary mixtures in the IRMOFs at 298 K and 100 kPa. Due to the lack of diffusion of ethane and ethylene in IRMOF-4 and -5, these two structures are excluded.

Structure	10:90	20:80	30:70	40:60	50:50	60:40	70:30	80:20	90:10
IRMOF-1	0.841	1.552	1.303	1.264	1.230	1.278	1.054	1.379	1.396
IRMOF-2	1.147	1.242	1.344	1.424	1.254	1.425	1.322	1.553	1.745
IRMOF-3	1.202	1.270	1.316	1.249	1.174	1.683	1.295	1.384	1.518
IRMOF-6	0.890	1.069	1.673	1.103	1.322	1.443	1.415	1.101	1.283
IRMOF-7	1.690	1.442	1.403	1.520	1.408	1.478	1.377	1.476	1.417
IRMOF-8	1.071	1.189	1.287	1.146	1.132	1.229	1.148	1.053	1.306
IRMOF-9	1.392	1.415	1.424	1.494	1.545	1.543	1.527	1.604	1.566
IRMOF-10	1.342	0.977	1.352	1.270	0.995	1.294	1.175	1.113	1.405
IRMOF-11	1.533	1.524	1.512	1.650	1.740	1.607	1.557	1.598	1.635
IRMOF-12	1.112	1.473	1.322	1.138	1.271	1.401	1.058	1.178	1.161
IRMOF-13	1.536	1.498	1.474	1.571	1.648	1.494	1.555	1.560	1.635
IRMOF-14	1.193	1.118	1.093	1.206	1.159	1.114	1.346	1.002	1.126
IRMOF-15	1.474	1.272	1.264	1.330	1.289	1.231	1.260	1.368	1.276
IRMOF-16	1.043	1.017	0.978	1.023	0.949	0.975	0.987	1.015	1.043

(1) Linstrom, P.; Mallard, W. G. *NIST Standard Reference Database Number 69; National Institute of Standards and Technology: Gaithersburg, MD, ; RN 108-88- 3; http://webbook.nist.gov* **June 2005**.

(2) Pillai, R. S.; Pinto, M. L.; Pires, J.; Jorge, M.; Gomes, J. R. B. *Acs Applied Materials & Interfaces* **2015**, *7*, 624.

Appendix 2

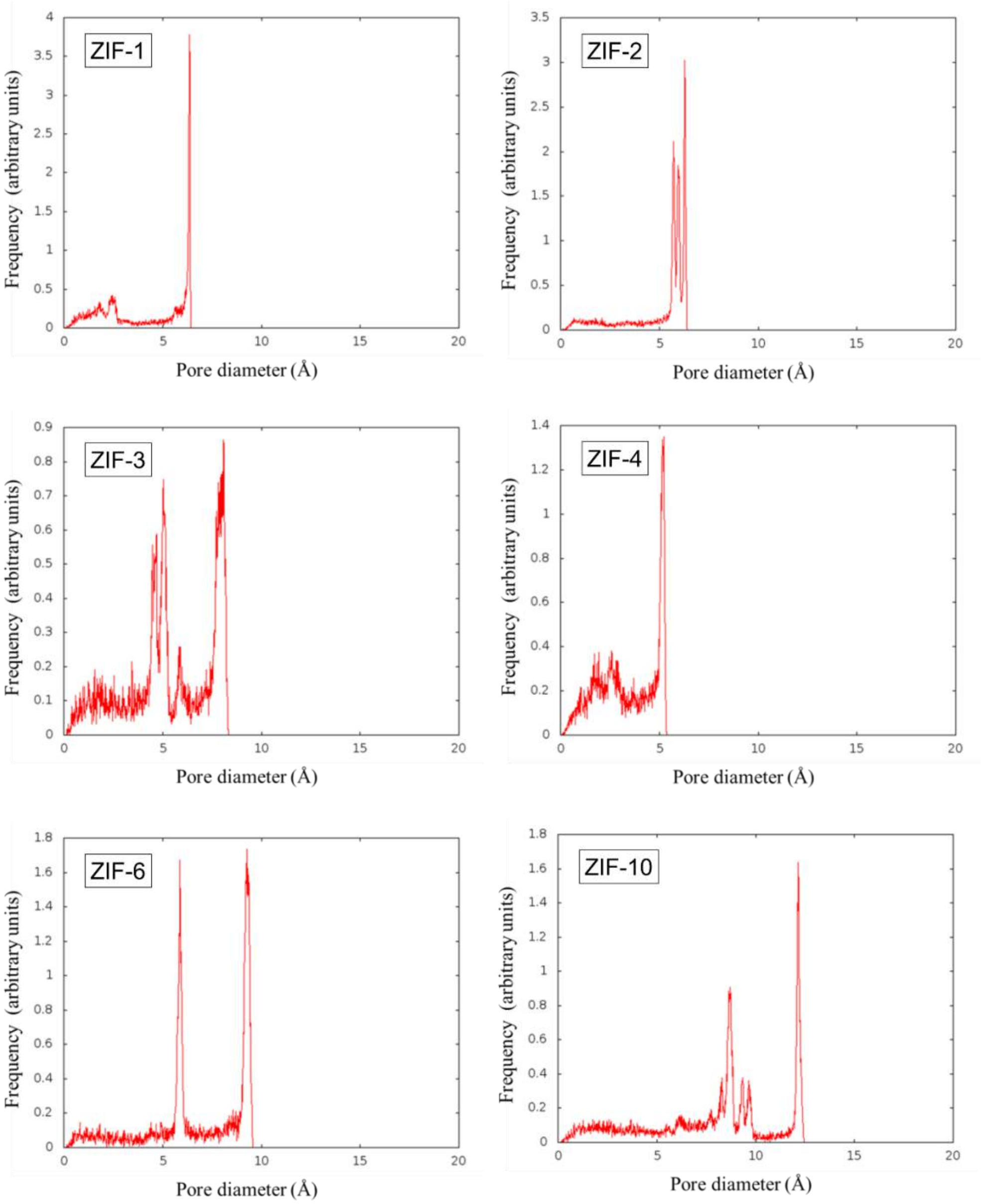

Figure A1. Pore size distribution of ZIF-1, -2, -3, -4, -6, and -10.

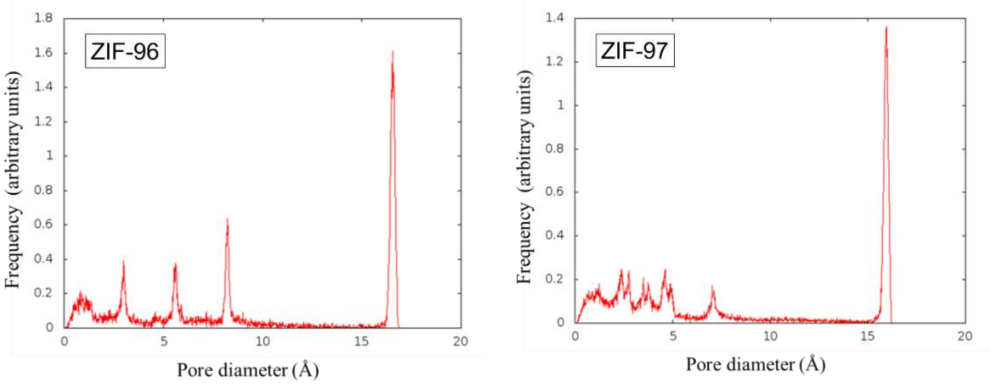

Figure A2. Pore size distribution of ZIF-71, -93, -96, and -97.

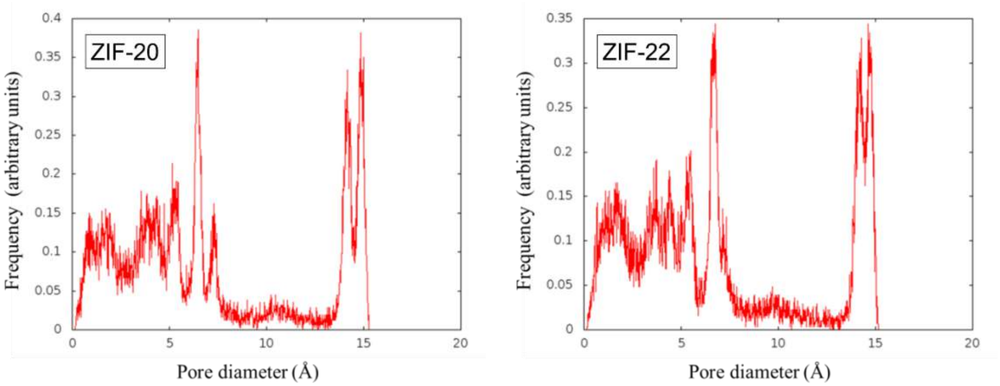

Figure A3. Pore size distribution of ZIF-20 and -22.

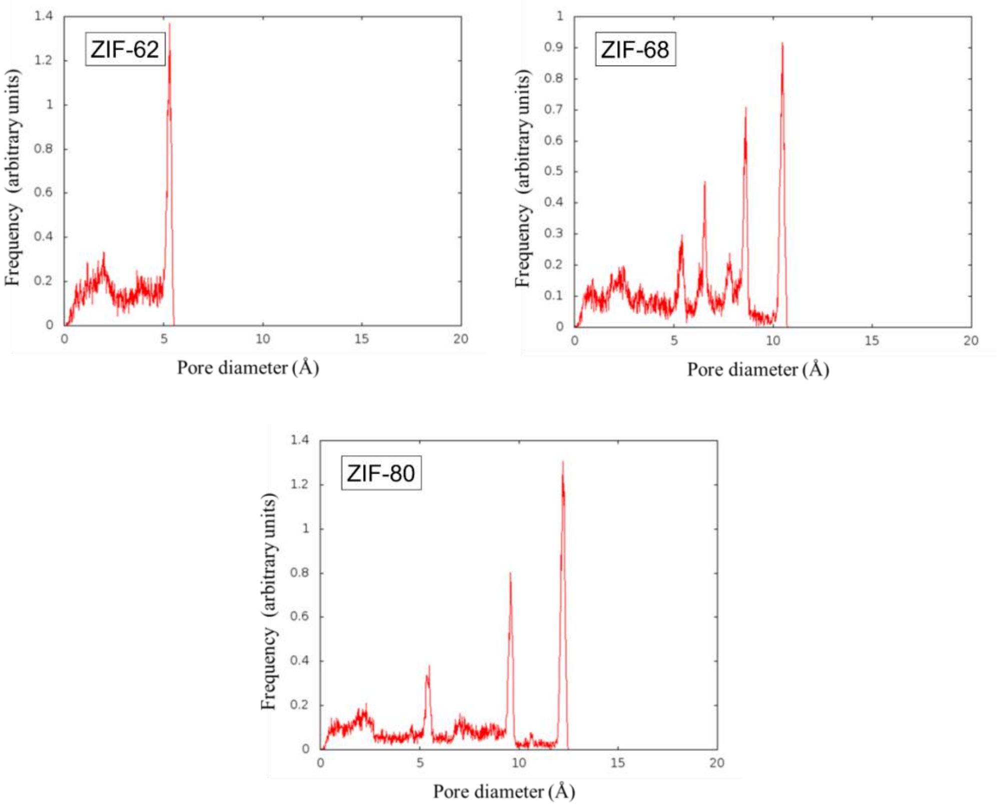

Figure A4. Pore size distribution of ZIF-62, -68, and -80.

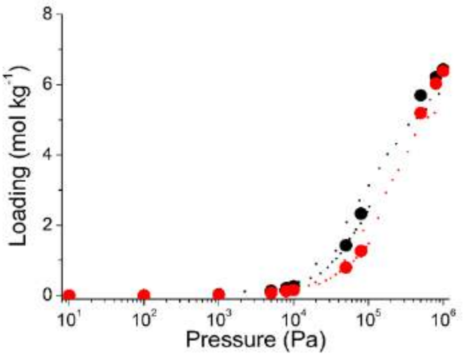

Figure A5. Pure component adsorption isotherms of ethane (large black symbols) and ethylene (large red symbols) in ZIF-8 at 298 K. Experimental data from H. Bux *et al.*[1] and U. Böhme *et al.*[2] are shown in dots. Simulation results are shown in circles. Error bars are within the symbol size.

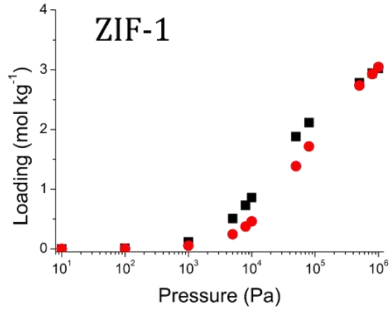
ZIF-1
Loading (mol kg^{-1})
0
1
2
3
4
10^1
10^2
10^3
10^4
10^5
10^6
Pressure (Pa)

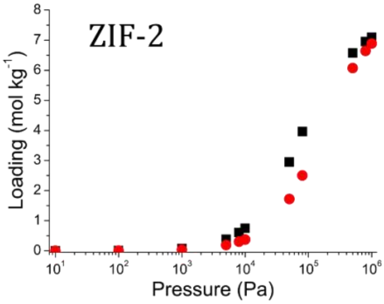
ZIF-2
Loading (mol kg^{-1})
0
1
2
3
4
5
6
7
8
10^1
10^2
10^3
10^4
10^5
10^6
Pressure (Pa)

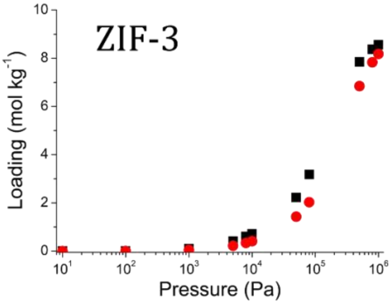
ZIF-3
Loading (mol kg^{-1})
0
2
4
6
8
10
10^1
10^2
10^3
10^4
10^5
10^6
Pressure (Pa)

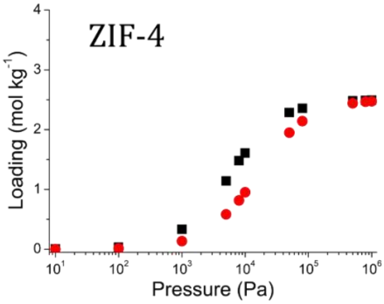
ZIF-4
Loading (mol kg^{-1})
0
1
2
3
4
10^1
10^2
10^3
10^4
10^5
10^6
Pressure (Pa)

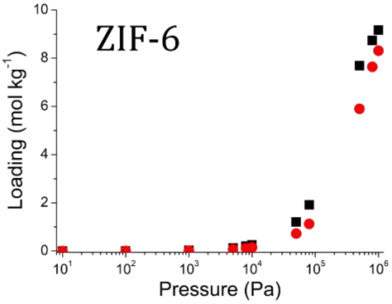
ZIF-6
Loading (mol kg^{-1})
0
2
4
6
8
10
10^1
10^2
10^3
10^4
10^5
10^6
Pressure (Pa)

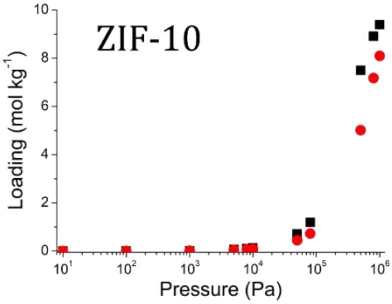
ZIF-10
Loading (mol kg^{-1})
0
2
4
6
8
10
10^1
10^2
10^3
10^4
10^5
10^6
Pressure (Pa)

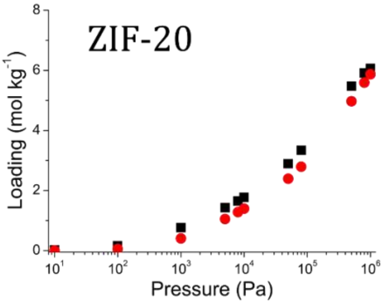
ZIF-20
Loading (mol kg^{-1})
0
2
4
6
8
10^1
10^2
10^3
10^4
10^5
10^6
Pressure (Pa)

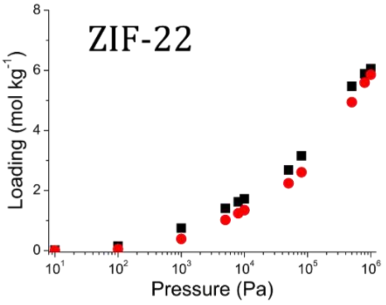
ZIF-22
Loading (mol kg^{-1})
0
2
4
6
8
10^1
10^2
10^3
10^4
10^5
10^6
Pressure (Pa)

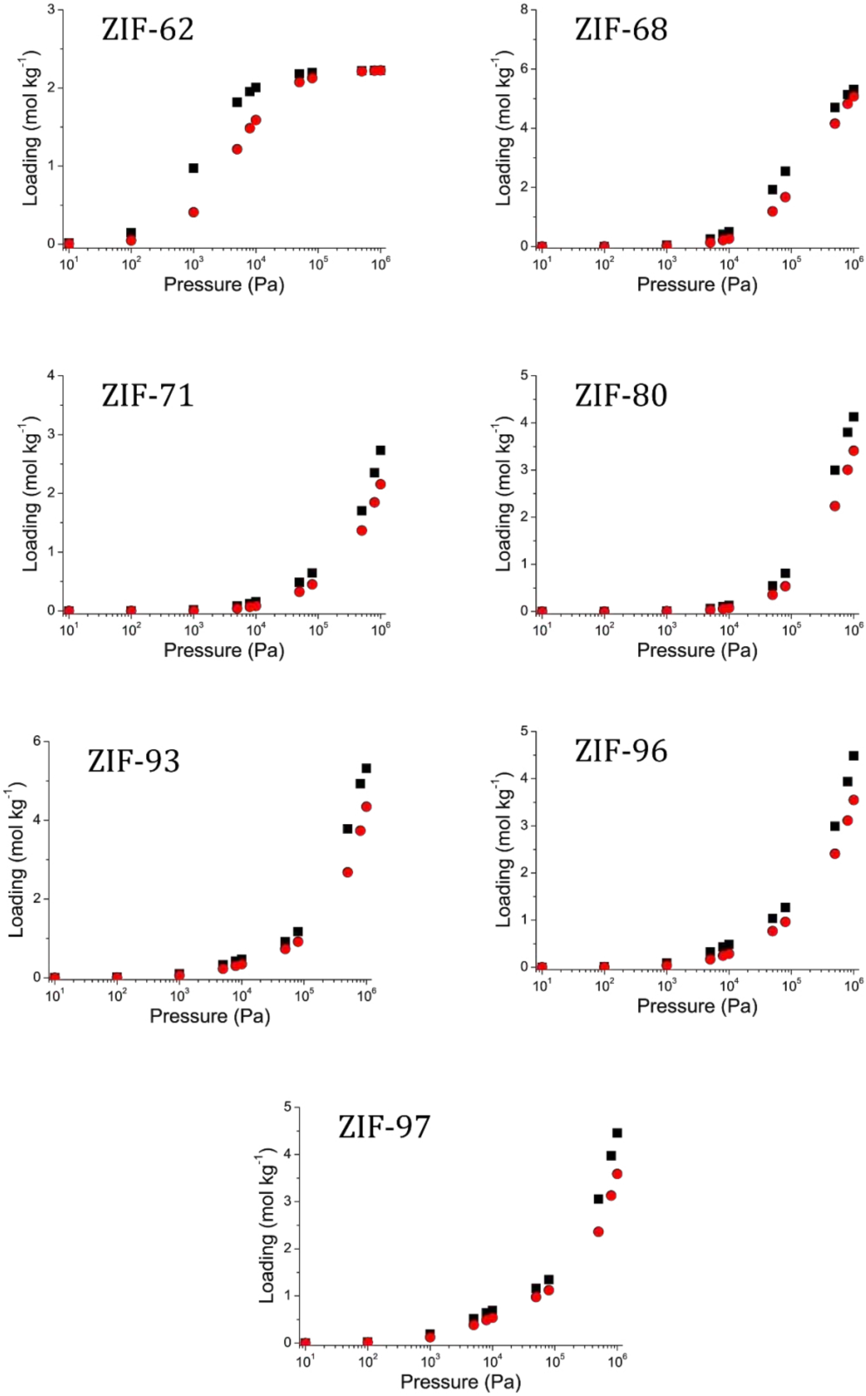

Figure A6. Pure component adsorption isotherms of ethane (black squares) and ethylene (red circles) in several ZIFs at 298 K. Error bars are within the symbol size.

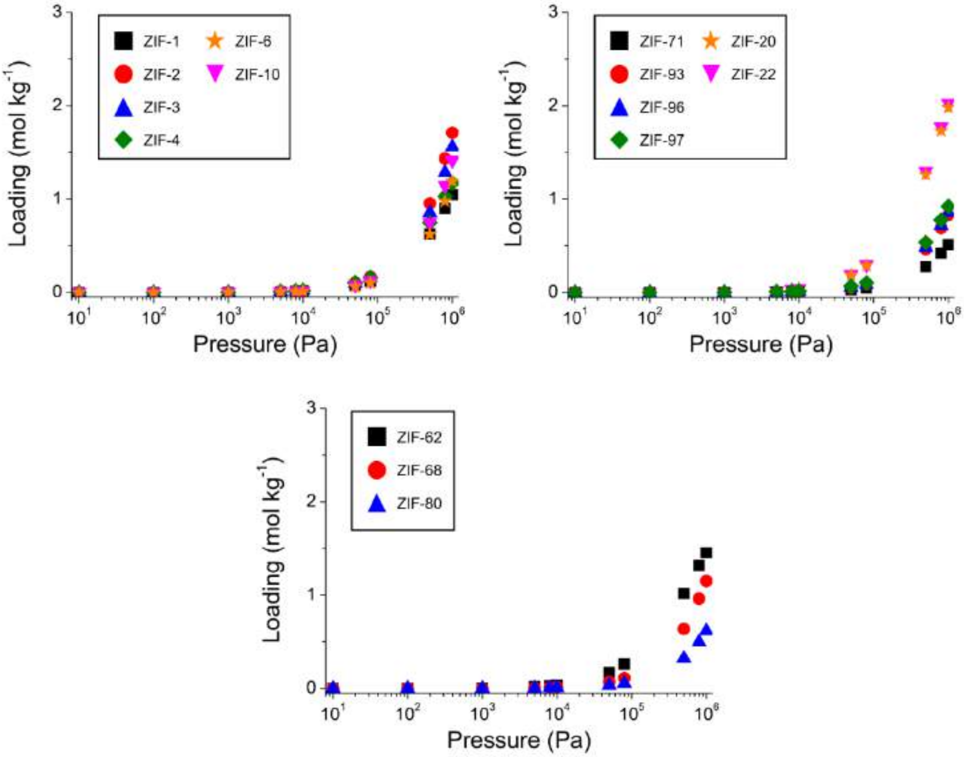

Figure A7. Pure component adsorption isotherms of nitrogen in several ZIFs at 298 K. Error bars are within the symbol size.

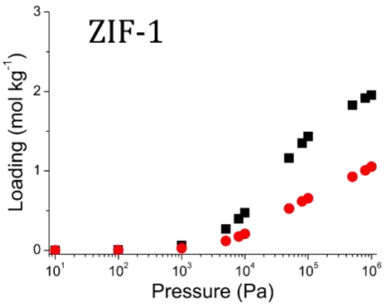
ZIF-1
Loading (mol kg^{-1})
0
1
2
3
10^1
10^2
10^3
10^4
10^5
10^6
Pressure (Pa)

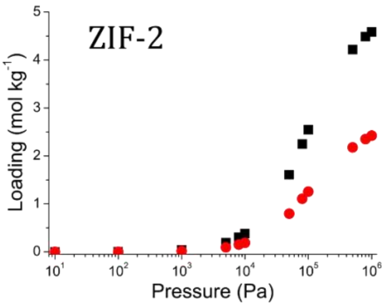
ZIF-2
Loading (mol kg^{-1})
0
1
2
3
4
5
10^1
10^2
10^3
10^4
10^5
10^6
Pressure (Pa)

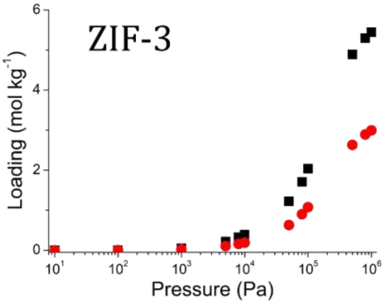
ZIF-3
Loading (mol kg^{-1})
0
2
4
6
10^1
10^2
10^3
10^4
10^5
10^6
Pressure (Pa)

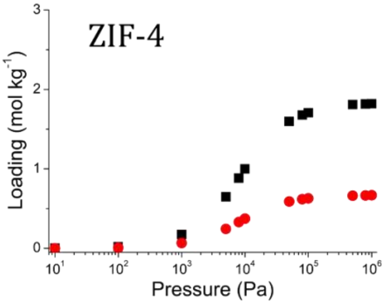
ZIF-4
Loading (mol kg^{-1})
0
1
2
3
10^1
10^2
10^3
10^4
10^5
10^6
Pressure (Pa)

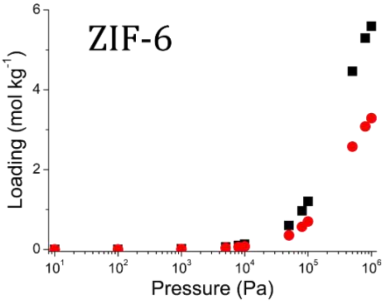
ZIF-6
Loading (mol kg^{-1})
0
2
4
6
10^1
10^2
10^3
10^4
10^5
10^6
Pressure (Pa)

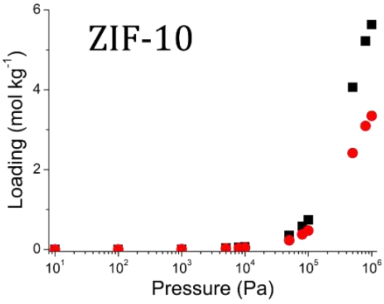
ZIF-10
Loading (mol kg^{-1})
0
2
4
6
10^1
10^2
10^3
10^4
10^5
10^6
Pressure (Pa)

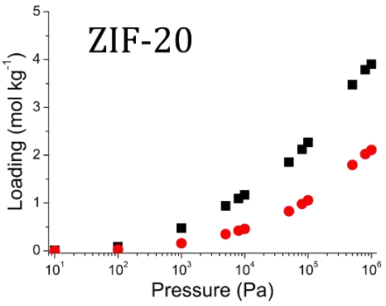
ZIF-20
Loading (mol kg^{-1})
0
1
2
3
4
5
10^1
10^2
10^3
10^4
10^5
10^6
Pressure (Pa)

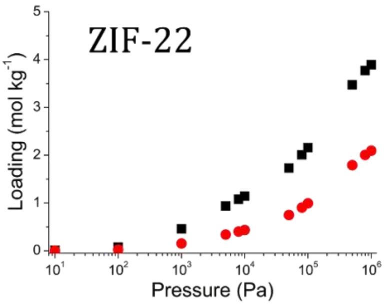
ZIF-22
Loading (mol kg^{-1})
0
1
2
3
4
5
10^1
10^2
10^3
10^4
10^5
10^6
Pressure (Pa)

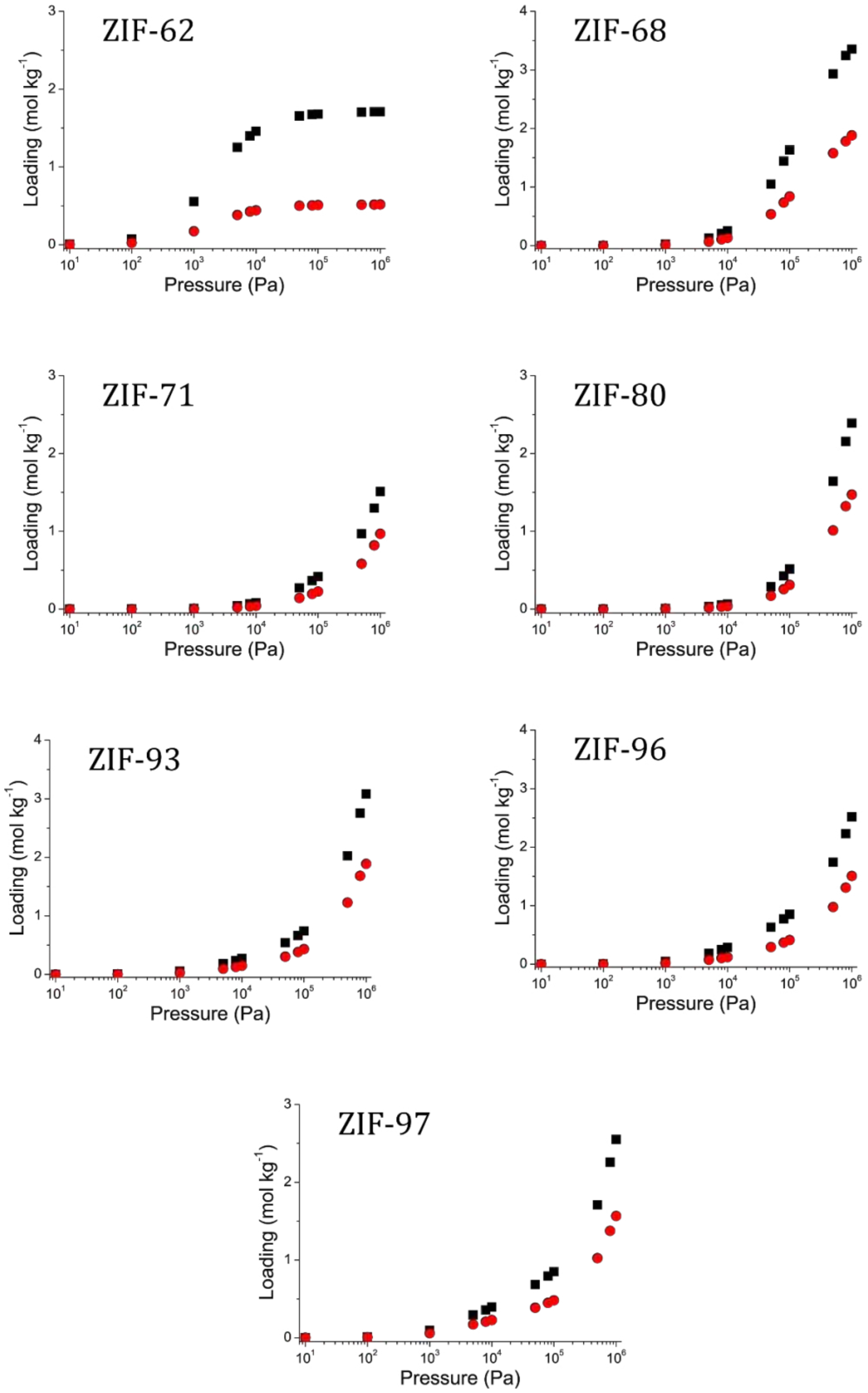

Figure A8. Adsorption isotherms of ethane (black squares) and ethylene (red circles) from the 50:50 binary mixture in several ZIFs at 298 K. Error bars are within the symbol size.

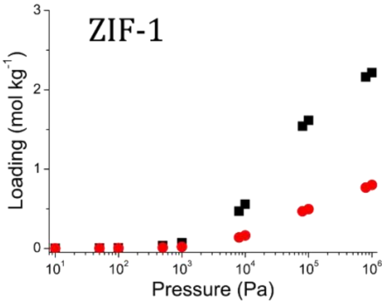
ZIF-1
Loading (mol kg^{-1})
0
1
2
3
Pressure (Pa)
10^1
10^2
10^3
10^4
10^5
10^6

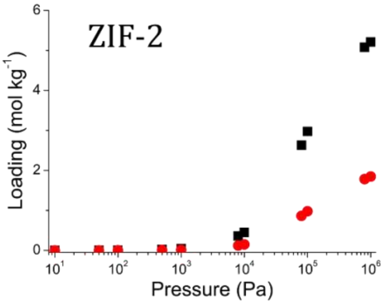
ZIF-2
Loading (mol kg^{-1})
0
2
4
6
Pressure (Pa)
10^1
10^2
10^3
10^4
10^5
10^6

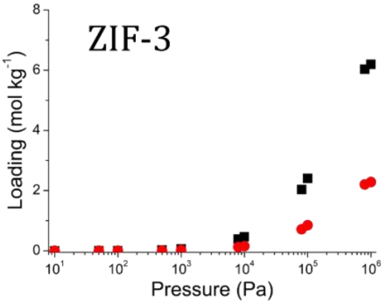
ZIF-3
Loading (mol kg^{-1})
0
2
4
6
8
Pressure (Pa)
10^1
10^2
10^3
10^4
10^5
10^6

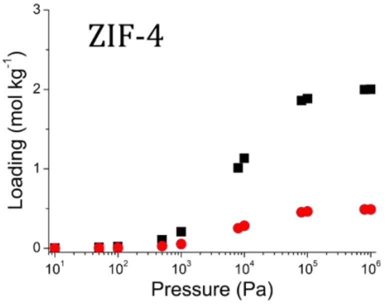
ZIF-4
Loading (mol kg^{-1})
0
1
2
3
Pressure (Pa)
10^1
10^2
10^3
10^4
10^5
10^6

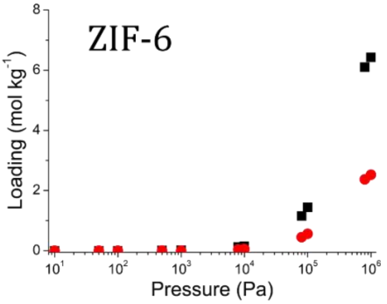
ZIF-6
Loading (mol kg^{-1})
0
2
4
6
8
Pressure (Pa)
10^1
10^2
10^3
10^4
10^5
10^6

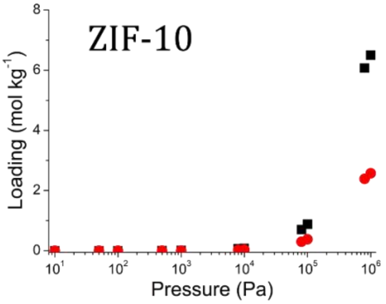
ZIF-10
Loading (mol kg^{-1})
0
2
4
6
8
Pressure (Pa)
10^1
10^2
10^3
10^4
10^5
10^6

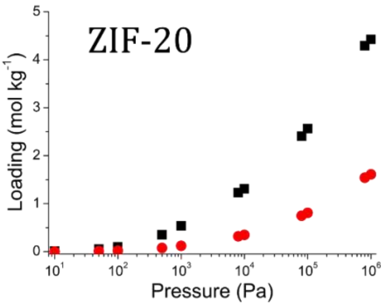
ZIF-20
Loading (mol kg^{-1})
0
1
2
3
4
5
Pressure (Pa)
10^1
10^2
10^3
10^4
10^5
10^6

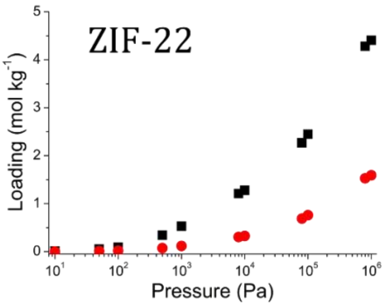
ZIF-22
Loading (mol kg^{-1})
0
1
2
3
4
5
Pressure (Pa)
10^1
10^2
10^3
10^4
10^5
10^6

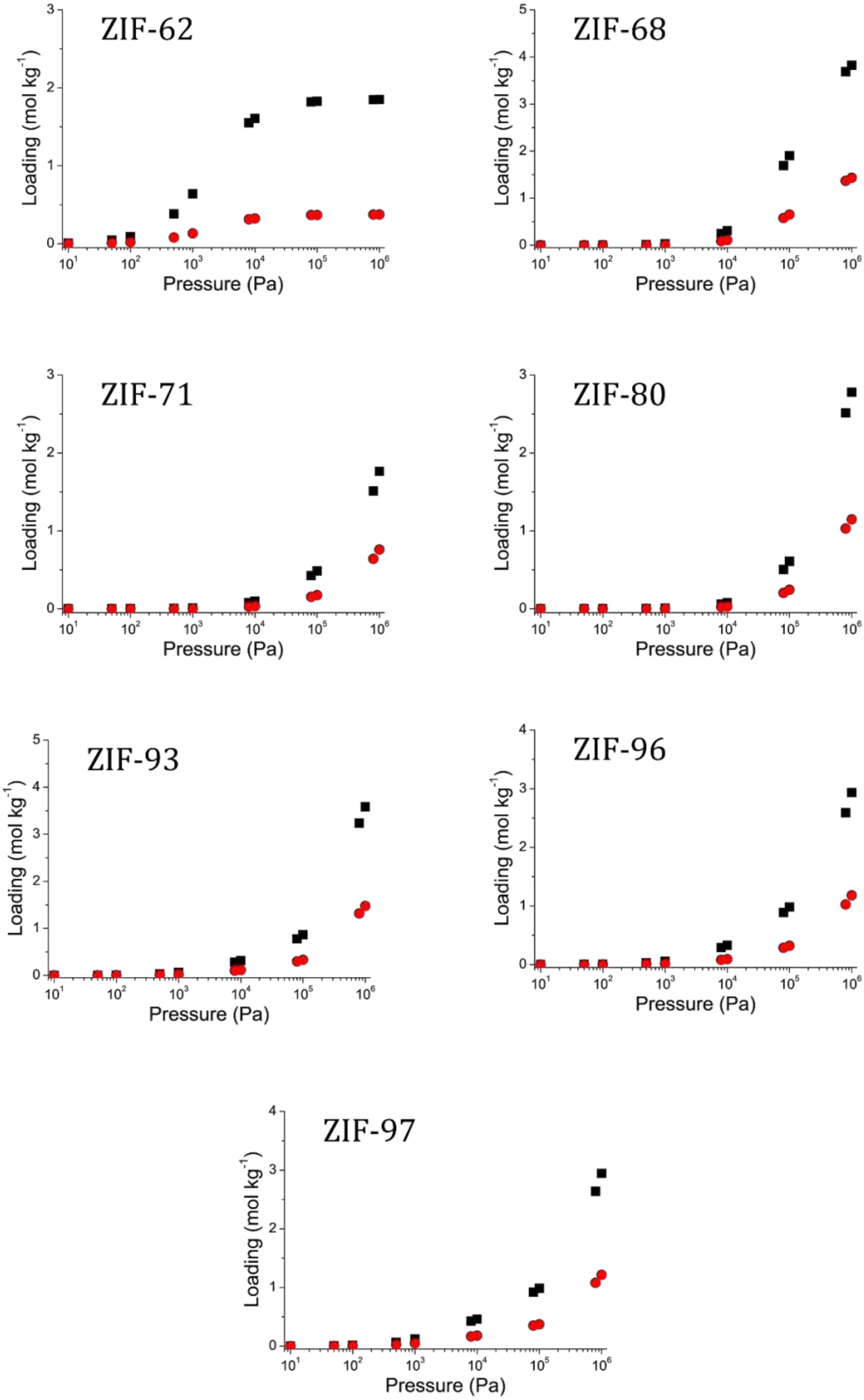

Figure A9. Adsorption isotherms of ethane (black squares) and ethylene (red circles) from the 60:40 binary mixture in several ZIFs at 298 K. Error bars are within the symbol size.

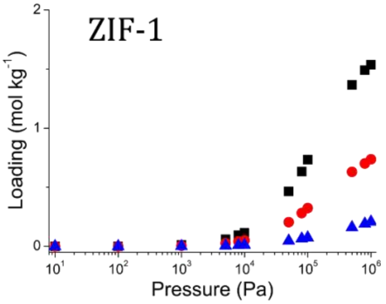
ZIF-1

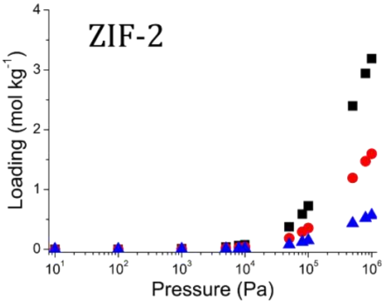
ZIF-2

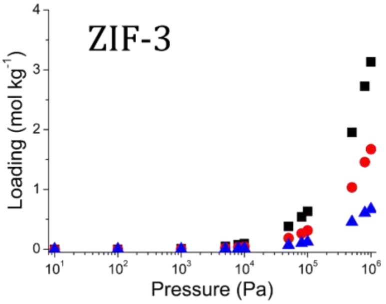
ZIF-3

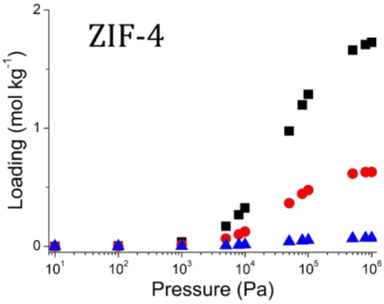
ZIF-4

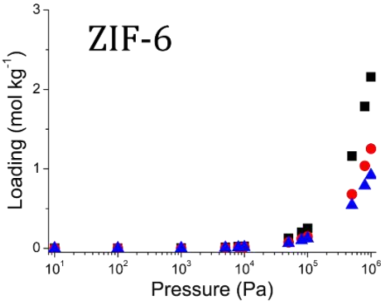
ZIF-6

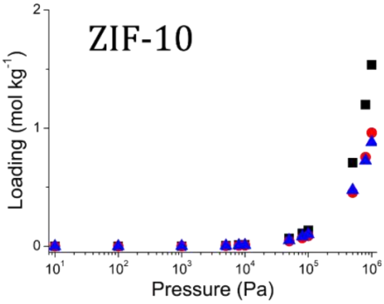
ZIF-10

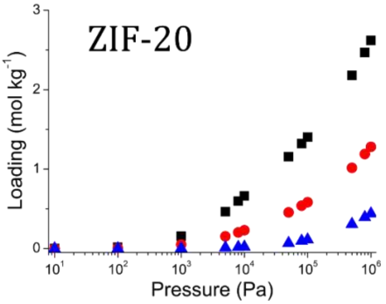
ZIF-20

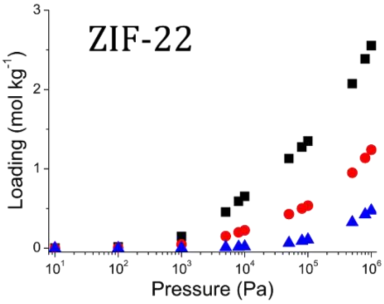
ZIF-22

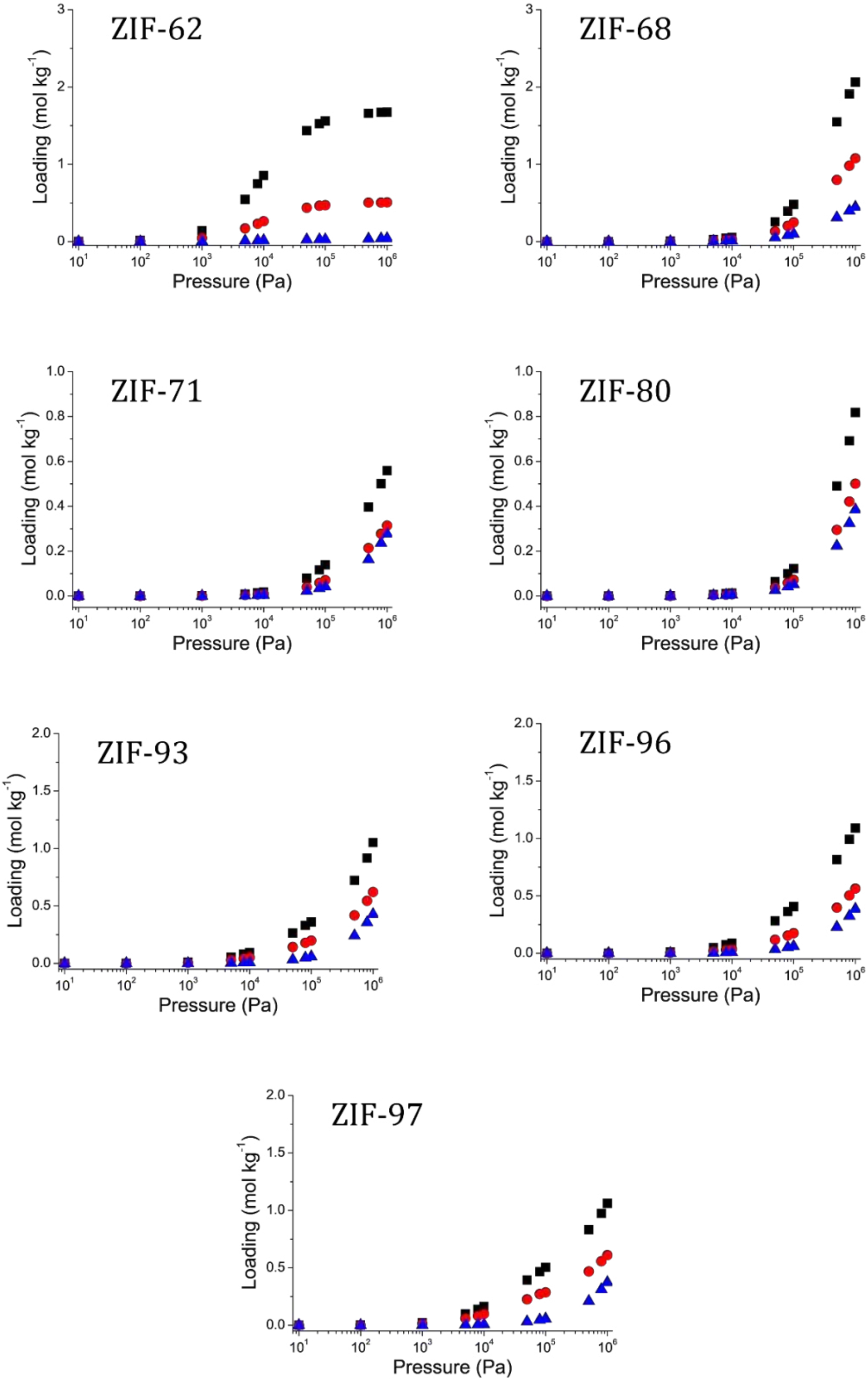

Figure A10. Adsorption isotherms of ethane (black squares) and ethylene (red circles) from the 60:40 binary mixture in several ZIFs at 298 K. Error bars are within the symbol size.

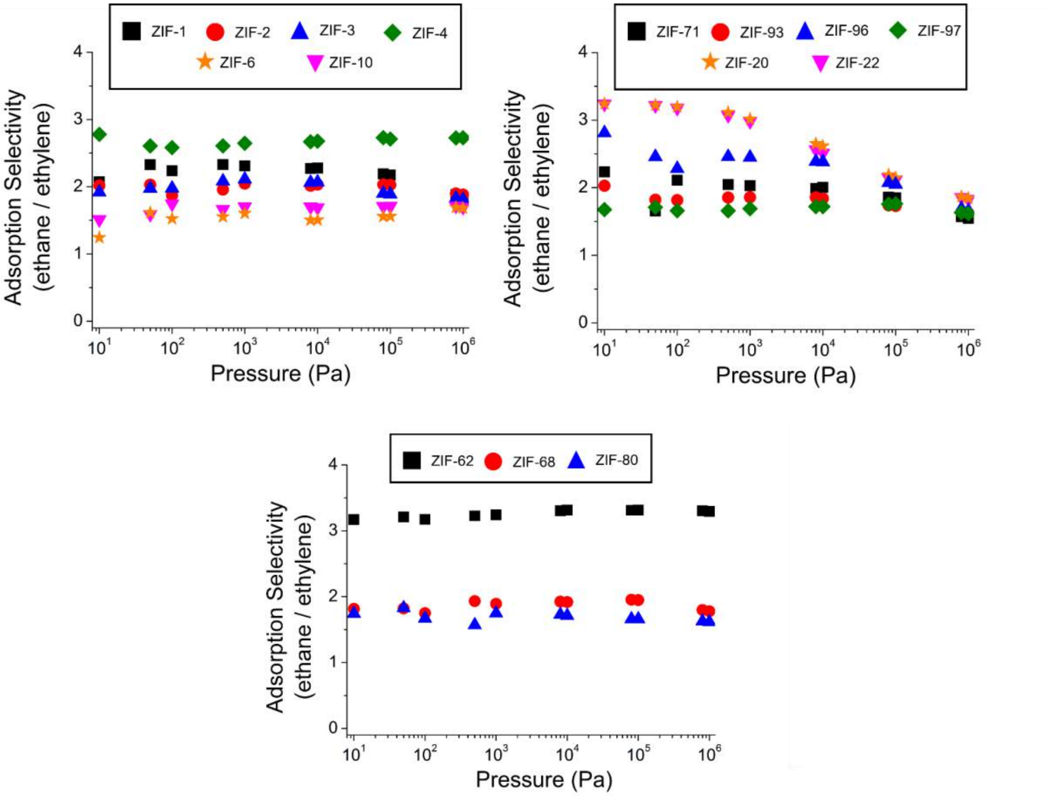

Figure A11. Adsorption selectivity of ethane over ethylene from the 60:40 binary mixture at 298 K. Error bars are within the symbol size.

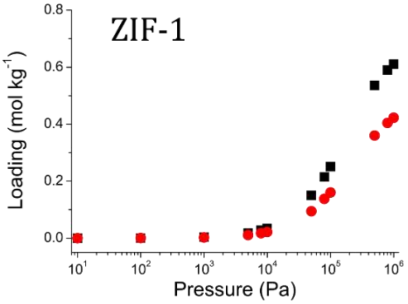
ZIF-1
Loading (mol kg^{-1})
0.8
0.6
0.4
0.2
0.0
10^1
10^2
10^3
10^4
10^5
10^6
Pressure (Pa)

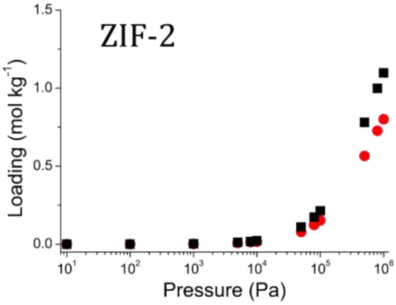
ZIF-2
Loading (mol kg^{-1})
1.5
1.0
0.5
0.0
10^1
10^2
10^3
10^4
10^5
10^6
Pressure (Pa)

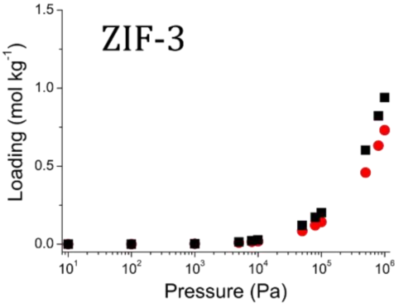
ZIF-3
Loading (mol kg^{-1})
1.5
1.0
0.5
0.0
10^1
10^2
10^3
10^4
10^5
10^6
Pressure (Pa)

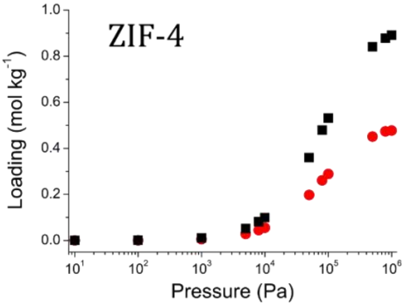
ZIF-4
Loading (mol kg^{-1})
1.0
0.8
0.6
0.4
0.2
0.0
10^1
10^2
10^3
10^4
10^5
10^6
Pressure (Pa)

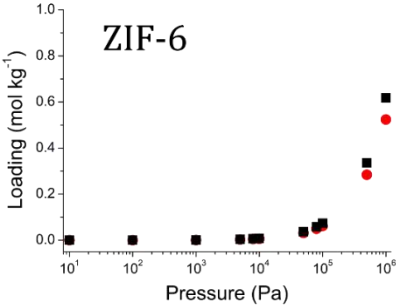
ZIF-6
Loading (mol kg^{-1})
1.0
0.8
0.6
0.4
0.2
0.0
10^1
10^2
10^3
10^4
10^5
10^6
Pressure (Pa)

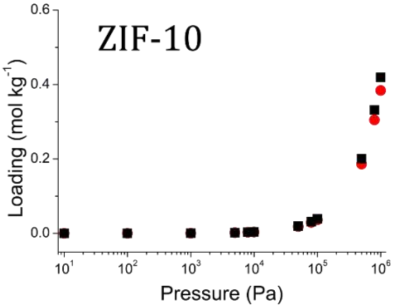
ZIF-10
Loading (mol kg^{-1})
0.6
0.4
0.2
0.0
10^1
10^2
10^3
10^4
10^5
10^6
Pressure (Pa)

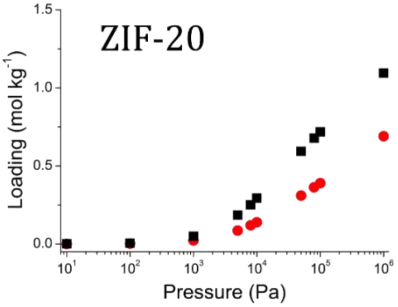
ZIF-20
Loading (mol kg^{-1})
1.5
1.0
0.5
0.0
10^1
10^2
10^3
10^4
10^5
10^6
Pressure (Pa)

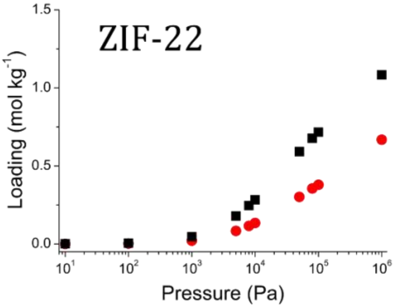
ZIF-22
Loading (mol kg^{-1})
1.5
1.0
0.5
0.0
10^1
10^2
10^3
10^4
10^5
10^6
Pressure (Pa)

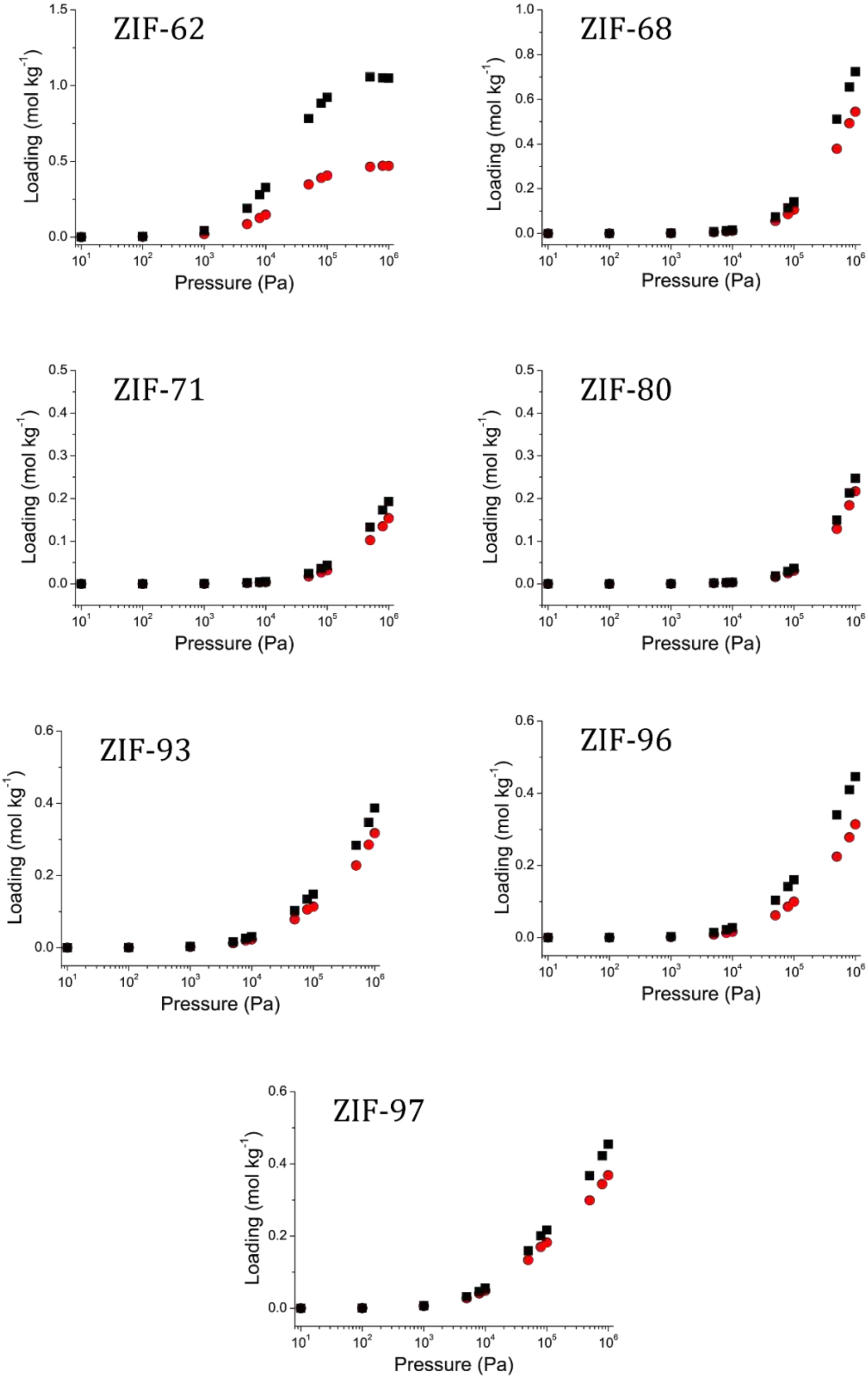

Figure A12. Adsorption isotherms of ethane (black squares) and ethylene (red circles) from the seven-component mixture in several ZIFs at 298 K. Error bars are within the symbol size.

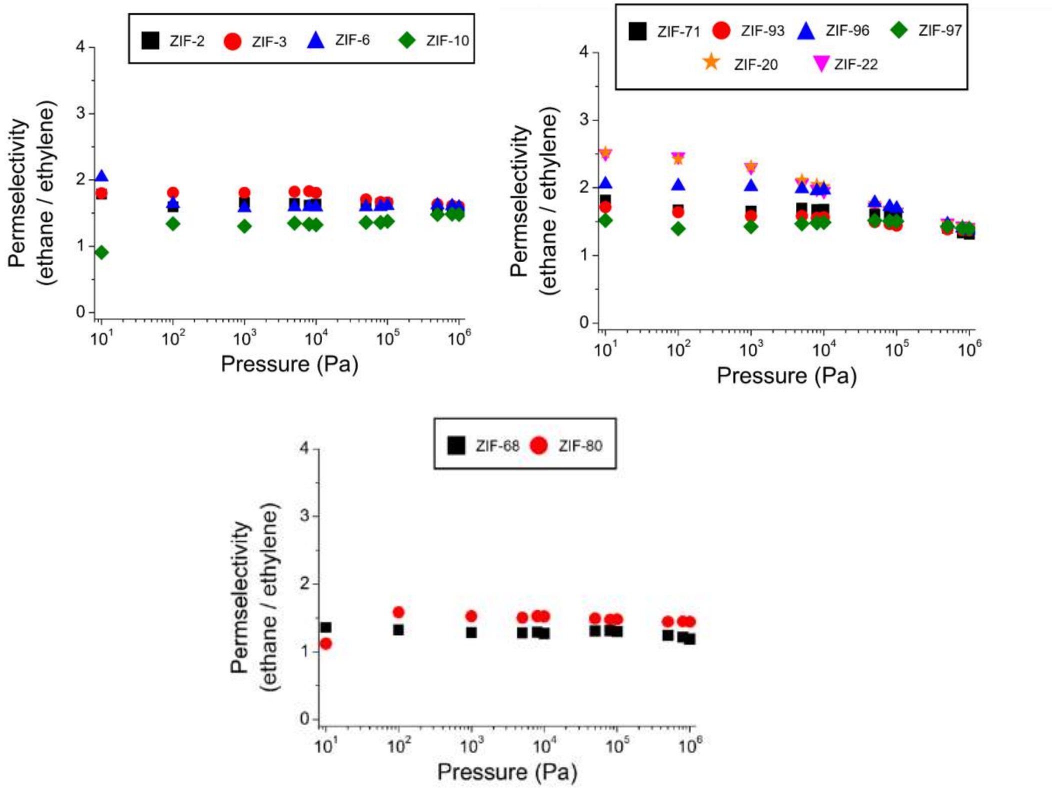

Figure A13. Permselectivity of ethane over ethylene from the 50:50 binary mixture in ZIF-2, -3, -6, -10, -20, -22, -68, -71, -80, -93, -96, and -97 at 298 K. Error bars are within the symbol size.

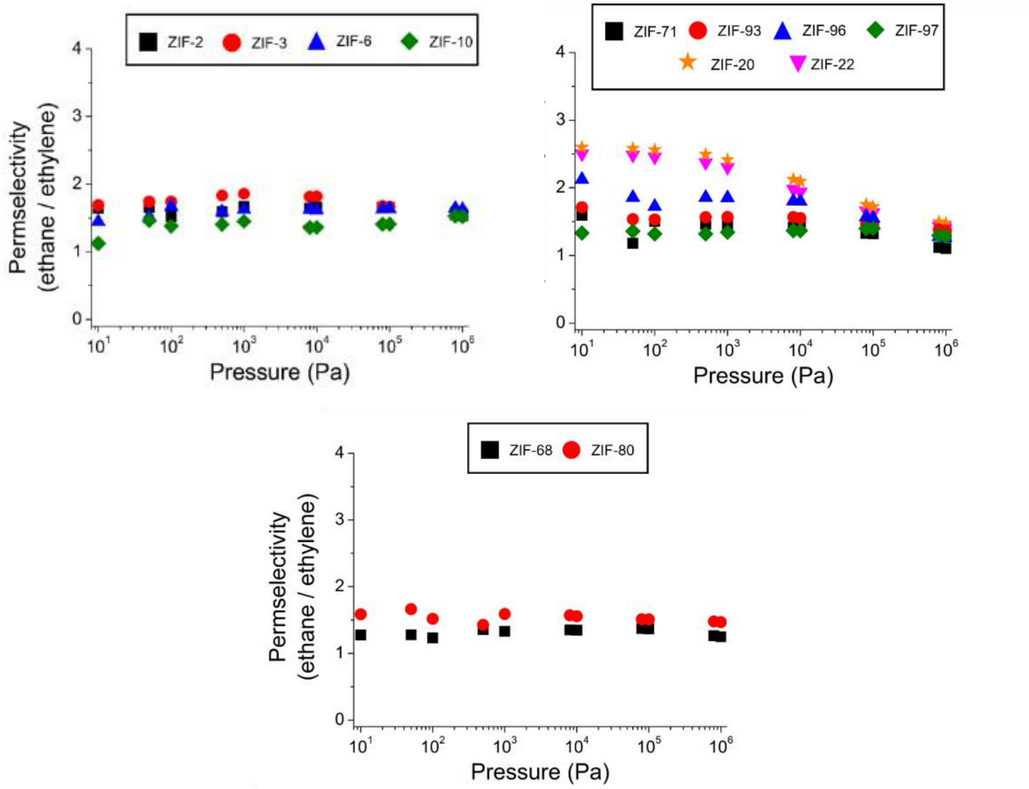

Figure A14. Permselectivity of ethane over ethylene from the 60:40 binary mixture in ZIF-2, -3, -6, -10, -20, -22, -68, -71, -80, -93, -96, and -97 at 298 K. Error bars are within the symbol size.

Table A1. Lennard-Jones parameters and partial charges employed for the adsorbates.

Atom	Charge (e-)	ε/ kB (K)	σ (Å)
	Ethane		
CH_3	-	108	3.76
	Ethylene		
CH_2	-	93	3.685
	Nitrogen		
N	-0.4048	38.298	3.306
Dummy Atom	0.8096	-	-
	Hydrogen		
H	0.4829	36.5	2.82
Dummy Atom	-0.9658	-	-
	Oxygen		
O	-0.112	53.023	3.045
Dummy Atom	0.224	-	-
	Methane		
CH_4	-	158.5	3.72
	Carbon monoxide		
C	-0.2424	16.141	3.636
O	-0.2744	98.014	2.979
Dummy Atom	0.6443	-	-
	Carbon dioxide		
C	0.6512	29.993	2.745
O	-0.3256	85.671	3.017

Table A2. Lennard-Jones parameters and partial charges employed for the adsorbates.

Atom	ε/ kB (K)	σ (Å)
Zn	56.218	2.215
N	31.283	2.935
C	47.604	3.088
H	19.948	2.314
O	27.202	2.806
Cl	102.915	3.165

Table A3. Partial charges of the atoms of the structures employed in this work. The neighbours of the atom are annotated for clarification purposes when needed.

	ZIF-1	ZIF-2	ZIF-3	ZIF-4	ZIF-6	ZIF-8	ZIF-10	ZIF-20
Zn	1	1	1	1	1	1	1	1
N1_$_{\mathrm{CCZn}}$	-0.28	-0.28	-0.28	-0.28	-0.28	-0.2935	-0.28	-0.285
C1_$_{\mathrm{HNN}}$	0.035	0.035	0.035	0.035	0.035	0.126	0.035	0.06
C2_$_{\mathrm{HNC}}$	-0.075	-0.075	-0.075	-0.075	-0.075	-0.074	-0.075	0.02
C3_$_{\mathrm{CHHH}}$						-0.292		-0.075
C4_$_{\mathrm{HNC}}$								-0.12
H1_$_{\mathrm{C1/C3}}$	0.055	0.055	0.055	0.055	0.055	0.0655	0.055	0.06
H2_$_{\mathrm{C2}}$	0.06	0.06	0.06	0.06	0.06	0.09	0.06	0.075

	ZIF-22	ZIF-62	ZIF-68	ZIF-71	ZIF-80	ZIF-93	ZIF-96	ZIF-97
Zn	1	1	1	1	1	1	1	1
N1_$_{\mathrm{CCZn}}$	-0.285	-0.285	-0.285	-0.277	-0.277	-0.2875	-0.2785	-0.2835
N2_$_{\mathrm{CCZn}}$			-0.265		-0.265	-0.285	-0.293	-0.283
N3_$_{\mathrm{CH}}$			0.23		0.23		-0.215	
N4_$_{\mathrm{C}}$							-0.4955	
C1_$_{\mathrm{HNN}}$	0.06	0.06	0.06	-0.062	0.027	0.038	0.0375	0.0035
C2_$_{\mathrm{HNC}}$	0.02	0.02	0.02	0.054	-0.062	-0.349	0.1565	-0.358
C3_$_{\mathrm{CN}}$	-0.075	-0.075	-0.075	0.027	0.054	0.0385	-0.068	0.0215
C4_$_{\mathrm{NNC}}$	-0.12	-0.12	-0.12		0.12	-0.051	0.124	0.005
C5_$_{\mathrm{OH}}$					-0.05	0.1855		-0.0545
H1_$_{\mathrm{C1}}$	0.06	0.06	0.06	0.07	0.07	0.0965	0.0995	0.097
H2_$_{\mathrm{C2}}$	0.075	0.075	0.075		0.075	0.1145	0.2185	0.1105
H3_$_{\mathrm{C2}}$						0.116	0.214	0.11
H4_$_{\mathrm{C5}}$						0.121		0.1025
H5_$_{\mathrm{C5}}$						0.066		0.0835
H6_$_{\mathrm{O}}$								0.1
H7_$_{\mathrm{C5}}$								0.2325
O			-0.185		-0.185	-0.3035		-0.387

Table A4. Pore volume (PV), surface area (SSA), helium void fraction (HVF), simulation box size (SBS), and topology of the ZIFs used in this work.

ZIF	PV (cm^3/g)	SSA (m^2/g)	HVF	SBS ($Å^3$)	Topology
ZIF-1	0.383	1502.377	0.462	29.221 x 30.532 x 29.872	CRB
ZIF-2	0.620	2746.407	0.576	29.037 x 24.114 x 24.450	CRB
ZIF-3	0.647	2997.299	0.570	37.940 x 37.940 x 33.480	DFT
ZIF-4	0.377	1707.724	0.461	30.790 x 30.614 x 36.852	CAG
ZIF-6	0.955	3401.148	0.729	37.030 x 37.030 x 40.490	GIS
ZIF-10	0.961	3385.222	0.717	27.061 x 27.061 x 38.812	MER
ZIF-20	0.500	1767.492	0.508	45.472 x 45.472 x 45.472	LTA
ZIF-22	0.508	1818.192	0.512	45.600 x 45.600 x 45.600	LTA
ZIF-62	0.249	993.722	0.333	31.324 x 31.324 x 36.414	CAG
ZIF-68	0.471	1830.895	0.486	26.641 x 26.641 x 36.976	GME
ZIF-71	0.337	1223.658	0.498	28.553 x 28.553 x 28.553	RHO
ZIF-80	0.405	1571.425	0.502	26.307 x 26.307 x 38.722	GME
ZIF-93	0.450	1591.819	0.446	28.356 x 28.356 x 28.356	RHO
ZIF-96	0.502	1889.748	0.491	28.356 x 28.356 x 28.356	RHO
ZIF-97	0.408	1540.834	0.407	28.432 x 28.432 x 28.432	RHO

Table A5. Henry coefficients (KH), energies, enthalpies, and entropies of adsorption computed for the adsorbates. In parenthesis it is shown the error of the last digit.

Molecule	KH (mol/kg/Pa)	|ΔS| (J/K/mol)	|ΔG| (kJ/mol)	|ΔA| (kJ/mol)	|ΔU| (kJ/mol)	|Qst| (kJ/mol)
			ZIF-1			
Ethane	1.23(1) 10^{-4}	29.35(1)	17.12(1)	14.64(1)	23.39(1)	25.86(1)
Ethylene	5.37(3) 10^{-5}	27.67(2)	15.06(1)	12.58(1)	20.83(2)	23.30(2)
Nitrogen	1.58(1) 10^{-6}	22.78(1)	6.32(1)	3.84(1)	10.63(1)	13.11(1)
			ZIF-2			
Ethane	7.69(1) 10^{-5}	21.54(1)	15.30(1)	12.82(1)	19.24(1)	21.72(1)
Ethylene	3.82(1) 10^{-5}	19.92(1)	13.57(1)	11.09(1)	17.03(1)	19.51(1)
Nitrogen	2.14(1) 10^{-6}	15.73(1)	6.43(1)	3.95(1)	8.64(1)	11.12(1)
			ZIF-3			
Ethane	1.00(1) 10^{-4}	39.84(3)	15.82(1)	13.34(1)	25.22(2)	27.69(2)
Ethylene	4.77(4) 10^{-5}	34.83(7)	13.98(3)	11.51(2)	21.88(5)	24.36(5)
Nitrogen	2.00(1) 10^{-6}	19.86(1)	6.12(1)	3.65(1)	9.57(1)	12.04(1)
			ZIF-4			
Ethane	3.72(2) 10^{-4}	38.76(1)	19.87(1)	17.40(1)	28.95(1)	31.42(1)
Ethylene	1.41(1) 10^{-4}	35.60(2)	17.49(1)	15.01(1)	25.62(1)	28.10(1)
Nitrogen	2.13(1) 10^{-6}	28.07(1)	7.09(1)	4.61(1)	12.98(1)	15.46(1)
			ZIF-6			
Ethane	2.57(1) 10^{-5}	22.24(1)	12.10(1)	9.62(1)	16.25(1)	18.72(1)
Ethylene	1.50(1) 10^{-5}	20.14(2)	10.78(1)	8.30(1)	14.30(2)	16.78(2)
Nitrogen	1.61(1) 10^{-6}	13.32(1)	5.24(1)	2.76(1)	6.73(1)	9.21(1)
			ZIF-10			
Ethane	1.31(1) 10^{-5}	21.60(3)	10.38(1)	7.90(1)	14.34(2)	16.82(2)
Ethylene	8.58(3) 10^{-6}	19.83(1)	9.34(1)	6.86(1)	12.77(1)	15.25(1)
Nitrogen	1.28(1) 10^{-6}	13.15(1)	4.61(1)	2.13(1)	6.05(1)	8.53(1)
			ZIF-20			
Ethane	1.87(1) 10^{-3}	50.05(1)	23.43(1)	20.96(1)	35.87(1)	38.35(1)
Ethylene	5.84(9) 10^{-4}	45.51(9)	20.53(4)	18.06(4)	31.62(6)	34.09(7)
Nitrogen	4.11(2) 10^{-6}	28.59(2)	8.27(1)	5.79(1)	14.31(1)	16.78(1)
			ZIF-22			
Ethane	1.76(1) 10^{-3}	48.61(2)	23.26(1)	20.79(1)	35.27(1)	37.75(1)
Ethylene	5.43(7) 10^{-4}	44.43(2)	20.35(1)	17.88(1)	31.11(2)	33.59(2)
Nitrogen	3.98(1) 10^{-6}	27.94(2)	8.17(1)	5.69(1)	14.02(1)	16.49(1)

ZIF-62						
Ethane	1.52(1) 10^{-3}	38.35(2)	23.59(1)	21.11(1)	32.54(1)	35.02(1)
Ethylene	4.74(4) 10^{-4}	35.33(1)	20.71(1)	18.23(1)	28.76(1)	31.24(1)
Nitrogen	3.62(1) 10^{-6}	28.25(1)	8.63(1)	6.16(1)	14.57(1)	17.05(1)
ZIF-68						
Ethane	5.26(1) 10^{-5}	31.58(2)	14.62(1)	12.15(1)	21.56(2)	24.04(2)
Ethylene	2.77(1) 10^{-5}	29.61(1)	13.02(1)	10.54(1)	19.37(1)	21.84(1)
Nitrogen	1.41(1) 10^{-6}	20.42(1)	5.43(1)	2.95(1)	9.04(1)	11.51(1)
ZIF-71						
Ethane	1.87(1) 10^{-5}	36.05(2)	12.95(1)	10.47(1)	21.21(1)	23.69(1)
Ethylene	9.33(8) 10^{-6}	32.51(6)	11.22(2)	8.74(2)	18.43(3)	20.91(4)
Nitrogen	6.08(1) 10^{-7}	18.97(1)	4.46(1)	1.98(1)	7.63(1)	10.11(1)
ZIF-80						
Ethane	1.34(1) 10^{-5}	33.96(3)	11.68(1)	9.20(1)	19.32(2)	21.80(2)
Ethylene	7.79(3) 10^{-6}	30.71(2)	10.34(1)	7.86(1)	17.01(1)	19.49(1)
Nitrogen	6.82(1) 10^{-7}	17.25(3)	4.30(1)	1.83(1)	6.97(1)	9.45(2)
ZIF-93						
Ethane	1.21(2) 10-4	62.47(6)	16.59(2)	14.11(1)	32.73(3)	35.20(4)
Ethylene	6.54(9) 10-5	57.43(9)	15.02(4)	12.54(3)	29.65(8)	32.13(9)
Nitrogen	1.07(1) 10-6	27.32(1)	4.88(1)	2.41(1)	10.55(1)	13.02(1)
ZIF-96						
Ethane	1.04(1) 10^{-4}	47.13(2)	16.18(1)	13.70(1)	27.75(1)	30.22(2)
Ethylene	4.22(2) 10^{-5}	42.48(2)	13.94(1)	11.46(1)	24.12(1)	26.60(2)
Nitrogen	1.12(1) 10^{-6}	21.91(3)	4.96(1)	2.48(1)	9.01(1)	11.49(2)
ZIF-97						
Ethane	2.46(2) 10^{-4}	64.20(9)	18.36(3)	15.89(2)	35.02(5)	37.50(5)
Ethylene	1.48(2) 10^{-4}	60.21(9)	17.13(3)	14.66(2)	32.60(6)	35.08(6)
Nitrogen	1.37(1) 10^{-6}	33.72(5)	5.51(1)	3.03(1)	13.08(2)	15.56(2)

Table A6. Self-diffusion coefficients of ethane and ethylene from the 50:50 (left) and the 60:40 (right) binary mixture in ZIF-2, -3, -6, -10, -20, -22, -68, -71, -80, -93, -96, and -97 at 106 Pa and 298 K. In parenthesis it is shown the error of the last digit.

	Ethane	Ethylene
Structure	D 10^{-8} (m^{2} s^{-1})	D 10^{-8} (m^{2} s^{-1})
ZIF-1	-	-
ZIF-2	4.45(2) x 10^{-2}	5.49(1) x 10^{-2}
ZIF-3	7.03(1) x 10^{-2}	8.00(1) x 10^{-2}
ZIF-4	-	-
ZIF-6	2.27(2) x 10^{-1}	2.43(2) x 10^{-1}
ZIF-10	1.54(1) x 10^{-1}	1.76(1) x 10^{-1}
ZIF-20	5.58(9) x 10^{-2}	7.29(8) x 10^{-2}
ZIF-22	5.21(9) x 10^{-2}	6.81(9) x 10^{-2}
ZIF-62	-	-
ZIF-68	5.51(1) x 10^{-2}	8.24(7) x 10^{-2}
ZIF-71	6.68(1) x 10^{-2}	7.92(1) x 10^{-2}
ZIF-80	1.48(1) x 10^{-1}	1.67(2) x 10^{-1}
ZIF-93	1.50(9) x 10^{-1}	1.78(9) x 10^{-1}
ZIF-96	1.53(1) x 10^{-1}	1.87(1) x 10^{-1}

	Ethane	Ethylene
Structure	D 10^{-8} (m^{2} s^{-1})	D 10^{-8} (m^{2} s^{-1})
ZIF-1	-	-
ZIF-2	4.25(1) x 10^{-2}	5.22(1) x 10^{-2}
ZIF-3	6.88(1) x 10^{-2}	7.82(1) x 10^{-2}
ZIF-4	-	-
ZIF-6	2.47(1) x 10^{-1}	2.58(1) x 10^{-1}
ZIF-10	1.52(1) x 10^{-1}	1.68(1) x 10^{-1}
ZIF-20	5.50(1) x 10^{-2}	7.12(1) x 10^{-2}
ZIF-22	5.02(1) x 10^{-2}	6.27(1) x 10^{-2}
ZIF-62	-	-
ZIF-68	6.23(1) x 10^{-2}	8.87(1) x 10^{-2}
ZIF-71	8.11(1) x 10^{-2}	1.14(1) x 10^{-1}
ZIF-80	1.61(1) x 10^{-1}	1.77(1) x 10^{-1}
ZIF-93	1.24(1) x 10^{-1}	1.48(1) x 10^{-1}
ZIF-96	1.52(1) x 10^{-1}	2.01(1) x 10^{-1}

Table A7. Self-diffusion coefficients of ethane, ethylene, and nitrogen from the ternary 10:10:80 mixture in ZIF-2, -3, -6, -10, -20, -22, -68, -71, -80, -93, -96, and -97at 106 Pa and 298 K. In parenthesis it is shown the error of the last digit.

	Ethane	Ethylene	Nitrogen
Structure	D 10^{-8} (m^2 s^{-1})	D 10^{-8} (m^2 s^{-1})	D 10^{-8} (m^2 s^{-1})
ZIF-1	-	-	-
ZIF-2	1.12(1) x 10^{-1}	1.24(2) x 10^{-1}	1.16(5) x 10^{-1}
ZIF-3	1.33(1) x 10^{-1}	1.54(2) x 10^{-1}	2.94(3) x 10^{-1}
ZIF-4	-	-	-
ZIF-6	4.29(1) x 10^{-1}	4.70(1) x 10^{-1}	7.38(1) x 10^{-1}
ZIF-10	2.68(5) x 10^{-1}	3.33(4) x 10^{-1}	5.06(1) x 10^{-1}
ZIF-20	5.73(8) x 10^{-2}	7.41(9) x 10^{-2}	2.10(9) x 10^{-1}
ZIF-22	5.78(6) x 10^{-2}	7.06(9) x 10^{-2}	2.28(9) x 10^{-1}
ZIF-62	-	-	-
ZIF-68	6.67(6) x 10^{-2}	7.70(1) x 10^{-2}	2.34(2) x 10^{-1}
ZIF-71	9.07(1) x 10^{-2}	1.14(1) x 10^{-1}	4.69(2) x 10^{-1}
ZIF-80	1.09(1) x 10^{-1}	1.09(1) x 10^{-1}	5.62(1) x 10^{-1}
ZIF-93	7.55(7) x 10^{-2}	1.09(9) x 10^{-1}	3.69(2) x 10^{-1}
ZIF-96	1.28(1) x 10^{-1}	1.88(1) x 10^{-1}	5.05(2) x 10^{-1}

Table A8. Self-diffusion coefficients of ethane oxygen, methane, carbon monoxide, carbon dioxide, ethane, and ethylene from the seven component mixtures in ZIF-2, -3, -6, -10, -20, -22, -68, -71, -80, -93, -96, and -97 at 106 Pa and 298 K. In parenthesis it is shown the error of the last digit.

	Hydrogen	Oxygen	Methane	Carbon monoxide	Carbon dioxide	Ethylene	Ethane
Structure	D 10^{-8} (m^2 s^{-1})	D 10^{-8} (m^2 s^{-1})	D 10^{-8} (m^2 s^{-1})	D 10^{-8} (m^2 s^{-1})	D 10^{-8} (m^2 s^{-1})	D 10^{-8} (m^2 s^{-1})	D 10^{-8} (m^2 s^{-1})
ZIF-1	-	-	-	-	-	-	-
ZIF-2	5.07(2) x 10^{-1}	2.13(9) x 10^{-1}	1.99(4) x 10^{-1}	1.44(3) x 10^{-1}	3.24(2) x 10^{-1}	1.66(1) x 10^{-1}	1.39(2) x 10^{-1}
ZIF-3	7.84(3) x 10^{-1}	9.45(9) x 10^{-2}	3.36(1) x 10^{-1}	1.31(6) x 10^{-1}	3.68(3) x 10^{-1}	1.93(2) x 10^{-1}	1.61(3) x 10^{-1}
ZIF-4	-	-	-	-	-	-	-
ZIF-6	1.85(1) x 10^{0}	5.75(2) x 10^{-1}	7.98(1) x 10^{-1}	3.89(2) x 10^{-1}	9.26(6) x 10^{-1}	4.69(1) x 10^{-1}	4.21(1) x 10^{-1}
ZIF-10	1.22(8) x 10-0	6.16(1) x 10^{-1}	4.78(2) x 10^{-1}	4.25(2) x 10^{-1}	9.77(9) x 10^{-1}	3.55(1) x 10^{-1}	2.67(9) x 10^{-1}
ZIF-20	1.73(9) x 10^{-2}	9.13(9) x 10^{-3}	2.38(9) x 10^{-2}	2.59(9) x 10^{-2}	1.07(1) x 10^{-1}	7.69(9) x 10^{-2}	4.41(9) x 10^{-2}
ZIF-22	1.60(9) x 10^{-2}	1.08(9) x 10^{-2}	2.95(9) x 10^{-2}	2.71(9) x 10^{-2}	1.20(1) x 10^{-1}	8.86(9) x 10^{-2}	4.16(8) x 10^{-2}
ZIF-62	-	-	-	-	-	-	-
ZIF-68	3.72(1) x 10^{-2}	1.16(4) x 10^{-1}	1.48(8) x 10^{-1}	9.46(4) x 10^{-2}	1.17(2) x 10^{-1}	7.66(4) x 10^{-2}	5.97(3) x 10^{-2}
ZIF-71	3.64(9) x 10^{-0}	6.32(9) x 10^{-1}	3.50(2) x 10^{-1}	2.40(2) x 10^{-1}	9.12(9) x 10^{-1}	1.39(5) x 10^{-1}	1.44(6) x 10^{-1}
ZIF-80	1.75(9) x 10^{-0}	5.47(1) x 10^{-1}	3.76(1) x 10^{-1}	2.50(9) x 10^{-1}	9.00(9) x 10^{-1}	1.91(5) x 10^{-1}	1.76(2) x 10^{-1}
ZIF-93	3.73(4) x 10^{-1}	1.39(9) x 10^{-2}	2.24(5) x 10^{-1}	1.09(3) x 10^{-1}	2.42(2) x 10^{-1}	1.06(9) x 10^{-1}	7.90(9) x 10^{-2}
ZIF-96	1.43(7) x 10^{-0}	2.64(2) x 10^{-1}	4.48(9) x 10^{-1}	2.36(9) x 10^{-1}	2.52(7) x 10^{-1}	1.60(8) x 10^{-1}	1.35(4) x 10^{-1}

(1) Bux, H.; Chmelik, C.; Krishna, R.; Caro, J. *Journal of Membrane Science* **2011**, *369*, 284.

(2) Böhme, U.; Barth, B.; Paula, C.; Kuhnt, A.; Schwieger, W.; Mundstock, A.; Caro, J.; Hartmann, M. *Langmuir* **2013**, *29*, 8592.

List of publications

The following publications are directly related with this Thesis

Peer reviewed journals

- **F.D. Lahoz-Martín**, A. Martín-Calvo, J.J. Gutiérrez-Sevillano, and S. Calero. "Effect of Light Gases in the Ethane/Ethylene Separation Using Zeolitic Imidazolate Frameworks", *The Journal of Physical Chemistry C*, 2018, 122 (15), 8637-8646.
- **F.D. Lahoz-Martín**, S. Calero, J.J. Gutiérrez-Sevillano, and A. Martín-Calvo. "Adsorptive Separation of Ethane and Ethylene using IsoReticular Metal-Organic Frameworks", *Microporous and Mesoporous Materials*, 2017, 248, 40-45.
- **F. D. Lahoz-Martín**, A. Martin-Calvo and S. Calero. "Selective Separation of BTEX Mixtures Using Metal-Organic Frameworks", *Journal of Physical Chemistry C*, 2014, (24), 13126-13136.
- A. Martín-Calvo, **F. D. Lahoz-Martín** and S. Calero. "Understanding Carbon Monoxide Capture Using Metal-Organic Frameworks". *Journal of Physical Chemistry C*, 2012, 116 (11), 6655-6663.

Non-peer reviewed journals

- **F. D. Lahoz-Martín**. "MOFs use in drug separation", MoleQla: Revista de Ciencias de la Universidad Pablo de Olavide, ISSN-e 2173-0903, nº 9, 2013, págs. 89-90.

Appendix 3

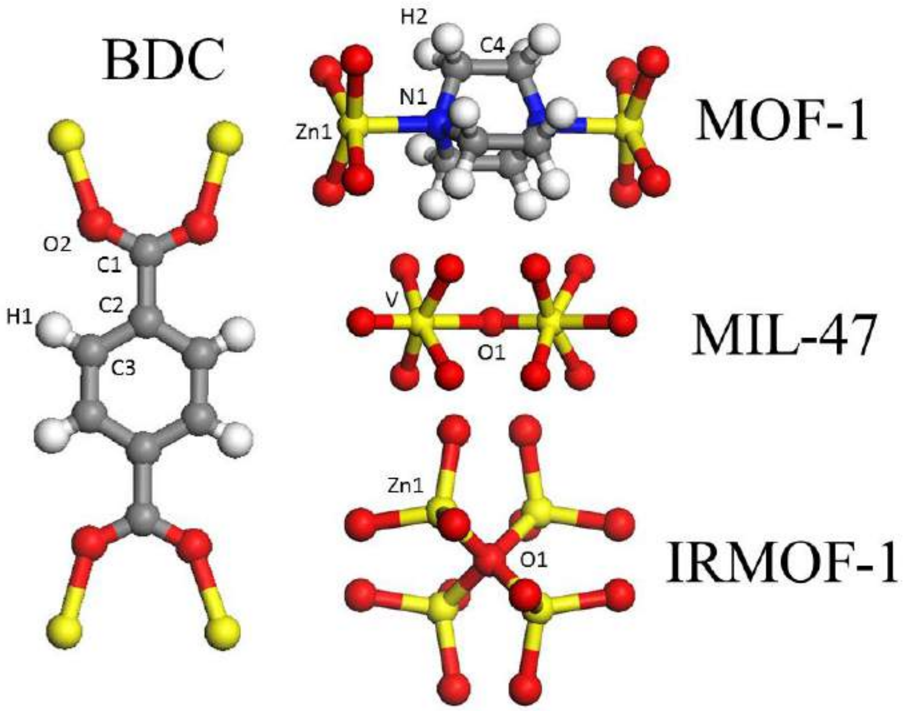

Figure A1. Labels of the different crystallographic atoms in the linker molecules and the metallic centres of MOF-1, MIL-47, and IRMOF-1.

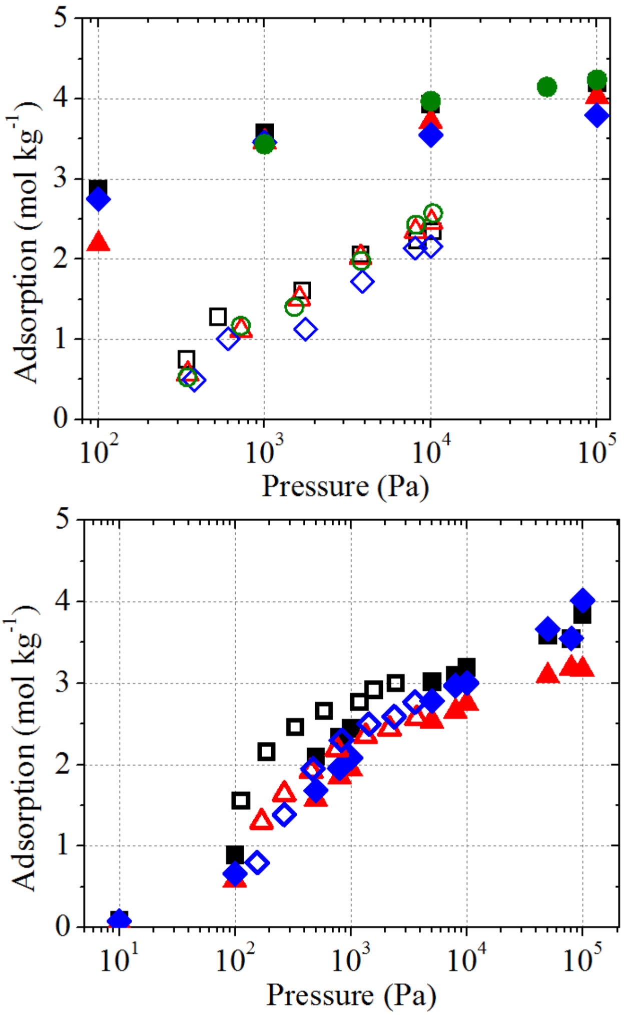

Figure A2. Pure component adsorption isotherms of ortho- (squares), meta- (triangles), and para-xylene (diamonds), in (a) MOF-1 at 448 K and (b) MIL-47 at 423 K. Simulation results (full symbols) are compared with experimental data (empty symbols) from Barcia *et al.*[1] and Finsy *et al.*[2], respectively.

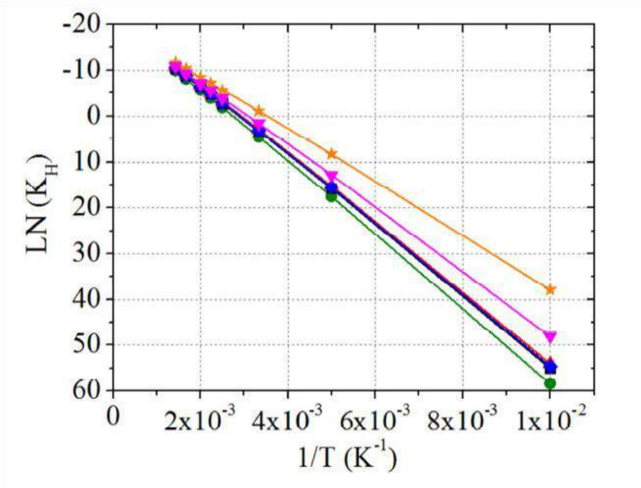

Figure A3. Computed Henry coefficients at different temperatures in MIL-47. Ortho-xylene (black squares), meta-xylene (red up-triangles), para-xylene (blue diamonds), ethylbenzene (green circles), benzene (orange stars), and toluene (pink down-triangles). Error bars are within the symbol size.

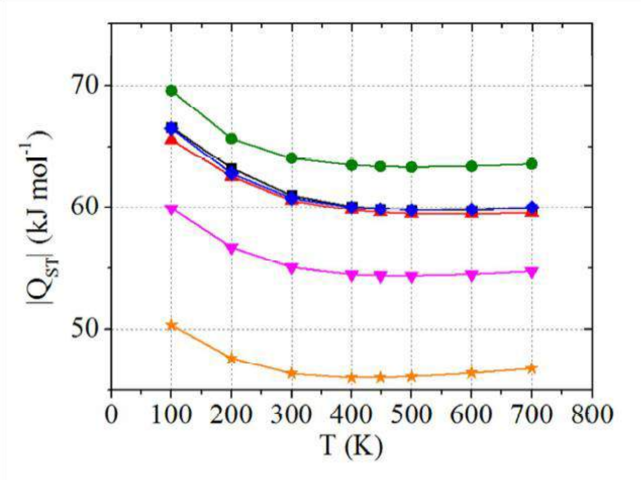

Figure A4. Computed isosteric heats of adsorption at different temperatures in MIL-47. Ortho-xylene (black squares), meta-xylene (red up-triangles), para-xylene (blue diamonds), ethylbenzene (green circles), benzene (orange stars), and toluene (pink down-triangles). Error bars are within the symbol size.

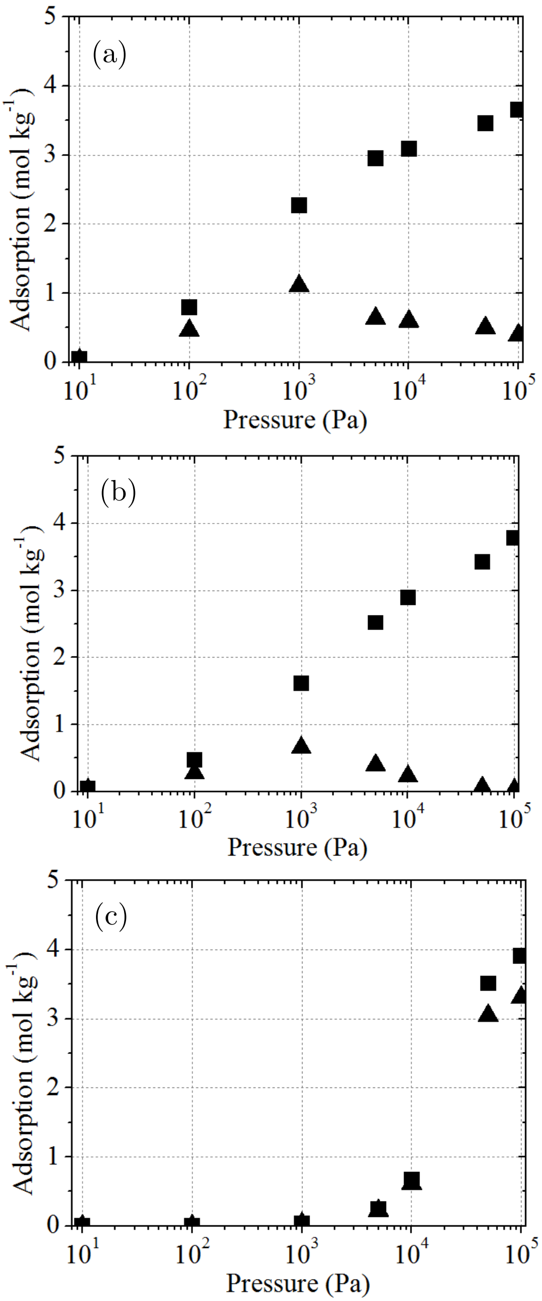

Figure A5. Computed adsorption isotherms of the binary equimolar mixture of ortho- / meta-xylene in (a) MOF-1, (b) MIL-47, and (c) IRMOF-1 at 448 K. Ortho-xylene (squares) and meta-xylene (triangles).

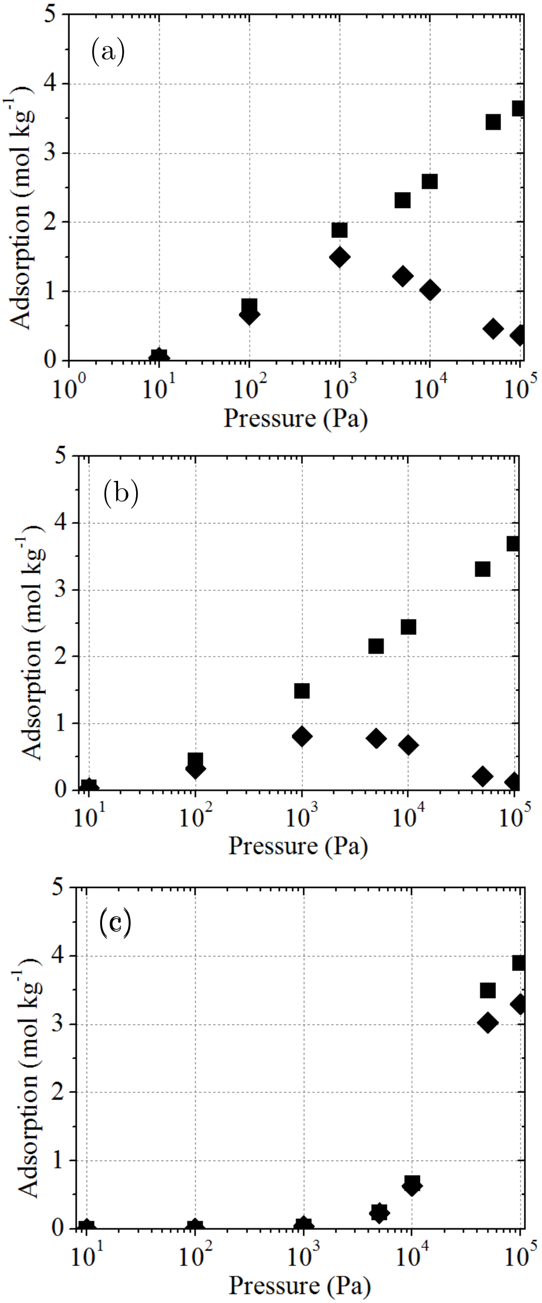

Figure A6. Computed adsorption isotherms of the binary equimolar mixture of ortho- / para-xylene in (a) MOF-1, (b) MIL-47, and (c) IRMOF-1 at 448 K. Ortho-xylene (squares) and para-xylene (diamonds).

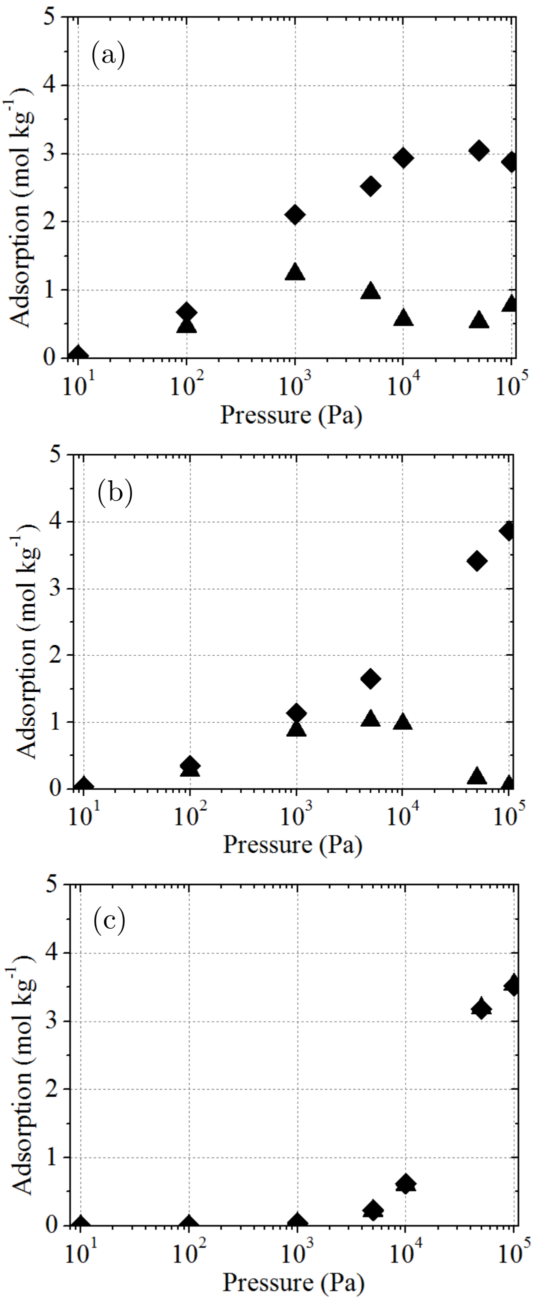

Figure A7. Computed adsorption isotherms of the binary equimolar mixture of meta- / para-xylene in (a) MOF-1, (b) MIL-47, and (c) IRMOF-1 at 448 K. Meta-xylene (triangles) and para-xylene (diamonds).

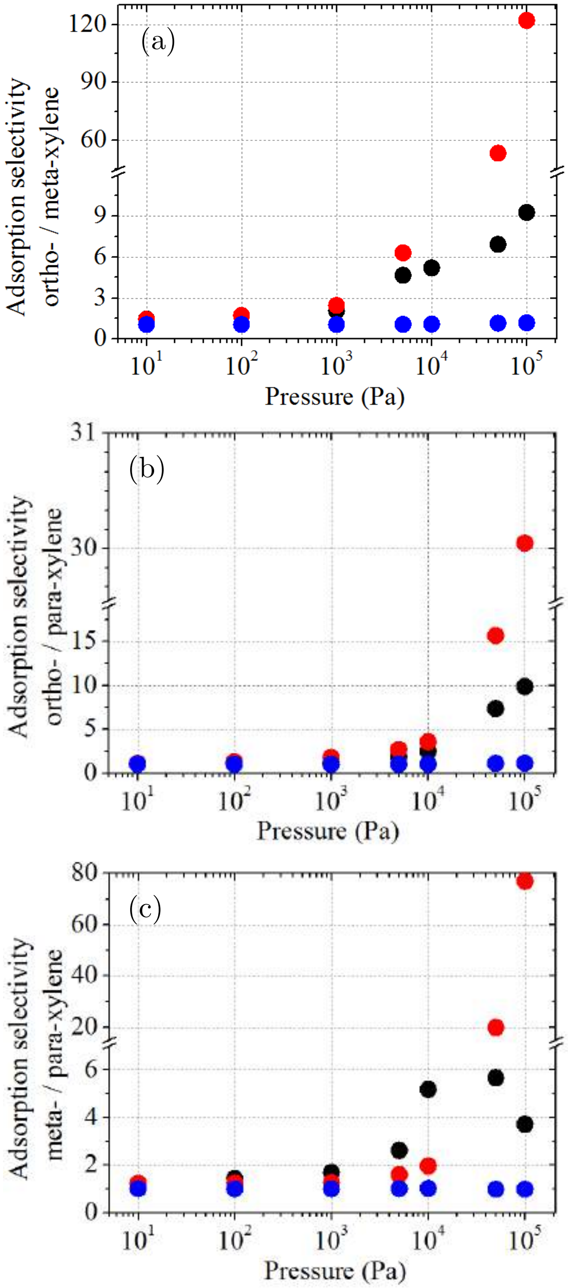

Figure A8. Adsorption selectivity of (a) ortho- / meta-xylene, (b) ortho- / para-xylene, and (c) para- / meta-xylene obtained from the equimolar binary mixture in MOF-1 (black), MIL-47 (red), and IRMOF-1 (blue) at 448 K.

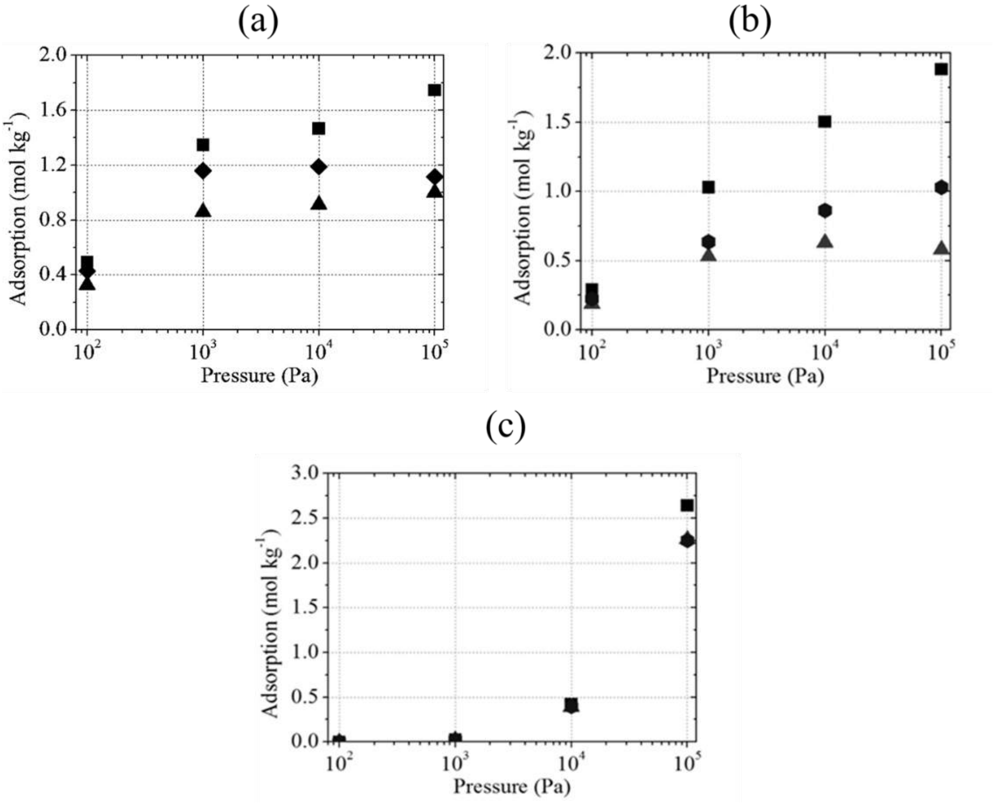

Figure A9. Computed adsorption isotherms for the equimolar trnary mixture (ortho- / meta- / para-xylene) in (a) MOF-1, (b) MIL-47, and (c) IRMOF-1 at 448 K. Ortho-xylene in squares, meta-xylene in triangles, and para-xylene in diamonds.

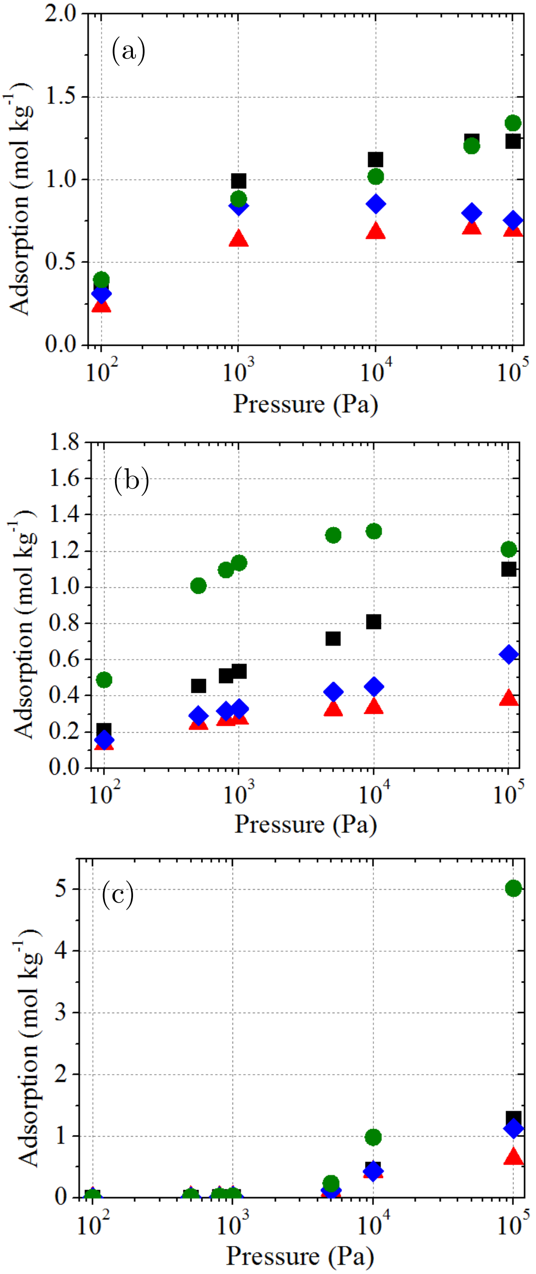

Figure A10. Computed adsorption isotherms for the equimolar quaternary mixture (ortho- / meta- / para-xylene / ethylbenzene) in (a) MOF-1, (b) MIL-47, and (c) IRMOF-1 at 448 K. Ortho-xylene in black squares, meta-xylene in red triangles, para-xylene in blue diamonds, and ethylbenzene in green circles.

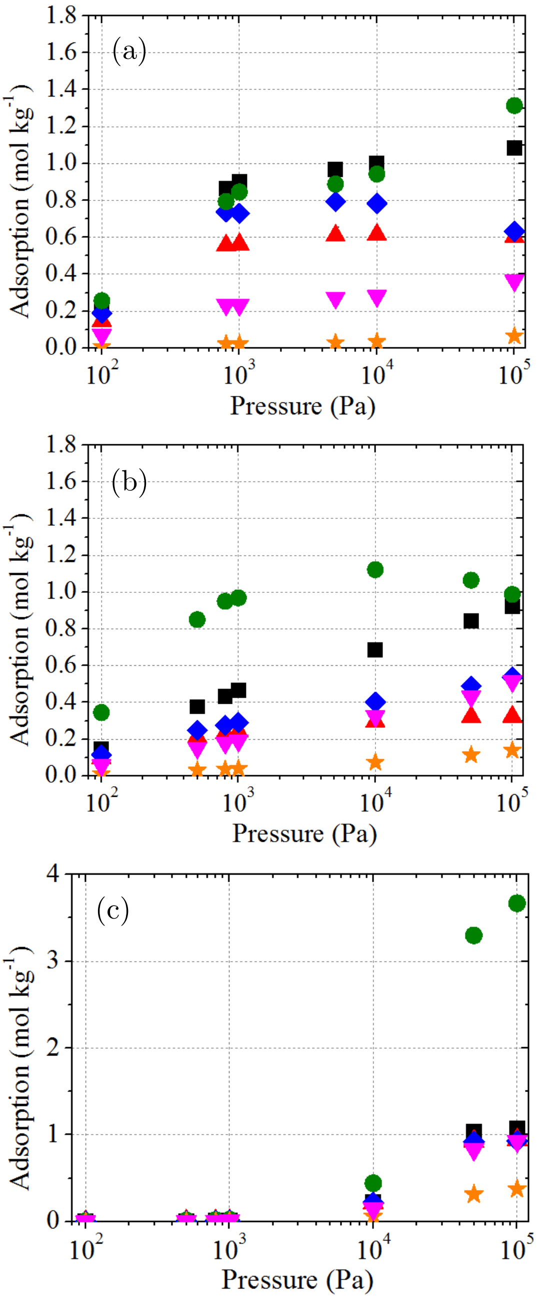

Figure A11. Computed adsorption isotherms for the six-component equimolar mixture (ortho- / meta- / para-xylene / ethylbenzene / benzene / toluene) in (a) MOF-1, (b) MIL-47, and (c) IRMOF-1 at 448 K. Ortho-xylene in black squares, meta-xylene in red up-triangles, para-xylene in blue diamonds, ethylbenzene in green circles, benzene in orange stars, and toluene in pink down-triangles.

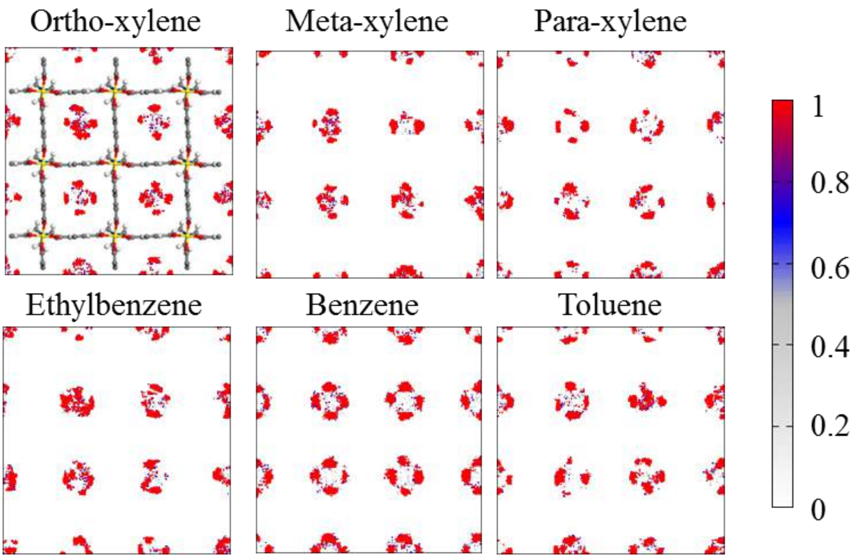

Figure A12. Average occupation profiles of ortho-, meta-, para-xylene, ethylbenzene, benzene, and toluene, from the pure adsorption isotherms adsorbed in MOF-1, at 448 K and 100 kPa. The color gradation is related to the occupation density. For an easier understanding of the location of the molecules, a representation of the structure has been added to one of the plots.

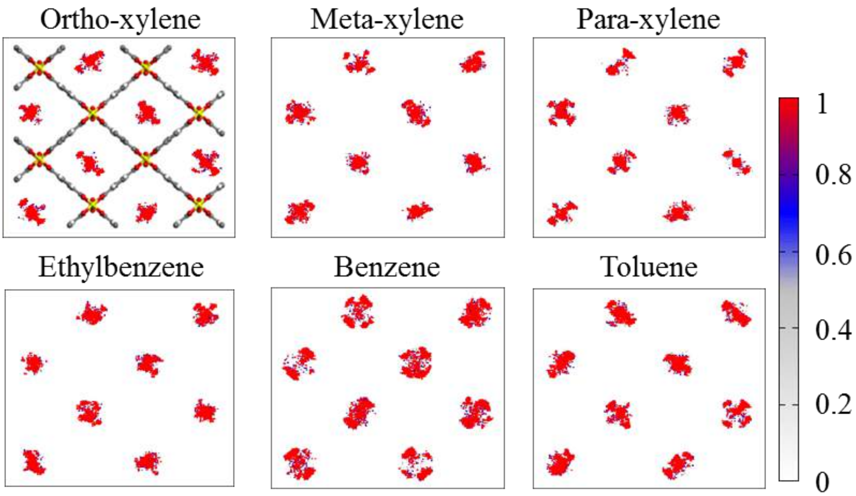

Figure A13. Average occupation profiles of ortho-, meta-, para-xylene, ethylbenzene, benzene, and toluene, from the pure adsorption isotherms adsorbed in MIL-47, at 448 K and 100 kPa. The color gradation is related to the occupation density. For an easier understanding of the location of the molecules, a representation of the structure has been added to one of the plots.

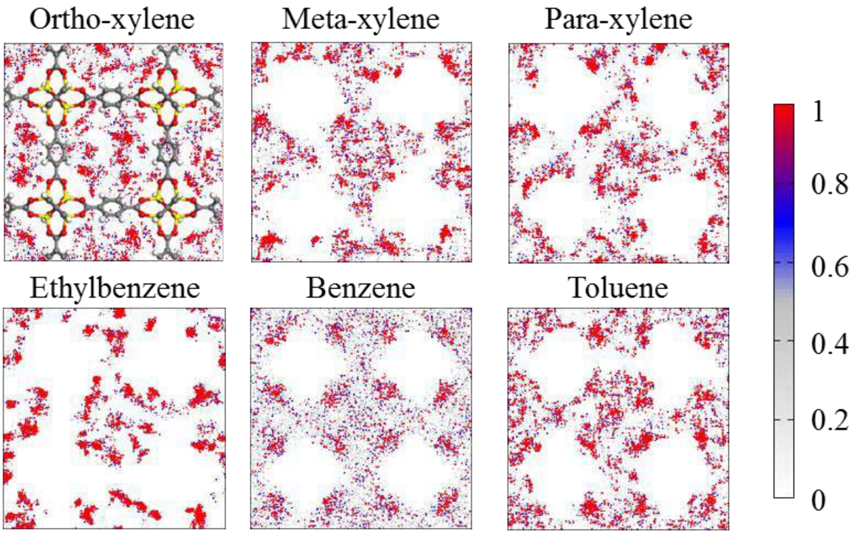

Figure A14. Average occupation profiles of ortho-, meta-, para-xylene, ethylbenzene, benzene, and toluene, from the pure adsorption isotherms adsorbed in IRMOF-1, at 448 K and 100 kPa. The color gradation is related to the occupation density. For an easier understanding of the location of the molecules, a representation of the structure has been added to one of the plots.

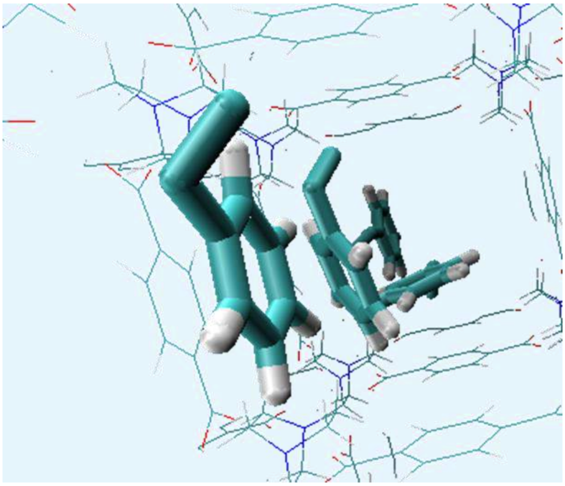

Figure A15. Distribution of ethylbenzene molecules inside MOF-1 at 10^5 Pa and 448 K. Image obtained from the six-component mixture adsorption isotherm data.

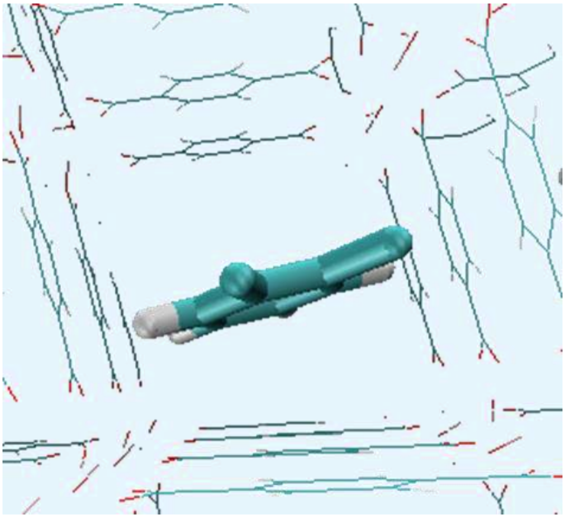

Figure A16. Distribution of ortho-xylene molecules inside the channels of MIL-47 at 10^5 Pa and 448 K. Image obtained from the six-component mixture adsorption isotherm data.

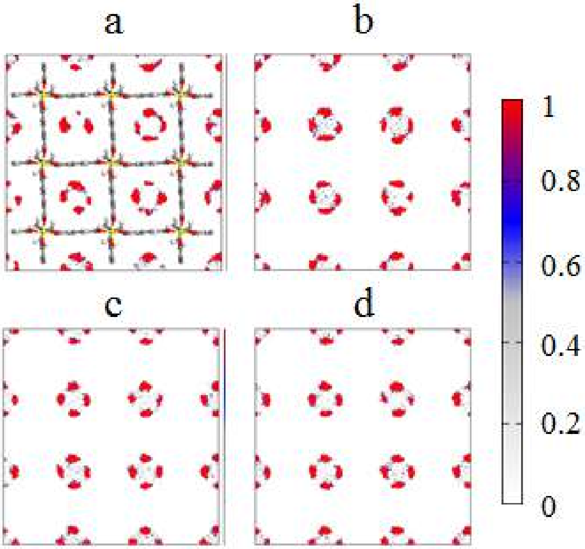

Figure A17. Average occupation profiles of the different models of ethylbenzene: (a) full atom model, (b) mixed model; and toluene: (c) full atom and (d) mixed model from the pure adsorption isotherms in MOF-1, at 448 K and at 100 kPa. The color gradation is related to the occupation density. For an easier understanding of the location of the molecules, a representation of the structure has been added to one of the plots.

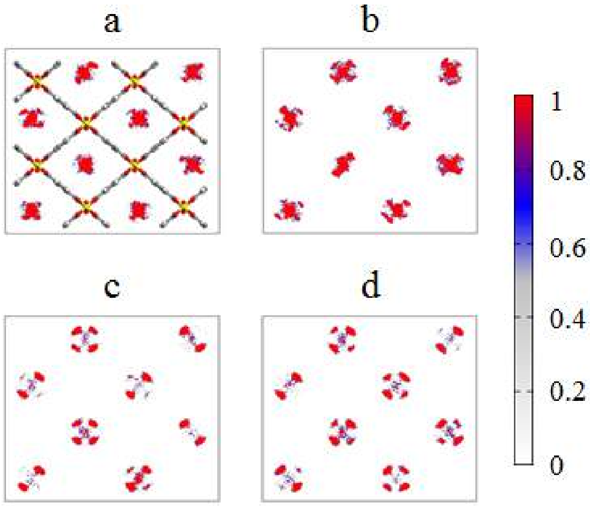

Figure A18. Average occupation profiles of the different models of ethylbenzene: (a) full atom model, (b) mixed model; and toluene: (c) full atom and (d) mixed model from the pure adsorption isotherms in MIL-47, at 448 K and at 100 kPa. The color gradation is related to the occupation density. For an easier understanding of the location of the molecules, a representation of the structure has been added to one of the plots.

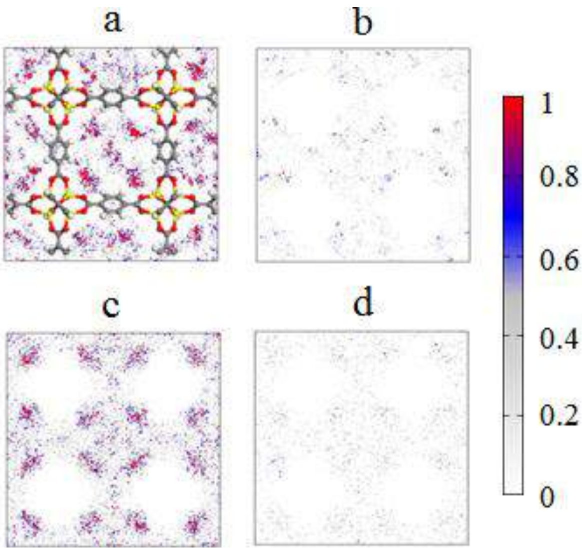

Figure A19. Average occupation profiles of the different models of ethylbenzene: (a) full atom model, (b) mixed model; and toluene: (c) full atom and (d) mixed model from the pure adsorption isotherms in IRMOF-1, at 448 K and at 100 kPa. The color gradation is related to the occupation density. For an easier understanding of the location of the molecules, a representation of the structure has been added to one of the plots.

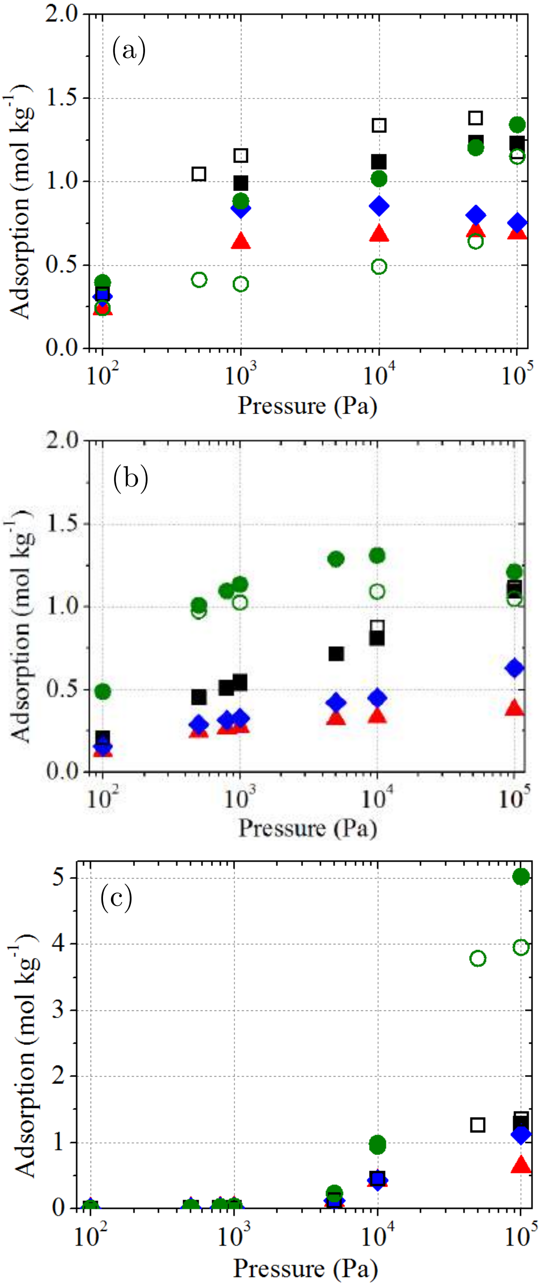

Figure A20. Computed adsorption isotherms for the equimolar quaternary mixture (ortho- / meta- / para-xylene / ethylbenzene) in (a) MOF-1, (b) MIL-47, and (c) IRMOF-1 at 448 K using different molecular models: original mixed models (full symbols) and full atom model of ethylbenzene (empty symbols). Ortho-xylene in black squares, meta-xylene in red triangles, para-xylene in blue diamonds, and ethylbenzene in green circles.

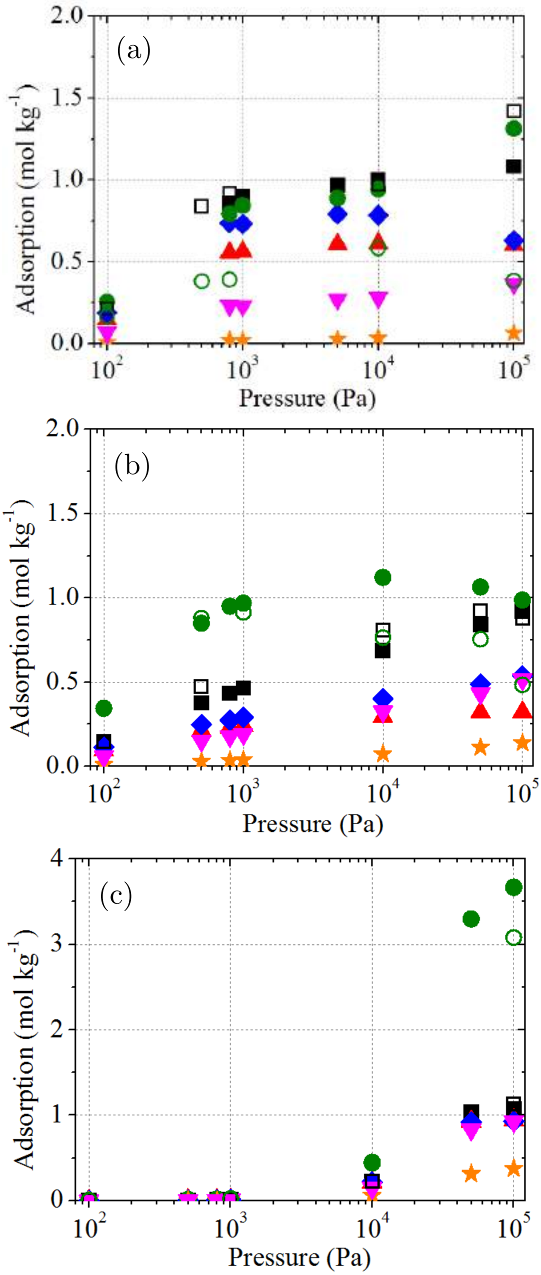

Figure A21. Computed adsorption isotherms for the equimolar six-component mixture (ortho- / meta- / para-xylene / ethylbenzene / benzene / toluene) in (a) MOF-1, (b) MIL-47, and (c) IRMOF-1 at 448 K using different molecular models: original mixed models (full symbols) and full atom models of ethylbenzene and toluene (empty symbols). Ortho-xylene in black squares, meta-xylene in red up-triangles, para-xylene in blue diamonds, ethylbenzene in green circles, benzene in orange stars, and toluene in pink down-triangles.

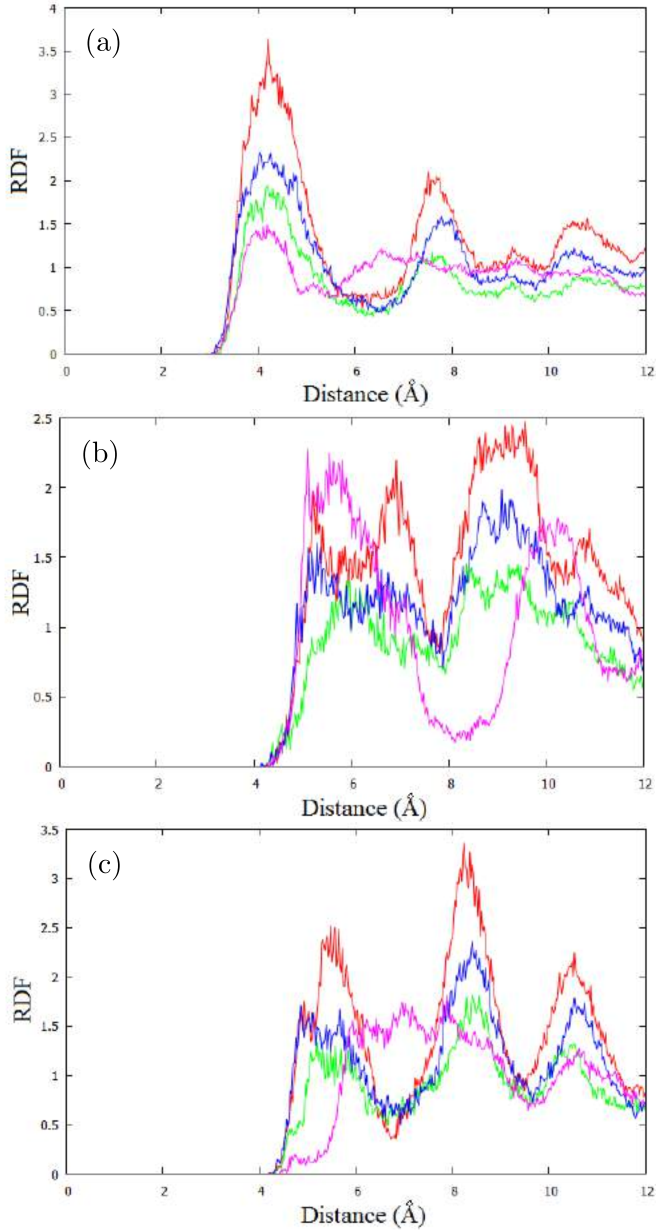

Figure A22. Computed radial distribution functions in MOF-1 of the CH3 group of the adsorbates referring to (a) the C3 atom of the benzene group of the linker, (b) the N atom of Dabco group, and (c) the Zn atom of the metallic center at 100 kPa and 448 K using a full atom model for ethylbenzene and toluene. Color lines represent the variation of the probability with the distance for each molecule: ortho- (red), meta- (green), para-xylene (blue), and ethylbenzene (pink).

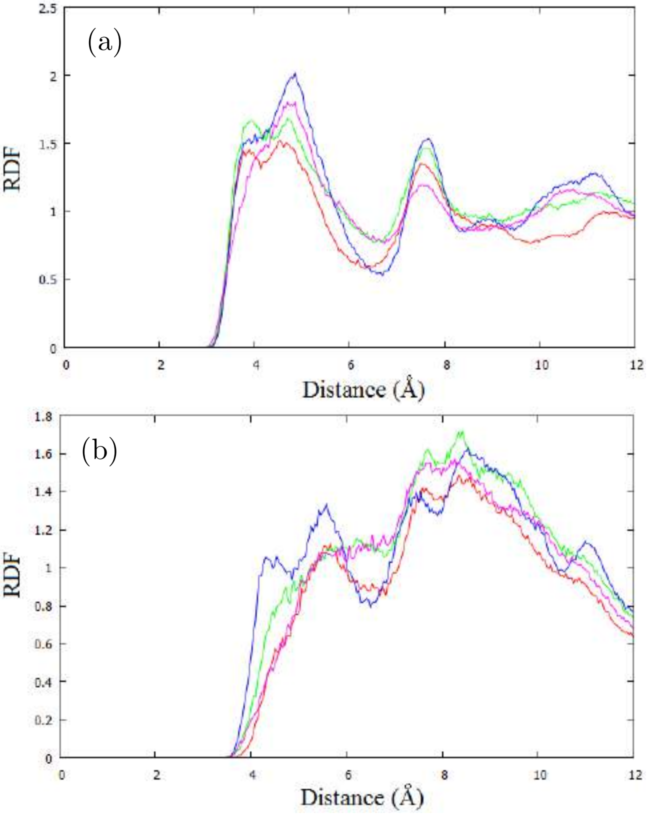

Figure A23. Computed radial distribution functions in MIL-47 of the CH3 group of the adsorbates referring to (a) the C3 atom of the benzene group of the linker, and (b) the V atom of the metallic center at 100 kPa and 448 K using a full atom model for ethylbenzene and toluene. Color lines represent the variation of the probability with the distance for each molecule: ortho- (red), meta- (green), para-xylene (blue), and ethylbenzene (pink).

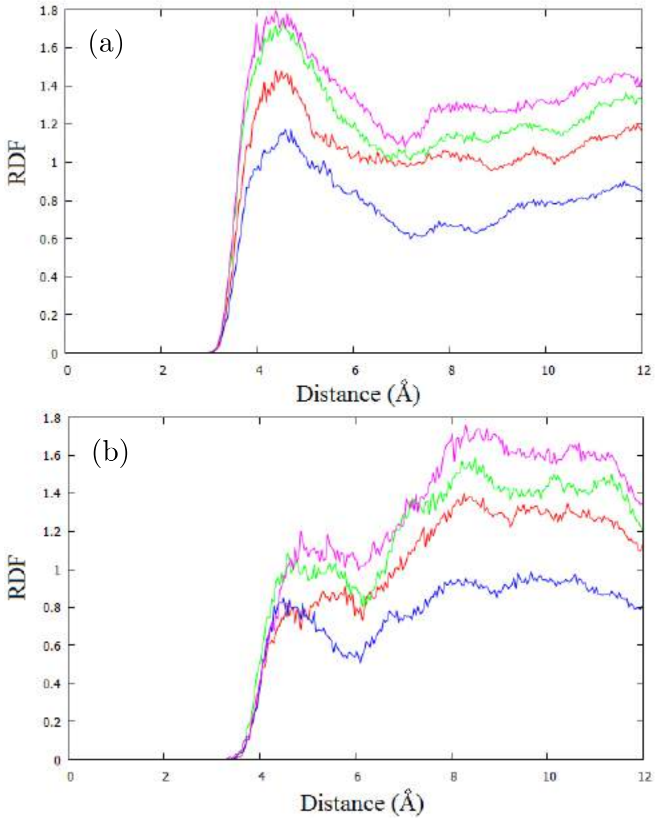

Figure A24. Computed radial distribution functions in IRMOF-1 of the CH3 group of the adsorbates referring to (a) the C3 atom of the benzene group of the linker, and (b) the Zn atom of the metallic center at 100 kPa and 448 K using a full atom model for ethylbenzene and toluene. Color lines represent the variation of the probability with the distance for each molecule: ortho- (red), meta- (green), para-xylene (blue), and ethylbenzene (pink).

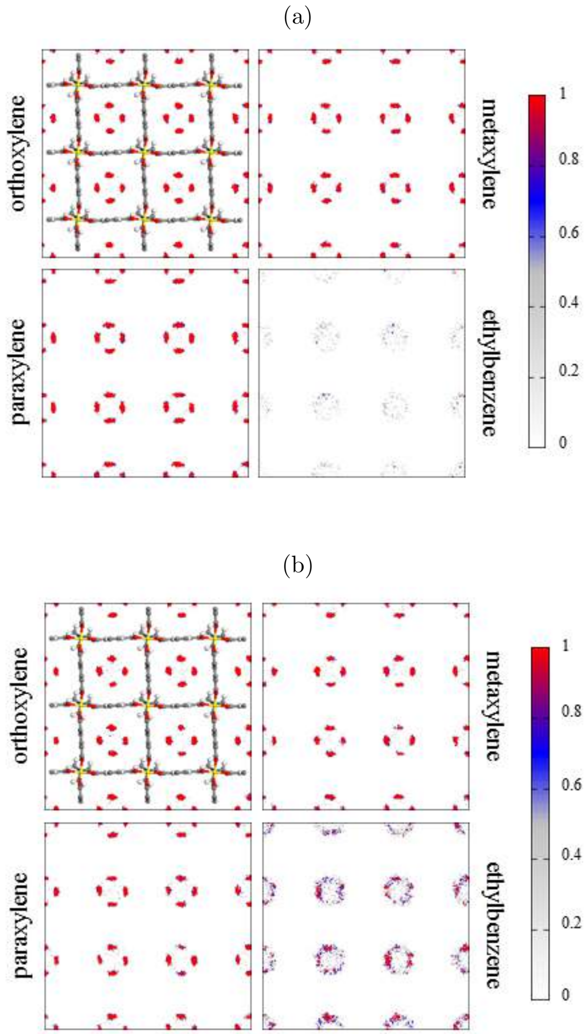

Figure A25. Average occupation profiles of ortho-, meta-, para-xylene, and ethylbenzene from the six-component mixture adsorbed in MOF-1, at 448 K and at (a) 1 kPa and (b) 100 kPa, using a full atom model for ethylbenzene and toluene. The color gradation is related to the occupation density. For an easier understanding of the location of the molecules, a representation of the structure has been added to one of the plots.

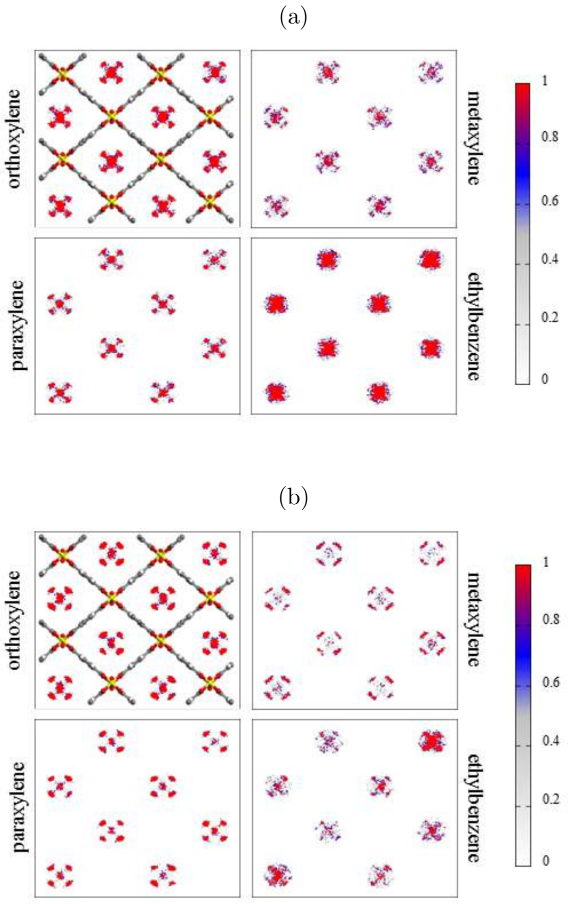

Figure A26. Average occupation profiles of ortho-, meta-, para-xylene, and ethylbenzene from the six-component mixture adsorbed in MIL-47, at 448 K and at (a) 1 kPa and (b) 100 kPa, using a full atom model for ethylbenzene and toluene. The color gradation is related to the occupation density. For an easier understanding of the location of the molecules, a representation of the structure has been added to one of the plots.

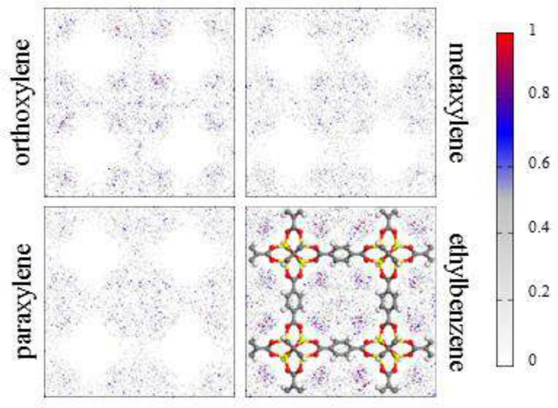

Figure A27. Average occupation profiles of ortho-, meta-, para-xylene, and ethylbenzene from the six-component mixture adsorption in IRMOF-1, at 448 K and 100 kPa, using a full atom model for ethylbenzene and toluene. The color gradation is related to the occupation density. For an easier understanding of the location of the molecules, a representation of the structure has been added to one of the plots.

Table A1. Lennard-Jones parameters and partial charges used for MOF-1, MIL-47, and IRMOF-1.

Atom	Charge (e-)	ε/ kB (K)	σ (Å)
	MOF-1		
Zn1	0.75	27.70	4.04
N1	-1.20	38.98	3.26
O2	-0.60	48.19	3.03
C1	0.47	47.86	3.47
C2	0.12	47.86	3.47
C3	0.15	47.86	3.47
C4	-0.15	47.86	3.47
H1/2	0.15	7.65	2.85
	MIL-47		
V	1.68	8.05	2.80
C1	0.56	47.86	3.47
C2	0.00	47.86	3.47
C3	-0.15	47.86	3.47
O1	-0.60	48.19	3.03
O2	-0.52	48.19	3.03
H1	0.12	7.65	2.85
	IRMOF-1		
Zn1	1.27	27.70	4.04
C1	0.47	47.86	3.47
C2	0.12	47.86	3.47
C3	-0.15	47.86	3.47
O1	-1.5	48.19	3.03
O2	-0.60	48.19	3.03
H1	0.15	7.65	2.85

Table A2. Lennard-Jones parameters and partial charges used for the adsorbates.

Atom	Charge (e-)	ε/ kB (K)	σ (Å)
Xylene isomers			
H	0.11	15.03	2.42
C	-0.11	35.24	3.55
CH3	0.11	85.51	3.80
Ethylbenzene			
H	0.11	25.45	2.36
C	-0.11	30.70	3.60
CH	-	53.0	3.74
CH2	0.11	93.0	3.68
CH3	-	108.5	3.75
Benzene			
H	0.10	30.70	3.60
C	-0.10	25.45	2.36
Toluene			
C (CH)	-0.11	30.70	3.60
C (CH3)	-0.06	30.70	3.60
H (CH)	0.11	25.45	2.36
H (CH3)	0.06	25.45	2.36
CH3	0.11	108.5	3.75

Table A3. Henry coefficients, energies, and entropies of adsorption computed for the adsorbates in MOF-1, MIL-47, and IRMOF-1. In parenthesis it is shown the error of the last digit.

Molecule	K_H (mol/kg/Pa)	|ΔS| (J/K/mol)	|ΔG| (kJ/mol)	|ΔA| (kJ/mol)	|ΔU| (kJ/mol)	|Qst| (kJ/mol)
MOF-1						
o-xylene	1.50(1) 10^{-2}	61.21(4)	44.00(9)	40.00(9)	67.43(7)	67.43(7)
m-xylene	1.04(1) 10^{-2}	62.04(9)	42.00(9)	37.00(9)	66.40(9)	66.40(9)
p-xylene	1.29(2) 10^{-2}	60.80(9)	43.00(9)	39.00(9)	66.70(5)	66.70(5)
ethylbenzene	1.20(1) 10^{-2}	57.61(3)	42.89(2)	39.17(2)	64.98(2)	64.98(2)
benzene	7.00(3) 10^{-4}	48.37(6)	32.31(9)	28.59(9)	50.26(5)	50.26(5)
toluene	3.10(5) 10^{-3}	54.70(9)	37.87(9)	34.14(9)	58.65(6)	58.63(6)
MIL-47						
o-xylene	9.36(1) 10^{-3}	38.95(1)	42.68(1)	38.96(2)	56.41(2)	61.55(2)
m-xylene	6.68 (1) 10^{-3}	40.99(1)	41.43(1)	37.70(3)	56.07(2)	56.00(1)
p-xylene	8.29 (1) 10^{-3}	39.84(1)	42.23(1)	38.51(1)	56.30(1)	56.36(7)
ethylbenzene	2.07 (1) 10^{-2}	39.53(1)	45.64(1)	41.91(2)	59.62(2)	59.62(2)
benzene	7.11 (1) 10^{-4}	28.78(8)	33.08(8)	29.36(8)	42.24(1)	42.25(1)
toluene	3.50 (1) 10^{-3}	34.32(1)	39.02(1)	35.29(2)	50.66(2)	50.66(2)
IRMOF-1						
o-xylene	1.11(1) 10^{-4}	30.50(9)	24.23 (1)	20.51 (1)	34.18(2)	34.18(2)
m-xylene	1.07 (1) 10^{-4}	30.90(9)	24.08 (1)	20.36(1)	34.22(3)	34.22(3)
p-xylene	1.08(1) 10^{-4}	30.75(6)	24.14 (1)	20.42(1)	34.19(1)	34.19(1)
ethylbenzene	1.24(1) 10^{-4}	30.41(9)	24.62 (1)	20.90 (1)	34.52(2)	34.52(2)
benzene	2.37 (1) 10^{-5}	23.90(9)	18.47 (1)	14.75(1)	25.47(1)	25.47(1)
toluene	5.00(1) 10^{-5}	27.05(9)	21.25 (1)	17.52(1)	29.64(1)	29.64(1)

(1) Barcia, P. S.; Nicolau, M. P. M.; Gallegos, J. M.; Chen, B. L.; Rodrigues, A. E.; Silva, J. A. C. *Microporous and Mesoporous Materials* **2012**, *155*, 220.

(2) Finsy, V.; Verelst, H.; Alaerts, L.; De Vos, D.; Jacobs, P. A.; Baron, G. V.; Denayer, J. F. M. *Journal of the American Chemical Society* **2008**, *130*, 7110.

Acknowledgements/Agradecimientos

Throughout this wonderful and tiresome journey that I have undertaken, I have been loyally backed and supported by many people, without whom this outcome would have never come to be. Starting with my family and co-workers, which have been by my side more than many would have, I want to thank Espe, my partner, friend, support, and everything; my sister, who I left alone to deal with my parents to go far away and has always been the best; my father and my mother, who would endure an hour and a half of English and would try to read this just to make me happy, as always; my Sevilla family, who has been the reason I have survived so long away from my other family, especially Carmen, Noelia, Pedro and Ana; my grandparents, be them here now or before, who are the best one could hope for; my uncles, aunts and cousins, especially Pablo who is the greatest and always loved meeting me every six months or so; I would like to thank Ana, because it would absolutely be impossible to be writing this without all her help, almost infinite patience and dedication; Sofía, who was always there even when I was not, and would always find a way to make our ideas into projects; Ismael, Rocío, Julio, Juanjo, Vicent, Azahara, Paula, José Little, Said, Rabdel, Patrick… those who came after, and those who left before me, thank you all for making the workplace a friendplace, you are adorable.

My friends who have always been here with me Migue and Dani, who should be up top given they are the brothers I never had; those abroad who suffered the same as me but even more, Amaranta and Bea; saving the best for last, the greatest person I have ever met, Samba, which I will always carry with me; my little boys with feathers and scales, who can always cheer me up no matter what. And also me for taking this crazy journey and you for reading at least part of it.